

Metabolic phenotyping in cells and tissues using pyruvate metabolism and nuclear magnetic resonance spectroscopy

Marius Silickas

BSc Hons.

Thesis submitted to the University of Nottingham for
the degree of Master of Research

Acknowledgements

I would like to offer my gratitude to Dr Sébastien Serres for guiding me throughout this degree and helping me develop my competence as a scientist.

Thanks to Dr Huw Williams for giving me training in NMR spectroscopy and helping me conduct my experiments.

Thanks to Dr Marie-Christine Pardon for offering constructive advice on data analysis and for providing Alzheimer's model tissue for this project

I am very thankful to Dr Laura Macri Pellizzeri and Dr Virginie Sottile for offering their invaluable help and counsel regarding mesenchymal stem cell culturing and analysis.

Finally, a huge thanks to all my friends and family, both in the UK and back home for their continuous support throughout my studies. They helped keep going, no matter the odds.

Abstract

Cellular energy metabolism is a key player in both physiological and pathological scenarios. In mouse mesenchymal stem cell populations (MSC), changes in bioenergetics are associated with differentiation into adipocyte and osteoblast lineages. As new phenotypes are adopted by differentiated cells, unique metabolic profiles are observed. On a tissue scale, metabolites associated with cellular bioenergetics (e.g. pyruvate, lactate) show potential as biomarkers for disease, such as Alzheimer's. Changes in tissue metabolic profiles are the result of the pathological mechanisms associated with disease. Additionally, metabolites are known to reflect upstream perturbations in the proteome and the genome. Thus, detection of specific metabolite signatures is a promising approach for the interpretation of physiological and pathological processes.

In this project, we explored the possible application of ^1H nuclear magnetic resonance spectroscopy to observe pyruvate metabolism in real-time in mMSCs and mouse tissues (wild-type and Alzheimer's model). Following administration of ^{13}C -labelled pyruvate, we observed a significant increase in the production of ^{13}C -labelled lactate and alanine. Comparison of newly generated metabolite ratios allowed us to determine the metabolic phenotype of cells and tissues. Following from there, we investigated changes in upstream gene and protein expression in relation to observed metabolite signatures. Our target enzymes were lactate dehydrogenase, alanine aminotransferase, and pyruvate dehydrogenase, as well as the genes associated with the expression of these enzymes.

Our results suggest that ^1H NMR spectroscopy is a viable technique for real-time metabolic studies, as we were able to discern cell and tissue phenotypes based on the observed $[1-^{13}\text{C}]\text{lactate}/[1-^{13}\text{C}]\text{alanine}$ ratios.

In Alzheimer's tissue, metabolites levels also reflected sexual dimorphism and treatment-associated effects. Indecisive results were observed when correlating metabolite signatures with changes in protein and gene expression. Lastly, using metabolomics, we identified some potential target metabolites for future investigation.

Declaration

I declare that this thesis is the product of my own work for the degree of Master of Research (MRes) at the University of Nottingham. All the data and figures presented were generated by me unless stated otherwise. Procedures not directly performed by myself are acknowledged.

It should also be noted that the work presented may lack completion due to time limitations imposed by the COVID-19 pandemic.

Marius Silickas

Student ID: 14279788

October 2021

Total word count: 31,902

Table of Contents

Chapter 1: Introduction	12
1.1 Pyruvate metabolism	12
1.1.1 Pyruvate metabolism in health.....	14
1.1.2 Pyruvate metabolism in disease	21
1.2 Key enzymes in pyruvate metabolism	25
1.3 Pyruvate metabolism in stem cells	29
1.4 Assessing pyruvate metabolism.....	32
1.5 Metabolic phenotyping using nuclear magnetic resonance (NMR) spectroscopy.....	35
1.6 Aims	42
Chapter 2: Methods	45
2.1 Cell culture	45
2.1.1 Mesenchymal stem cell differentiation	45
2.1.2 Alizarin Red staining and quantification	46
2.1.3 Oil Red O staining and quantification	46
2.1.4 Alanine aminotransferase (ALT) activity assay	47
2.1.5 Lactate dehydrogenase (LDH) activity assay.....	47
2.2 Western blotting.....	48
2.2.1 Tissue sample collection	48
2.2.2 Preparation of lysate from tissues	49
2.2.3 Protein Quantification – Bradford Assay	49
2.2.4 SDS-PAGE.....	50
2.2.5 Gel transfer	51
2.2.6 Immunoblotting.....	51
2.2.7 Processing of immunoblot data	53
2.3 Quantitative reverse transcription polymerase chain reaction (qRT-PCR).....	53
2.3.1 Sample preparation for RNA purification	53
2.3.2 Total RNA Purification.....	53
2.3.3 cDNA synthesis	54

2.3.4	Relative quantification.....	54
2.3.5	Absolute quantification	56
2.4	Nuclear magnetic resonance (NMR) spectroscopy.....	56
2.4.1	Sample preparation for NMR.....	56
2.4.2	Running the ¹ H NMR experiment	57
2.5	Statistical analysis	60
Chapter 3:	Results.....	61
3.1	Adipogenic and osteogenic differentiation of mouse mesenchymal stem cells (mMSCs) <i>in vitro</i> was successful.	61
3.2	mMSC differentiation into adipocyte and osteoblast lineages is associated with changes in LDH and ALT activities.	61
3.3	¹ H NMR observation of ¹³ C label incorporation into alanine and lactate can be used as biomarker of mMSC lineage determination during differentiation	64
3.4	Distinction of metabolic profiles in mMSC-derived populations using principal component analysis (PCA).....	66
3.5	mMSCs indicated fluctuations in gene expression during mesenchymal differentiation	67
3.6	Levels of proteins involved in pyruvate metabolism indicate minimal differentiation-associated changes.	72
3.7	¹³ C label incorporation into alanine and lactate occurs much faster in tissue samples.....	74
3.8	Wild-type tissue metabolomics display no clear grouping of tissues	78
3.9	Differences in gene expression responsible for pyruvate metabolism in mouse tissues	79
3.10	Differences in enzyme expression responsible for pyruvate metabolism in mouse tissues	81
3.11	¹ H NMR data collected from Alzheimer’s Disease mouse tissue cannot differentiate between sex or treatment	83
3.12	Metabolomics of Alzheimer’s tissues reveals differences between different sexes and treatments.	86
3.13	Gene expression of pyruvate-associated enzymes display changes based on sex and treatment.....	89
3.14	Western blot analysis reveals differences in protein levels associated with sex and inflammation	91
Chapter 4:	Discussion.....	96

4.1 mMSCs demonstrate lineage plasticity	97
4.3 Differences in enzyme activity levels reflect post-differentiation phenotypes.....	97
4.4 Real-time observation of ¹³ C-label exchange offers a promising approach to mMSC phenotyping.....	99
4.5 Creatine level fluctuations seem to be associated with mMSC differentiation.....	100
4.6 Gene and protein expression data allows insight into cell biology changes during differentiation.....	100
4.7 Kinetics data clearly separated cell and tissue sample groups	101
4.8 Although initially successful, metabolic phenotyping of tissues presents further challenges.....	102
4.9 ¹ H NMR data allows elucidation of the inflammatory mechanism in APP/PS1 mice.....	103
4.10 AD mouse livers metabolic profiles depend on sex and treatment.....	105
4.11 Amino acid metabolism seemingly plays a key role in AD cortex tissue.....	106
4.12 Real-time study is imperative when correlating metabolomics, proteomics, and genomics.....	108
4.13 Tissue complexity limits reliability of acquired data.....	108
4.14 Further development of NMR methodology is required.	109
4.15 Conclusion.....	110
5. Bibliography	112
6. Appendix.....	142

List of figures

Figure 1: Major pathways of pyruvate metabolism in health

Figure 2: The lactate dehydrogenase reaction

Figure 3: The alanine aminotransferase reaction.

Figure 4: ATP generation through cooperation between TCA cycle and OXPHOS.

Figure 5: Example of ^{13}C label incorporation in a biological system.

Figure 6: ORO and AR staining of control and differentiated mMSC populations at day 10 of differentiation *in vitro*.

Figure 7: ORO and AR staining of control and differentiated mMSC populations at day 13 of differentiation *in vitro*.

Figure 8: Changes in ALT and LDH activity associated with mMSC differentiation *in vitro*.

Figure 9: Distinction between mMSC-derived adipocytes and osteoblasts using ^1H NMR and ^{13}C -labelled pyruvate.

Figure 10: Principal component analysis of mMSC populations.

Figure 11: Gene expression heatmaps in cultured mMSCs and mMSCs-derived adipocytes and osteoblasts.

Figure 12: Western blotting results in cultured and differentiated mMSCs.

Figure 13: ^1H NMR spectroscopic measurements of ^{13}C label incorporation in tissue samples.

Figure 14: Principal component analysis of wild-type mouse tissues.

Figure 15: Absolute quantification of gene expression in wild-type mouse tissues.

Figure 16: Western blot results of wild-type mouse tissues.

Figure 17: Production of ^{13}C -labelled lactate and alanine in APP/PS1 mouse tissue.

Figure 18: Principal component analysis of APP/PS1 livers.

Figure 19: Principal component analysis of APP/PS1 cortex.

Figure 20: Relative gene expression levels of ALT, LDH, and PDH in Alzheimer's model mouse.

Figure 21: Analysis of Western blots in AD phenotype livers.

Figure 22: Analysis of Western blots in Alzheimer's phenotype cortex.

Abbreviations

- AD – Alzheimer’s disease
- ALT – alanine aminotransferase
- ATP – adenosine triphosphate
- Cr – creatine
- DMEM – Dulbecco’s Modified Eagle’s Medium
- DNP – dynamic nuclear polarization
- ETC – electron transport chain
- F LPS – female, LPS-treated tissue
- F PBS – female, PBS-treated tissue
- FAD/FADH₂ – flavin adenine dinucleotide
- GABA - γ -amino butyric acid
- GAPDH – glyceraldehyde 3-phosphate dehydrogenase
- LDH – lactate dehydrogenase
- LPS - lipopolysaccharide
- M LPS – male, LPS-treated tissue
- M PBS – male, PBS-treated tissue
- mMSC – mouse mesenchymal stem cells
- MPC – mitochondrial pyruvate carrier
- NAD⁺/NADH – nicotinamide adenine dinucleotide
- NMR – nuclear magnetic resonance
- OXPHOS – oxidative phosphorylation
- PBS – phosphate buffered saline
- PC – pyruvate carboxylase
- pCr – phosphocreatine
- PDH – pyruvate dehydrogenase
- PDK – pyruvate dehydrogenase kinase
- PDP – pyruvate dehydrogenase phosphatase

- PECK - phosphoenolpyruvate carboxykinase
- PK – pyruvate kinase
- pPDH – phosphorylated pyruvate dehydrogenase
- qPCR – quantitative real-time polymerase chain reaction
- TCA – tricarboxylic acid cycle

Chapter 1: Introduction

1.1 Pyruvate metabolism

Pyruvate is a major intermediate metabolite in the bioenergetic network of eukaryotic and mammalian cells. Primarily generated during the breakdown of glucose in the cytosol, pyruvate is the end product of glycolysis and closely associated with the energetic state of the cell. Although the standard fate of pyruvate is to support adenosine triphosphate (ATP) synthesis in the mitochondria by providing carbon source to the tricarboxylic acid cycle (TCA), alternative pathways (e.g. lactate and/or alanine biosynthesis, gluconeogenesis) grant metabolic flexibility to this metabolite. The reversibility of the cytosolic pyruvate conversions further allows for rapid pyruvate allocation and regeneration to fulfil the energetic and biosynthetic demands of cells (Gray, Tompkins and Taylor, 2014). This is well-documented in the context of stem cell differentiation, with the inherent metabolic plasticity termed “metabolic reprogramming” (Shyh-Chang, Daley and Cantley, 2013; Loeffler *et al.*, 2018). The control of pyruvate metabolism confers an additional mechanism that influences lineage commitment, specification, and self-renewal (Ito and Suda, 2014; Song *et al.*, 2019). As such, metabolic reprogramming through pyruvate-associated pathways allows for metabolic adjustments that determine cell identity. For instance, there is a shift from glycolysis towards mitochondrial oxidative phosphorylation and oxidative stress during the maturation of stem cells into differentiated cells (Rafalski, Mancini and Brunet, 2012). In addition to influencing tissue differentiation, the pivotal role of pyruvate in the generation of mitochondrial ATP and driving key biosynthetic pathways makes it a vulnerable target for disruption in disease. Aberrant energy metabolism is a hallmark trait of certain pathologies, such as cancer or

neurodegenerative disease (e.g. Alzheimer's disease) (Michelson *et al.*, 2001; DeBerardinis *et al.*, 2008). Understanding the differences between pyruvate metabolism in both health and disease states is key to developing novel methods of detection and intervention.

1.1.1 Pyruvate metabolism in health

Pyruvate metabolism in eukaryotic and human cells can be classified into two distinct groups based on cellular compartments in which the pyruvate is present: the cytosol and the mitochondria. Cytosolic pyruvate is primarily generated by the dephosphorylation of phosphoenolpyruvate through the activity of enzyme pyruvate kinase (PK; EC 2.7.1.40) during the last step of glycolysis (Gupta and Bamezai, 2010). Complete breakdown of a single glucose molecule via the glycolytic pathway reactions yields two molecules of pyruvate along with two net molecules of ATP. The generated pyruvate then undergoes one of three fates: 1) conversion to lactate by the enzyme lactate dehydrogenase (LDH; EC 1.1.1.27); 2) transamination into alanine by the enzyme alanine aminotransferase (ALT; EC 2.6.1.2); 3) transportation into the mitochondria mediated by the mitochondrial pyruvate carrier (MPC), ultimately linking pyruvate to the TCA carbon flux. While the latter is the most predominant fate of pyruvate in high energy demand tissues, the alternative cytosolic conversions of pyruvate fulfil situational metabolic demands (Brosnan, 2000; Hui *et al.*, 2017) (Figure 1)

Reduction of pyruvate to lactate is a reversible reaction catalyzed by LDH and is coupled with the regeneration of NAD^+ from NADH (Figure 2). This reaction is crucial in managing excessive glycolytic flux associated with spontaneous increase in tissue energy demand (Greenhaff *et al.*, 2004). The most prominent example of such stressful metabolic conditions is during periods of intense physical exercise in humans (Stallknecht, Vissing and Galbo, 1998). Under immense strain, the energy demands for maintaining skeletal muscle contractions far exceeds the

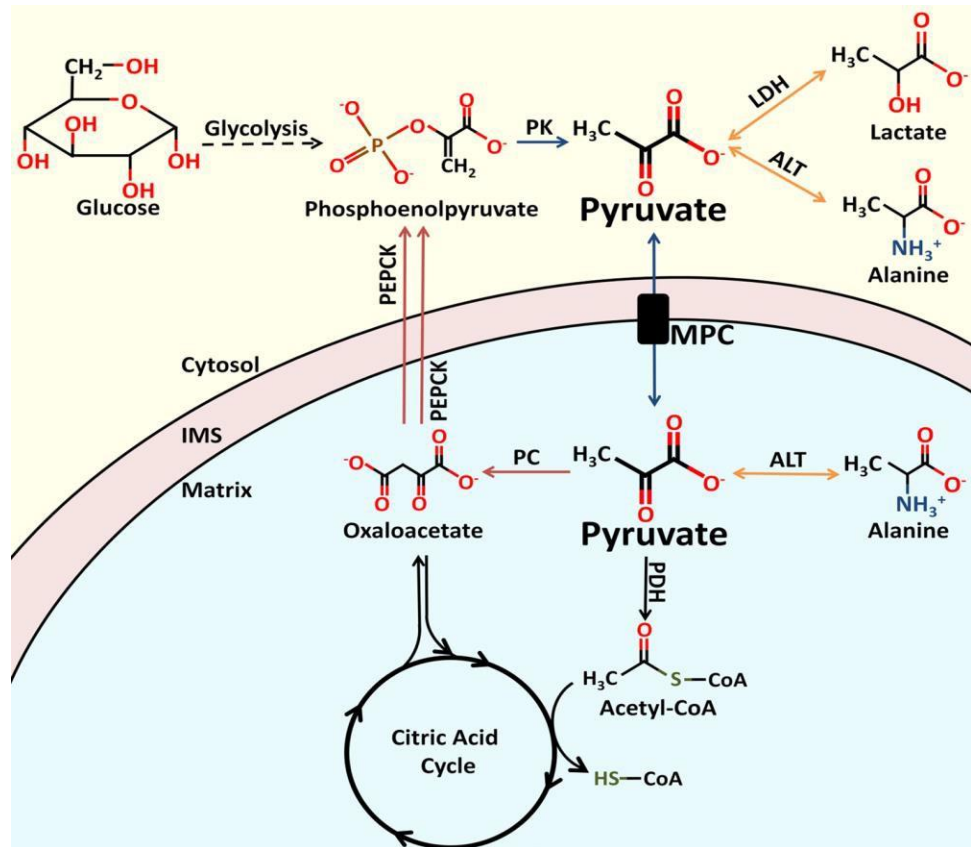


Figure 1: Major pathways of pyruvate metabolism in health. Pyruvate occupies a crucial position in the central carbon metabolism. Various biochemical reactions are linked to the generation of pyruvate, including glycolysis, lactate oxidation, and alanine transamination. Pyruvate entry into the mitochondrial matrix is regulated by the MPC. Similar as in the cytosol, pyruvate has multiple fates inside the mitochondrial matrix. In the form of Acetyl-CoA, pyruvate enters the citric acid cycle and facilitates ATP synthesis. Pyruvate conversion to oxaloacetate serves as an anaplerotic pathway to replenish the citric acid cycle intermediates. Alternatively, oxaloacetate can be metabolized to phosphoenolpyruvate, thus facilitating gluconeogenesis. Molecular structures of all the core compounds, as well as the enzymes involved in reaction catalysis, are shown. PK, pyruvate kinase; LDH, lactate dehydrogenase; ALT, alanine aminotransferase; MPC, mitochondrial pyruvate carrier; PDH, pyruvate dehydrogenase; PC, pyruvate carboxylase; PEPCK, phosphoenolpyruvate carboxykinase; IMS, intermembrane space. Taken from (Gray, Tompkins and Taylor, 2014)

rate of mitochondrial ATP production (Mookerjee *et al.*, 2017). Simultaneously, the resulting accumulation of NADH inhibits glycolysis, as glycolysis required NAD⁺ as a cofactor. LDH promotes glycolytic ATP generation by recycling NADH into NAD⁺ for glycolysis, concomitantly producing lactate (Figure 2). As a result of the LDH reaction, glycolysis is switched to an anaerobic mode of function, producing ATP to support work rates unsustainable by oxidative phosphorylation alone. Given renewed oxygen supply, this process is reversed via the Cori cycle, where the lactate produced in the muscle is delivered to the liver via the bloodstream and converted back to pyruvate by an isoform of LDH (Markert, Shaklee and Whitt, 1975). The free interconvertibility between pyruvate and lactate allows utilization of lactate as a gluconeogenic precursors during periods of fasting. Although seemingly a situational metabolite in healthy tissues, lactate maintains importance in certain tissues even under conditions of normoxia and abundant energy supply. Lactate synthesis has been found to be prioritized by cultured and primary mammalian adipocytes even in times of glucose deprivation, indicating adipose tissue contribution to whole-body lactate turnover (Krycer *et al.*, 2020). Furthermore, neurons have been found to preferentially take up lactate released by astrocytes to fuel oxidative phosphorylation (Bouzier-Sore *et al.*, 2006). However, elevated lactate synthesis is closely associated with some disease states, as discussed later.

Cytosolic mammalian pyruvate metabolism is closely associated with the catabolism of amino acids such as alanine, serine, and threonine. The former is noteworthy as it is a major protein-derived gluconeogenic precursor. *In vitro* and *in vivo* studies have shown that glucose biosynthesis from alanine heavily outclasses all other amino acids in terms of synthesis rate and reaction saturation (Felig, 1975). At the core of this alanine utility is the enzyme ALT, also often referred to as glutamic-pyruvic transaminase

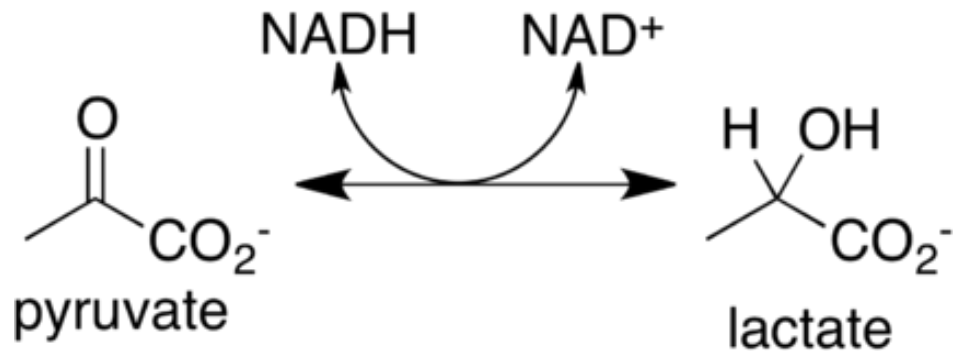


Figure 2: The lactate dehydrogenase reaction. The reaction catalyzed by LDH links the production of lactate from pyruvate to the regeneration of NAD^+ from NADH . Reversible interconversion of these metabolites allows for metabolic flexibility.

(GPT). ALT mediates the reversible conversion of alanine and α -ketoglutarate to pyruvate and glutamate, effectively bridging energy metabolism with amino acid biosynthesis pathways (Figure 3). Further investigations of this link have revealed a direct linear relationship between pyruvate and alanine levels in the blood plasma. With increased glucose utilization by the skeletal muscle during periods of exercise, simultaneous increases in the levels of circulatory alanine have been observed (Felig, 1973). Termed the alanine cycle, this interplay between pyruvate and alanine closely resembles the Cori cycle in that, during increased energy consumption, excess circulatory alanine is scavenged up by the liver and is recycled back to pyruvate for utilization in gluconeogenesis. However, the alanine cycle suffers from inefficiency due to necessitated detoxification of ammonia, a by-product of glutamate deamination. It is estimated that the alanine cycle, with respect to its contribution to hepatic glucose synthesis and role as peripheral tissue by-product endpoint, occurs at a rate of approximately 50% of that observed for the Cori cycle. Alanine cycling is also a crucial mechanism in brain tissue, where, despite not contributing to energy or neurotransmitter metabolism directly, alanine

plays a role in carbon skeleton recycling in both rodents and humans (Evans *et al.*, 2004; Bröer *et al.*, 2007).

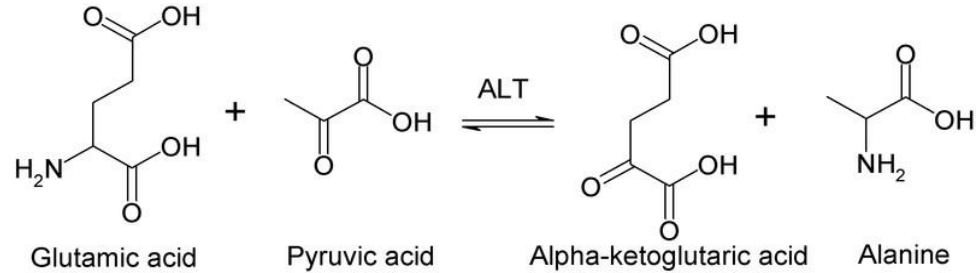


Figure 3: The alanine aminotransferase reaction. This pathway links pyruvate to amino acid metabolism. Pyruvate can be thus utilized for biosynthetic purposes, while the reverse reaction allows for amino acid utilization for energy generation in the absence of other substrates.

In most mammalian tissues, the pyruvate produced in the cytosol is predominantly imported into the mitochondrial matrix where it drives the TCA cycle flux, thereby facilitating ATP production by oxidative phosphorylation (OXPHOS) and numerous biosynthetic pathways (Figure 4). Linkage between cytosolic and mitochondrial pyruvate is mediated by the mitochondrial pyruvate carrier (MPC), a carrier protein located on the inner mitochondrial membrane (Bricker *et al.*, 2012). Once inside the mitochondria, pyruvate has several potential fates. Nevertheless, the majority is oxidized to carbon dioxide in the TCA cycle to support ATP production. In this pathway, pyruvate dehydrogenase (PDH) complex catalyzes the irreversible set of reactions that ultimately converts pyruvate and NAD^+ into acetyl-CoA, NADH, and carbon dioxide. Acetyl-CoA then enters the TCA cycle, where the remainder of the pyruvate carbon skeleton is metabolized. Alongside energy metabolism, acetyl-CoA can contribute anabolic pathways, including lipogenesis, cholesterol synthesis, and the production of acetylcholine (Pietrocola *et al.*, 2015). The oxidation of

pyruvate in the TCA cycle results in the reduction of NAD^+ and FAD to NADH and FADH_2 , respectively. These electron carriers are utilized by the electron transport chain (ETC) machinery to generate a proton gradient in the intermembrane space of the mitochondria necessary for OXPHOS. The final electron acceptor in this chain is oxygen, the absence of which deems mitochondrial energy production futile and upregulates anaerobic glycolysis. Overall, the full oxidation of a single glucose molecule leads to the generation of approximately 30 molecules of ATP, demonstrating the efficiency of OXPHOS and the difference between cytosolic and mitochondrial energy metabolism (Nath, 2016).

An alternative fate to decarboxylation by PDH to acetyl-CoA is the irreversible, ATP-dependent carboxylation of pyruvate to oxaloacetate, catalysed by the enzyme pyruvate carboxylase (PC; EC 6.4.1.1) (Utter and Keerch, 1960). The utility of mitochondrial pyruvate is therefore not limited to ATP production, but also includes carbon flux provision for biosynthetic pathways intersecting the TCA cycle through several intermediate metabolites. Oxaloacetate is one such intermediate that is used for aspartate and asparagine biogenesis (Curthoys, 1995; Wu and Morris, 1998). Furthermore, oxaloacetate, along with citrate, are key players in gluconeogenesis and lipogenesis, respectively (Owen, Kalhan and Hanson, 2002). Other examples of biosynthetic precursors associated with the TCA cycle include α -ketoglutarate (used in glutamine, glutamate, arginine and proline biosynthesis) and succinyl-CoA (heme production) (Curthoys, 1995; Wu and Morris, 1998; Orkin and Zon, 2008). The multitude of pathways associated with the TCA cycle place a significant strain on the carbon pool available in the mitochondria. Any intermediates consumed for biosynthetic purposes must be replenished to maintain the TCA cycle carbon flux. Anaplerotic reactions, such as the one catalysed by PC, fulfil a vital role by replenishing the diminished carbon pool in the form

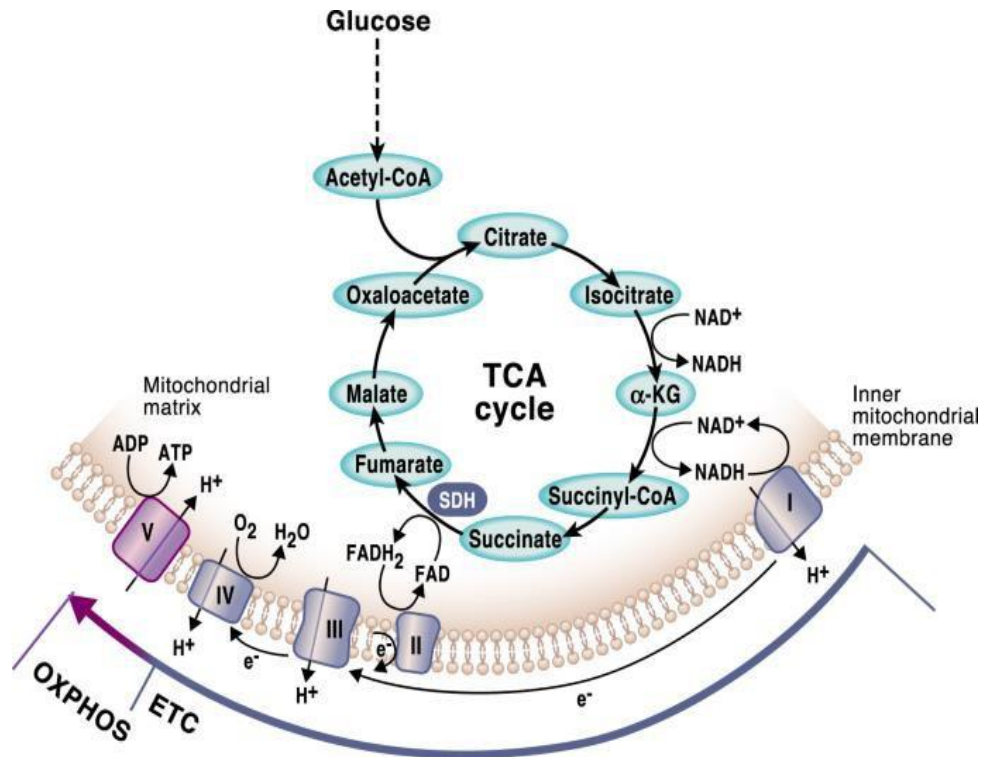


Figure 4: ATP generation through cooperation between TCA cycle and OXPHOS. Every complete TCA cycle rotation generates reduced counterparts of NAD^+ and FAD , termed NADH and FADH_2 , respectively. The electrons (e^-) on NADH and FADH_2 proceed to be transported to the enzymatic complexes (marked in Roman numerals) of the electron transport chain (ETC), located on the inner mitochondrial membrane (IMM). Passage of electrons through the ETC complexes and the IMM promotes export of protons (H^+) into the intermembrane space of the mitochondria, thus generating a proton gradient. This gradient is utilized to drive ATP synthesis by complex V. Intermediates of the TCA cycle, such as $\alpha\text{-KG}$ or oxaloacetate, also participate in biosynthetic reactions (not shown). $\alpha\text{-KG}$, α -ketoglutarate; SDH, succinate dehydrogenase; NAD^+/NADH , nicotinamide adenine dinucleotide; FAD/FADH_2 , flavin adenine dinucleotide. Taken from (Martínez-Reyes and Chandel, 2020)

of cycle intermediates (Owen, Kalhan and Hanson, 2002). The anaplerotic role of oxaloacetate generated by PC is to serve as an acceptor for the acetyl-CoA produced by PDH. Brain cells are especially reliant on anaplerosis, as they suffer heavy TCA cycle intermediate losses during neurotransmission events involving glutamate and γ -aminobutyric acid (GABA) (Hassel, 2000). Another crucial anaplerotic reaction is the breakdown of glutamine and glutamate to α -ketoglutarate, which is often observed to be vital for some the proliferation of many cancer cells (Brosnan, 2000).

1.1.2 Pyruvate metabolism in disease

The disruption of energy metabolism in mammalian cells has been implicated in the onset and progression of disease (Raichur *et al.*, 2014; Tchetina, 2018). The severity of a specific disease is closely associated with the localization of the disruption (often a mutation) within the organism. Tissues with a high consumption rate of ATP, such as the nervous system, are at the highest risk due to their prioritization of ATP production through carbohydrate metabolism. Most aberrations in pyruvate metabolism originate from mutations in any of the numerous genes encoding regulatory enzymes. A plethora of diseases are linked to pyruvate dysmetabolism, with the most prominent ones being cancer, neurodegeneration and heart failure.

Aberrant cell bioenergetics have been widely observed across numerous types of neoplasia (Sellers *et al.*, 2015; Diers *et al.*, 2016; Bensard *et al.*, 2020). One recurring theme among the variety of tumours is the cellular dependence on the Warburg effect – a phenomenon described by a markedly increased uptake of glucose and conversion of pyruvate to lactate preferentially to OXPHOS in the presence of sufficient oxygen supply. This effect, also termed aerobic glycolysis, was first observed by Otto Warburg almost a century ago and was originally believed to be the

result of impaired mitochondrial metabolism (Warburg, 1931, 1956). However, the discovery of Warburg effect-driven bioenergetics in highly proliferative cell types, including human and mouse lymphocytes, has shed some light on the functional advantages of glycolytic metabolic modes. Despite the inherent energetic inefficiency of glycolysis in comparison to OXPHOS, a major advantage of aerobic glycolysis over OXPHOS is the rate of the ATP production. If the glycolytic flux is sufficiently high, the ATP production can easily outpace the ATP yield from OXPHOS. Therefore, when glucose supply is abundant, the inefficiency to glycolysis is compensated for by the faster breakdown of glucose to meet the high demands of growing and dividing cells (Lunt and Vander Heiden, 2011). A direct consequence of the upregulation of the glycolytic carbon flux is the elevated biosynthesis of lactate. This metabolic mode makes glycolysis self-sufficient, as it regenerates NAD^+ necessary to keep the glycolysis running.

In addition to sustaining aerobic glycolysis, other explanations for elevated lactate production could be observed through closer inspection of anaerobic glycolysis machinery. Although glycolysis uncoupling from OXPHOS is predictable under hypoxic conditions, molecular mechanisms that prevent oxidative breakdown of pyruvate are known. This switch is necessary to prevent mitochondrial oxidative stress by reducing electron flux through oxidative phosphorylation in the absence of sufficient oxygen. Expression levels of both pyruvate dehydrogenase kinase (PDK) and lactate dehydrogenase A (LDHA) are induced in response to hypoxia (Shim *et al.*, 1997; Kim *et al.*, 2006). Through phosphorylation of PDH, PDK prevents the import of pyruvate into the mitochondrial matrix, while LDH-A converts the cytosolic pyruvate to lactate. As PDH has a low V_{max} , this consumption of pyruvate is critical to avoid potentially harmful accumulation of pyruvate in addition to NAD^+ regeneration (Fantin, St-Pierre and Leder,

2006). Meanwhile, the TCA cycle ensures the flux of biosynthetic intermediates for lipid and amino acid synthesis. For example, the export and cleavage of citrate in the cytosol produces acetyl-CoA and oxaloacetate, which are utilised in lipogenesis and non-essential amino acid synthesis, respectively. The lactate is utilised by cancer cells to facilitate their proliferation through several mechanisms: (i) the inhibition of the immune system by tumour microenvironment acidification, (ii) regulation of extracellular matrix metalloproteinase activity, and (iii) maintenance of superficial tumour cell bioenergetics through conversion to pyruvate (Pavlova and Thompson, 2016). The flexibility of energetic, and thus, pyruvate metabolism is key mechanism in cancer pathology that has recently emerged as a novel hallmark in the benign-malignant transition of tumours (Hanahan and Weinberg, 2011).

In addition to cancer, neurodegenerative disease pathology is also closely associated with perturbations in energy metabolism. Defects in various enzyme activities, including PDH, MPC, and PC, have been associated with neurological disorders (Sorbi, Bird and Blass, 1983; Patel and Tiwari, 2014; Rossi *et al.*, 2020). The human brain relies heavily on glucose and pyruvate for ATP production, accounting for almost a quarter of daily whole-body glucose consumption (Mink, Blumenshine and Adams, 1981). Research has determined that neurons are highly reliant on oxidative metabolism and may actively import lactate to support pyruvate flux into the mitochondria (Attwell and Laughlin, 2001). Simultaneously, glucose is redirection to the pentose phosphate pathway to generate NADPH for glutathione regeneration (Dienel, 2019). Such metabolism in neurons is supported by astrocytes, a highly glycolytic population of cells in the brain (Pellerin *et al.*, 1994, 2007). Lactate produced by astrocytic glycolysis is released into the extracellular space and is subsequently taken up by neurons as a carbon source for the TCA cycle. This coupling mechanism is

referred to as the astrocyte-neuron lactate shuttle (ANLS) (Pellerin and Magistretti, 1994; Bélanger, Allaman and Magistretti, 2011). Recent research indicates that the metabolic coupling of neurons and astrocytes is crucial in maintaining neuronal energy supply, as well as fulfilling homeostatic and cytoprotective roles (Stuart *et al.*, 2011; Magistretti and Allaman, 2018; Ioannou *et al.*, 2019). Inability to satisfy neuronal energetic demand leads to loss of proper neuronal function, which is absolutely central for the pathogenesis of Alzheimer's disease (AD) (Acosta, Anderson and Anderson, 2017).

Several factors are associated with the abnormal pyruvate metabolism observed in AD, including the generation of reactive oxygen species (ROS), decreased glucose uptake, and neuronal hyper-excitability (Uemura and Greenlee, 2001; Valko *et al.*, 2007; Horan, Pichaud and Ballard, 2012; Šišková *et al.*, 2014). ROS production, in particular, is noted as a hallmark of AD pathogenesis. Major sources of endogenous ROS include the mitochondria and NADPH oxidase. ROS radicals indirectly stimulate the cleavage of amyloid precursor protein (APP) into amyloid beta (A β) oligomers, the peptide widely recognized as the main pathogen in AD. Through the activation of NADPH oxidase, A β upregulates the production of more ROS, creating a feedforward cycle leading to increased neurotoxicity. Eventually, the ROS-upregulated hypoxia inducible factor-1 α (HIF-1 α) signaling reduces PDH activity (Casley *et al.*, 2002). Alternatively, PDH can be inhibited by acrolein, a product of lipid peroxidation in the presence of high oxidative stress (Pocernicha and Butterfield, 2003). Inactivated PDH severely impacts the ATP generation capacity of the neurons, leading to cellular dysfunction, and, ultimately, neuronal death. As a result, pyruvate concentrations in the cerebrospinal fluid directly correlate with severity of dementia (Parnetti *et al.*, 1995). Conversely, recent research has discovered that systematic pyruvate

administration alleviated the neurodegenerative burden in both rat and mouse models of AD (Isopi *et al.*, 2015; Wang *et al.*, 2015). All these findings solidify the pivotal role of neuron bioenergetics in AD progression. Looking at the precursor of pyruvate, glucose, a more complex picture of metabolic dysfunction in AD can be drawn. Hyperglycemia, alongside impaired glycemic regulation, has been shown to be closely linked to cognitive decline (Cukierman-Yaffe *et al.*, 2009). Ageing-associated factors, including reduced insulin signaling and PI3K/Akt pathway dysregulation are implicated in the impairment of glucose uptake across the blood-brain barrier (Barone *et al.*, 2016). Consequently, capacity for glucose utilization is notably impaired in AD. In turn, both glycolysis and OXPHOS enter altered states of function in AD patients. Altered glycolysis in neuronal cells can lead to mitochondrial leakage-facilitated cell death, while altered OXPHOS leads to neuronal cell death via ROS generation (Petit-Taboué *et al.*, 1998; Lemeshko, 2018). Due to reduced insulin signaling, AD patients seem to be at increased risk for type 2 diabetes (Janson *et al.*, 2004). Summing up, AD metabolic dysfunction is heavily implicated in the causality and progression of AD. Metabolic pathways, therefore, present a potential target for both early diagnosis, as well as therapy.

Certain physiological conditions have the potential to exacerbate AD pathogenesis. Namely, inflammation has emerged as a driving force behind AD progression (Wyss-Coray and Rogers, 2012; Kinney *et al.*, 2018). Genetic factors associated with an increased inflammatory state presence have been linked to AD susceptibility in subjects. Additionally, elevated levels of pro-inflammatory biomarkers can be observed in circulation in subjects at risk for developing late-onset AD, as well as those in the preclinical stage of AD, termed mild cognitive impairment (Koyama *et al.*, 2013). These findings suggest that inflammation is a key catalyst

mechanism that can potentially exacerbate cognitive decline and A β plaque accumulation in patients. This picture is further complicated by the presence of a sexual dimorphism – in comparison to men, women experience more rapid AD-associated neurodegeneration, as well as a more prominent inflammatory response (Klein and Flanagan, 2016; Andrew and Tierney, 2018). Consequently, observations of inflammation-induced AD phenotypes yield some distinctions between the sexes. On a metabolic level, this interaction between inflammation and AD progression has not been extensively studied.

1.2 Key enzymes in pyruvate metabolism

Three key enzymes associated with pyruvate fate allocation are LDH, ALT and PDH. These enzymes convert pyruvate to lactate, alanine, and acetyl-CoA, respectively. LDH and ALT are cytosolic enzymes, while PDH is located in the mitochondria. Each of these three enzymes has unique structural properties and regulatory mechanisms, which contribute to the fate of pyruvate in mammalian cells. It is therefore imperative to understand the specifics of each enzyme in context of studying pyruvate metabolism in eukaryotes.

LDH is tetrameric oxidoreductase that is almost ubiquitously expressed across all mammalian tissues. Five isoforms of the LDH enzyme exist, each a unique combination of subunits (Drent *et al.*, 1996). The two most prevalent subunits in a mammalian system are LDHA and LDHB. These subunits are often defined by the tissue they are predominantly expressed in - LDHA is commonly termed as the M subunit (for muscle), while LDHB is referred to as the H subunit (for heart). The five isoforms of LDH (LDH1-5) are therefore various combinations of M and H subunits: H₄, H₃M₁, H₂M₂, H₁M₃, and M₄. While enzymatically similar, these isozymes differ in tissue distribution (Laughton *et al.*, 2000). For example, H₄ is found in the heart, while H₂M₂ is the primary isozyme of the lungs. This tissue-specific

isozyme distribution is based on a clear functional and regulatory distinction between the M and H isoforms (Świderek and Paneth, 2011). The M form promotes the biosynthesis of lactate, whereas H favours the opposite direction of the same reaction, producing pyruvate. Furthermore, the H isoform seems to be allosterically inhibited by pyruvate that otherwise has no effect on the M isoform. These seemingly minor differences in LDH isozyme functionality are linked to the distribution pattern of tetramers, although studies have suggested that LDH isozyme patterns play no physiological role (Quistorff and Grunnet, 2011). On a genetic level, LDH is encoded by multiple genes in mice, each encoding a specific subunit. H and M subunits are encoded by *Ldha* and *Ldhb* genes, respectively. In mammalian systems, other subunits, such as LDHC and LDHBx can also be included in the final tetramer, although in very specific environments (Goldberg *et al.*, 2010; Schueren *et al.*, 2014).

LDH is subject to three levels of regulation: allosteric effects, substrate-level regulation, and transcriptional control (Valvona *et al.*, 2016). Substrate availability and their concentration greatly impact the activity of LDH. Generally, allosteric activation of LDH occurs in the presence to fructose-1,6-biphosphate (FBP) (Feldman-Salit *et al.*, 2013). As FBP interacts with LDH, it increases LDH affinity for its substrates. The availability of substrates, as well as their concentration, is perhaps the most crucial regulator of LDH activity. For example, during strenuous muscle activity, OXPHOS machinery cannot keep up with the ATP demand. Therefore, pyruvate accumulates.

Additionally, due to limited oxygen supply, NAD⁺ cannot be regenerated. The excessive levels of pyruvate and NADH are therefore channelled through LDH. On a transcriptional level, genes encoding LDH proteins contain regulatory sequences that can bind major transcription factors, such as HIF-1 α and c-Myc (Firth, Ebert and Ratcliffe, 1995; Lewis *et al.*,

1997). As HIF-1 α is only stabilised under hypoxic conditions, LDHA gene expression becomes upregulated in response. C-Myc regulation of LDHA is rather complex, with some research suggesting a negative feedback loop. LDHA gene expression is often upregulated in cancers (Feng *et al.*, 2018).

Similar to LDH, ALT exists in several isoforms – ALT1 and ALT2, expressed by *Gpt1* and *Gpt2* genes in mice, respectfully (Rafter *et al.*, 2012). The major differences between these two variants lie in the localization on a cellular and tissue level. ALT1 predominates in the cytosol and is highly expressed in adipose, intestinal, and hepatic tissues. Conversely, ALT2 is compartmentalized entirely within the mitochondria of muscle and brain cells. An additional layer of complexity is added by the varying expression profiles across different species. In rats and mice, for example, both ALT isoforms are abundant in liver tissue. In contrast, human tissues display a clear dominance of ALT1, with ALT2 showing little to no presence in the liver (Glinghammar *et al.*, 2009). One common pattern is the predominance of ALT in liver tissue. Compared to the serum, the activity of ALT is roughly 3000 times higher in hepatocytes. Therefore, individuals suffering from acute or chronic hepatocellular injury present with increased ALT activity in the serum. Assays specific to ALT isoforms have been developed to allow separation of ALT1 and ALT2 levels in the blood (Liu *et al.*, 2008). No metabolic diseases are associated with deleterious ALT mutations. However, the absence of ALT may predispose the body to other disorders. In terms of enzyme regulation, ALT has not been extensively studied. However, research suggest that androgens, aminothiols, and vitamin B6 derivatives are all implicated in the control of ALT activity (Coss *et al.*, 2012; Mechie *et al.*, 2015). Additionally, transcription of *Alt1* and *Alt2* are upregulated during periods of fasting (Zhang *et al.*, 2011).

Unlike LDH and ALT, PDH is localised within the mitochondria, where it

directs pyruvate flux through OXPHOS. PDH is often referred to as the E1 component of the pyruvate dehydrogenase complex (PDC), a massive ~10MDa protein. The role of the PDC is to catalyse a sequence of enzymatic reactions, the summary of which is the generation of acetyl-CoA, NADH, and CO₂ from pyruvate and NAD⁺. PDH itself is a heterotetramer, composed of two α (α1 and α2) and two β subunits (Ciszak *et al.*, 2003). In mice, these subunits are encoded by *Pdha1*, *Pdha2*, and *Pdhb* genes. Mutations in the *Pdha1* are a well-established cause for pyruvate dehydrogenase deficiency (Patel *et al.*, 2012a). In terms of enzymatic regulation, phosphorylation-driven inhibition is a critical mechanism in PDH activity control. In response to elevated ATP, NADH, and acetyl-CoA, PDK enzymes phosphorylate PDH at specific serine residues (such as Ser-264 or Ser-293), thus inactivating PDH (Morales-Alamo *et al.*, 2018). Following phosphorylation, these residues lose their binding affinity for lipoyl domains, which are crucial for reaction catalysis. Pyruvate dehydrogenase phosphatases (PDP) act in opposition to PDKs, removing phosphate groups from inhibited PDH. PDP activity is upregulated in the presence of insulin, phosphoenolpyruvate, and AMP (Holness and Sugden, 2003). Expression patterns of PDKs and PDPs vary depending on tissue (Huang *et al.*, 1998; Klyuyeva *et al.*, 2019). Overall, given the importance of pyruvate in tissue differentiation and metabolic disorders, accessible and reliable markers that could measure pyruvate metabolism, including LDH, ALT, and PDH, are therefore needed as they would have the potential to monitor tissue differentiation, diagnose and treat diseases.

1.3 Pyruvate metabolism in stem cells

Although conventionally viewed as a by-product of cell lineage commitment and specialization, stem cell metabolism has recently received appreciation as a regulatory mechanism influencing the stem cell epigenome (Ryall *et al.*, 2015). This concept of “metabolic reprogramming”

describes the plasticity of stem cell bioenergetics in response to signals instructing quiescence, self-renewal, and differentiation. The turnover rate of tissue-specific stem cells varies dramatically, with some populations undergoing constant proliferation while others exist in quiescence. Bioenergetic flexibility ensures the provision of sufficient metabolic fuel to sustain specific cell states and the generation of substrates and cofactors involved in epigenetic regulation (Folmes, 2017). The balance between glycolytic and oxidative metabolic modes is thus indicative of stem cell fate status. Similar to cancer cells, proliferating stem cell populations avidly uptake and metabolize glucose, but limit the mitochondrial oxidation of the generated pyruvate (Simsek *et al.*, 2010; Ito and Suda, 2014). This glycolytic program is usually followed up by a transition to OXPHOS during cell differentiation (Rodríguez-Colman *et al.*, 2017). The initial step in the transition from glycolytic to oxidative metabolic mode is the increased utilisation of pyruvate and its derivative carbon sources. Therefore, pyruvate metabolism has a key role in stem cell fate dynamics.

The positioning of pyruvate at the intersection of numerous crucial metabolic pathways is exploitable in the context of tissue engineering and, more precisely, regenerative medicine. These fields investigate the potential of regenerative therapies that could heal or replace tissues and organs affected by age, disease, or physical trauma (Berthiaume, Maguire and Yarmush, 2011). In recent years, regenerative medicine has seen a drastic rise in interest in the UK, leading to nation-scale initiatives being undertaken to realise the full potential of this research area (McCall, 2012; O'Dowd, 2013). Much emphasis is placed on stem cell-based therapies, the development of which has resulted in clinically important treatments (Mao and Mooney, 2015). However, while stem cell transplantation is a very well-established and clinically validated intervention for some diseases, in others the outcomes have remained poor (Coppell *et al.*, 2010; Moya *et al.*, 2018). Ceaseless investigations into improving stem cell therapies, such

as better safety and effective differentiation ability, have been a priority in the field.

Nowadays, multiple types of stem cells are available to researchers, each with differing potencies: pluripotent (tri-lineage - ESCs, iPSCs), unipotent (single lineage – hematopoietic tissue progenitor cells, such as myeloids), and multipotent (more than one lineage – adult and tissue-specific MSCs) (Levenberg *et al.*, 2002; Tabar and Studer, 2014; Liu, Xia and Li, 2015). Choosing the right type of stem cell is crucial for obtaining favourable results in regenerative therapy development. Mesenchymal stem cells isolated from bone marrow, adipose tissue, and umbilical cord have shown considerable potential in combating certain pathologies, such as musculoskeletal disorders (Richardson *et al.*, 2016). Coincidentally, MSCs have also demonstrated promise in the treatment of neurological disorders, such as AD (Liu, Yang and Zhao, 2020). Treatments using MSCs derived from the bone marrow and the human umbilical cord have been demonstrated to reduce astrocytic inflammation and A β plaque burden in AD model mice, respectively (Lee *et al.*, 2012; Nakano *et al.*, 2020). Furthermore, MSCs demonstrate capacity for neuronal differentiation, suggesting potential clinical roles in restoration of neuronal connectivity and neuroprotection (Lee *et al.*, 2003; Li *et al.*, 2016; Urrutia *et al.*, 2019). In addition, MSCs are easy to handle and demonstrate better survivability than compared to other stem cells (Bianco, Robey and Simmons, 2008; Nakaji-Hirabayashi, Kato and Iwata, 2013). However, a number of challenges for the application of MSCs in regenerative medicine persist and new approaches are needed to overcome them.

Mesenchymal stem cells (MSCs), otherwise known as mesenchymal stromal cells, are generally recognized as a heterogenous population of multipotent stromal progenitor cells with osteoblastic, adipocytic, and chondrogenic lineage differentiation capacity (Uccelli, Moretta and Pistoia,

2008). Despite significant debate with regards to their nature, MSCs meet general stem cell criteria – they possess self-renewal capacity, demonstrate plastic adherence, and present a specific set of surface markers, such as CD44 and CD105 (Maleki *et al.*, 2014). Since the original discovery of MSCs in the bone marrow, a plethora of tissues, including skeletal muscle, adipose tissue, and liver, have been shown to contain residing populations of MSCs in a perivascular localization (Crisan *et al.*, 2008). Consequently, the International Society for Cellular Therapy (ISCT) guidelines for identification of MSCs state that: i) MSCs must be purified from the stromal cell population of the bone marrow; ii) MSCs must not present hematopoietic lineage surface markers; iii) MSCs must demonstrate *in vitro* differentiation into osteoblasts, adipocytes, and chondrocytes (Dominici *et al.*, 2006). Some evidence suggests that MSCs can transdifferentiate into non-mesenchymal cell types, such as astrocytes or hepatocytes (Schwartz *et al.*, 2002; Wang *et al.*, 2004; George, Hamblin and Abrahamse, 2019). MSCs of the bone marrow remain the most well-studied and best characterized and are believed to be imperative in the physiological control of their tissue microenvironment (Kfoury and Scadden, 2015). They act as precursors to regulatory hematopoietic environment components, thus contributing to the homeostasis of the bone marrow and generating a niche for cells of the hematopoietic lineage. Immunomodulatory activity of MSCs has also been observed in some experiments (Li and Hua, 2017). The contribution of MSCs to their native environments is closely associated with their ability to differentiate into mesenchymal cell lineages (Liu, Xia and Li, 2015; Ambrosi *et al.*, 2017).

In the context of metabolic reprogramming, significant differences in metabolic modes can be observed between undifferentiated bone marrow MSCs and their differentiated progeny (Yuan, Logan and Ma, 2019). MSC localisation within hypoxic microenvironments coincides with their

preference for a highly glycolytic state. A low rate of ROS production coupled with abundant anabolic supply is highly advantageous for both quiescent and proliferating stem cells. Even under normoxic conditions, MSCs have been observed to retain HIF-1 α signaling and maintain aerobic glycolysis (Palomäki *et al.*, 2013). However, the presence of oxygen may also cause a switch towards a bimodal metabolic phenotype (Pattappa *et al.*, 2011). Osteogenic MSC differentiation is accompanied by a shift towards a more aerobic metabolism, with increased reliance on OXPHOS, although glycolysis levels are maintained to support osteoblast differentiation and biosynthetic demand (Shum *et al.*, 2016; Lee *et al.*, 2017; Wu *et al.*, 2017). Major observed changes during osteoblast formation include increases in electron transport chain enzyme activity, oxygen consumption rate, and mitochondrial DNA copy number (Chen *et al.*, 2008). In a similar fashion, MSC commitment to the adipocyte lineage is characterized by an early increase in mitochondrial metabolism and ROS production (Tormos *et al.*, 2011). As they mature, however, adipocytes display upregulated glycolysis and elevated levels of cytosolic acetyl-CoA, the latter being the result of increased ATP-citrate lyase (ACLY) expression in response to carbohydrate consumption (Fukuda, Katsurada and Iritani, 1992). Acetyl-CoA serves as a critical building block for glucose-fuelled *de novo* synthesis of both cholesterol and fatty acids, and is a key player in lipid storage and adipocyte epigenetics (Wellen *et al.*, 2009; Zhao *et al.*, 2016; Fernandez *et al.*, 2019).

1.4 Assessing pyruvate metabolism

As numerous cellular processes both in disease and health revolve around the management of cell bioenergetics, measurement of pyruvate metabolism provides valuable clinical insight on such processes. Most historical and conventional techniques employed in quantitating pyruvate include high-performance liquid chromatography (HPLC) (Minniti *et al.*,

1982; Ewaschuk et al., 2004), colorimetric and fluorimetric enzymatic assays (Neville et. al., 1971; Olsen et. al., 1971), and amperometric biosensors (Bergmann, Rudolph and Spohn, 1999). The choice in applied method usually depends on time and sensitivity required for a specific experiment. A recurring feature of the aforementioned methods is the *ex vivo* approach to clinical metabolite quantification, relying on biofluid extracts such as blood plasma, serum, or urine. Metabolite level measurement in these biofluids can serve as indicators of specific pathologies. For example, measurement of serum lactate levels is associated with increased risk of mortality in patients with cancer (Maher *et al.*, 2018). Other metabolic disorders, such as those associated with mitochondrial dysregulation, usually require tissue biopsy samples (Wibom, Hagenfeldt and Von Döbeln, 2002). However, a major limitation associated with these approaches is the lack of dynamic info on the flux of metabolites, a more reliable marker of *in vivo* metabolic change. It is now known that cells can undergo dramatic metabolic programme shifts during disease and/or life cycle progression. While univariate metabolite quantification can serve as a disease phenotype indicator, more powerful and less invasive tools are required to provide diagnostic data for early intervention planning.

The rising interest in MSC properties and applications in regenerative medicine requires effective selection techniques to identify populations of interest. As stated before, MSC populations in the highly heterogenous, coexisting in the same environment skeletal stem cells (cells that show no adipogenic capacity) and non-stem stromal progenitor cells (no self-renewal) (Uccelli, Moretta and Pistoia, 2008; Chan *et al.*, 2018). Effective characterization protocols are thus a necessity to overcome technical hurdles imposed by the nature of MSCs, such as low reproducibility over different cell batches, the demands of dealing with low/precious cell starting populations, and transition from bench-scale production to

engineering and manufacturing tissue products (Mao and Mooney, 2015). Currently, cellular and molecular analysis techniques, such as flow cytometry, immunostaining, and gene expression analysis are either damaging or destructive, offer slow through-put, and are not compatible with real-time monitoring (Mushahary *et al.*, 2018). Furthermore, biomarkers are in demand to allow imaging of MSC immune-mediated response in patients (Li and Hua, 2017). To date, reporter genes and nanoparticles have been used to track stem cells, but these approaches are limited by toxicity from ionizing radiation and potential compromising effect on cell function, respectively (Bhirde *et al.*, 2011; Jurgielewicz *et al.*, 2017). Finally, MSCs are now being used as an assessment platform for predicting cell toxicity in drug trials (Scanu, Mancuso and Cao, 2011). It has emerged that antineoplastic drugs have a negative effect on MSC replication, which may affect MSC behaviour and phenotype *in vivo* (Houthuijzen *et al.*, 2012). In order to better understand these toxic effects on MSCs and MSC-derived populations, new *in vitro* biomarkers of toxicity that can be translate into the *in vivo* setting are needed.

1.5 Metabolic phenotyping using nuclear magnetic resonance (NMR) spectroscopy

The phenotype of an organism describes how the sum of various parameters characterizes the functional biology of an individual. It is now recognised that the phenotype represents the result of complex crosstalk between the genetic factors of an individual and the external environmental factors, namely diet, aging, drugs, physical and psychological stress. Consequently, the metabolome of an individual is therefore descriptive of the phenotype at the molecular level (Fiehn, 2002). It is this connection that is the basis of the concept of metabolic phenotyping.

Metabolic phenotyping, also referred to as metabolomics, offers a

comprehensive snapshot of the thousands of metabolites present in biological fluids and/or cell extracts, as well as structural and quantitative data of individual molecules. This snapshot, termed the metabotype, represents the metabolic state of particular compartments (fluid or tissue) within an individual at any time point. Such an approach to metabolite identification and quantification is fundamentally different from targeted or univariate metabolic measurements. The key notion underlying the distinction between the two approaches is that the observation of a complex network of metabolites, as well as their fluctuations and interplay in response to various conditions, offers powerful diagnostic insight. Consequently, metabolic phenotyping has already been applied various mammalian systems, including humans, to investigate the metabolic dynamics associated with disease states, drug supplementation, and nutrition (Wishart, 2008; Wikoff *et al.*, 2009; Shah and Newgard, 2015; Zaitsev *et al.*, 2016). The ultimate goal of such studies is the identification of biomarker metabolites indicative of pathological or physiological phenotypes. Once the biomarkers are determined, the mechanistic knowledge of how specific phenotypes are generated can be inferred. Although metabolic phenotyping shows promising initial results in many areas of clinical practice in its current state, the lack of universal methodologies and insufficient validation persist as roadblocks for further metabolic phenotyping implementation in clinical settings (Robertson, Watkins and Reilly, 2011; Song *et al.*, 2019).

While metabolomics revolves around measuring large quantities of metabolites in any given biological system, the field of fluxomics seeks to obtain kinetic information about the observed metabolites. Specifically, fluxomic studies measure the metabolic flux, or the rate of metabolic conversion, of various biochemicals in biological systems. Various systems' biology tools, including genomics, transcriptomics, and proteomics, offer predominantly qualitative snapshots of cell component sets, thus

providing metabolic pathway indicators rather than quantitative data (Winter and Krömer, 2013). In contrast, fluxomics combines *in vivo* metabolic flux data with reaction stoichiometry, thus determining the absolute fluxes of metabolites to and from their respective pools. As the origin of metabolites relates to the upstream components of the genome, transcriptome, and the proteome, the analysis of metabolic fluxes provides quantitative information on biological mechanisms in health and disease. Like metabolomics, fluxomics is the study of small molecules, but involving isotopically labelled compounds with tracer functionality to determine the target set of metabolic fluxes. The standard fluxomics experimental method relies on introducing a ^{13}C -labeled metabolite into the biological system, followed by observation and measurement of the rate of incorporation of ^{13}C from the supplied precursor into other biochemicals. Inclusion of fluxomics as an additional layer of data has helped comprehend aerobic/anaerobic metabolic responses in *E.coli* and yeast (Celton *et al.*, 2012; Foster *et al.*, 2019). In studies involving mammalian cells and tissues, fluxomics data have given insights on key cellular mechanisms, such as cell cycle progression and cell differentiation (Ahn *et al.*, 2017). Despite the mutual distinction, metabolomics and fluxomics are two sides of the same coin - highly complementary approaches to answering complex biological and biochemical questions.

Two technologies are most prominent in the routine analysis of metabolic profiles in biological samples: nuclear magnetic resonance (NMR) spectroscopy and mass spectrometry (MS). NMR spectroscopy is a powerful and accurate tool used in metabolite detection, identification, and quantification. The great majority of metabolites have their own unique and reproducible NMR signature, therefore enabling spectroscopic analysis of hundreds of metabolites on a variety of human

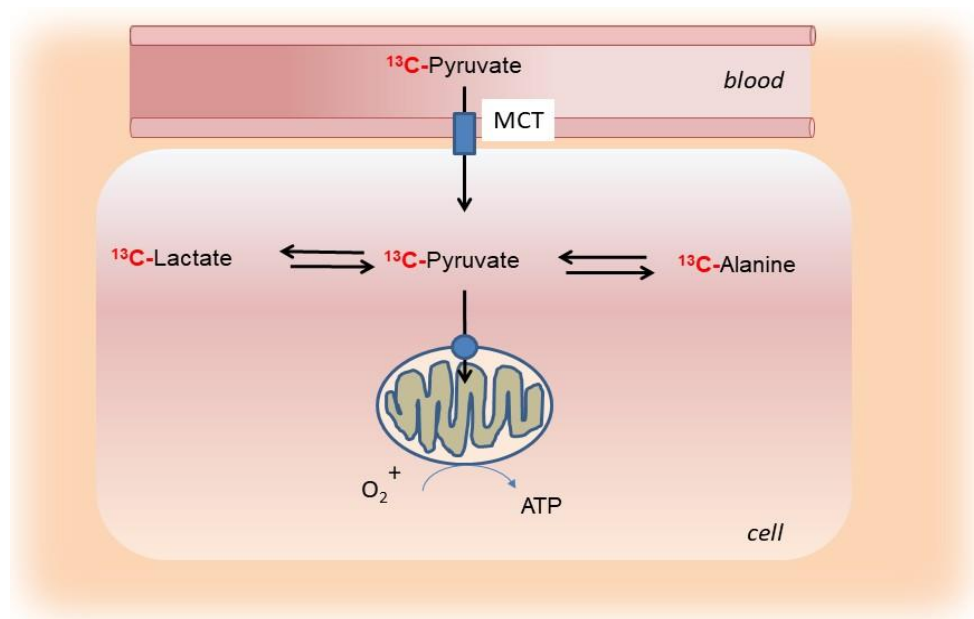


Figure 5: Example of ^{13}C label incorporation in a biological system. In a fluxomics study, a metabolite labelled with ^{13}C is introduced into a biological system, where it is metabolized. Consequently, the ^{13}C label gets transferred onto downstream molecules. The gradual increase in downstream label incorporation can be then detected by NMR spectroscopy, producing kinetics data. The given example demonstrates the ^{13}C label transfer from pyruvate to lactate and/or alanine.

samples, ranging from biofluids to tissues (Boesch and Kreis, 2000; Song *et al.*, 2019). Whereas biofluid analysis provides a more global overview of the body metabolism, tissue samples are more indicative of local responses to physiological or pathological stimuli. In contrast, MS-based approaches provide more sensitivity (nM-pM range vs μM -mM in NMR), particularly if coupled with liquid chromatography (LC) (Nagana Gowda and Djukovic, 2014; Emwas *et al.*, 2019). An LC-MS setup allows targeted metabolites to be quantitate even at levels as low as picomolar concentrations. Further differences between the two techniques lie in the cost and sample preparation. Typically, the costs associated with an NMR experiment prove to be less than those of MS (Bjerrum, 2015). Furthermore, no chemical or physical treatment of the sample is necessary when working with NMR, limiting the damage to the sample

and enabling reuse. Overall, the major advantages of NMR over MS are the high throughput capacity and reproducibility, all while maintaining comparatively low expenditures. Ultimately, however, the combined use of these two techniques can provide complementary analysis of the metabolome with the efficiency of NMR and the sensitivity of MS (Abd Ghafar *et al.*, 2020). In this study, we employed an NMR-based approach as we focused on the quantitative analysis of abundant soluble metabolites.

Table 1: Comparison of NMR and Mass Spectrometry techniques. The table summarizes the key differences between NMR and Mass spectrometry within seven key aspects.

	NMR	Mass spectrometry
Sensitivity	Low, but methods exist to improve signal (hyperpolarization, probe cryo-cooling, etc.)	High, metabolites can be detected at concentrations as low as nanomolar
Reproducibility	Highly reproducible	Less reproducible than NMR
Sample preparation	Simple, usually involves transfer to NMR tube and addition of deuterated solvent	More complex, usually requires chromatographic methods (liquid or gas)
Quantification	Intrinsically quantitative, metabolite signals are proportional to concentrations	Metabolite signals are not correlated with concentrations
Selectivity	Usually used for untargeted investigations, signal makes identification difficult	Very selective, especially in combination with chromatographic methods

Automation	Can be automated	Cannot be automated
Fluxomics	Both <i>in vitro</i> and <i>in vivo</i> flux analysis are possible	Possible, but limited by the destructive nature of MS methodology

To reveal metabolic status information of the sample, various nuclei have been employed, such as ^1H , ^{13}C , ^{31}P and ^{19}F . Many metabolomics studies rely on the measurement of ^1H NMR because of its relatively high sensitivity and significant natural abundance in most metabolites. Over the recent years, the improvements in NMR machinery and methodology have facilitated the extensive growth in metabolomic characterization. Developments of high-resolution NMR spectrometers (800MHz) and cryoprobes enable high-resolution NMR measurement with mass limited samples for *ex vivo* and *in vivo* samples (Voehler *et al.*, 2006; Alexandri *et al.*, 2017). Moreover, additions such as the 1D Nuclear Overhauser Effect Spectroscopy (NOESY) pulse sequence for water signal suppression, maximization of entropy to reduce experiment time, and improved probe design have significantly improved ^1H NMR-based metabolomics experiment outcomes. Meanwhile, nuclei like ^{13}C and ^{15}N have been predominantly used to monitor pathway regulation through metabolite enrichment with said nuclei (Nagana Gowda, Shanaiah and Raftery, 2019). However, the low intrinsic NMR sensitivity of ^{13}C and ^{15}N nuclei significantly extended the time required to obtain sufficient data on the metabolic flux rates. Furthermore, as fluxomics is focused on measuring time-associated changes in metabolites, it became essential to perform NMR studies in real-time using live organelle, cell, or tissue samples.

The application of hyperpolarization, the process of polarizing nuclear spins by altering the nuclei populations beyond their thermal equilibrium, has become a crucial approach for enhancing the low intrinsic NMR

sensitivity of ^{13}C nuclei and therefore ^{13}C NMR use for *in vivo* metabolite imaging (Chen *et al.*, 2020). The development of one particular method termed dynamic nuclear polarisation (DNP), has been a major breakthrough in hyperpolarization-assisted NMR metabolomics. Utilising low temperature, a strong magnetic field, and DNP, this approach strongly polarizes nuclear spins in the solid state (Ardenkjær-Larsen *et al.*, 2003). The subsequent rapid dissolution of the solid-state sample creates a solution of molecules with hyperpolarized spins, tremendously increasing the sensitivity of the signal. The overall result of this method is an increase in signal- to-noise ratio by over 10,000-fold, opening NMR up for easier *in vivo* application. With such a technique available, the prospect of *in vivo* NMR study presents feasibility.

^{13}C -labeled compounds are widely used in dissolution DNP studies because of their large chemical shift range and low natural abundance. One of the probes chosen for visualization of *in vivo* metabolic processes is pyruvate enriched with ^{13}C at the C1 position. This is due to the long T1 relaxation for the C1 carbon atom, allowing long retention of the signal (Merritt *et al.*, 2007). These *in vivo* studies depend on the sensitivity boost provided by the DNP method to visualize the different degree of conversion of pyruvate into alanine, lactate, or carbon dioxide, depending on the energetic status of the tissue. DNP has already been used to follow the kinetics of pyruvate metabolism in cancer cells and *in vivo* in breast cancer mouse models (Gutte *et al.*, 2015; Tran *et al.*, 2019; Granlund *et al.*, 2020). While NMR studies using cell cultures rely on culturing with $[1-^{13}\text{C}]$ pyruvate as energy substrate, *in vivo* studies supplement $[1-^{13}\text{C}]$ pyruvate through an intravenous (i.v.) injection. Following an i.v. injection, the ^{13}C -labelled pyruvate is rapidly distributed in the body and is absorbed by various organs and tissues. It is known that only insignificant amounts of the injected pyruvate leave the body through the regular excretory pathways, consequently ensuring the

complete metabolization of pyruvate within a short time of injection. Hyperpolarized ^{13}C pyruvate is converted to [1- ^{13}C] lactate, [1- ^{13}C] alanine and [1- ^{13}C] bicarbonate, and this is used to measure LDH, ALT and PDH activities in cells, respectively (Albers *et al.*, 2010; Serrao *et al.*, 2016, 2018). The relative amounts of metabolites produced from the injected pyruvate depends on the actual condition of the cells and a number of basic cell viability parameters, such as pO₂, pH, and need for protein synthesis.

1.6 Aims

In summary of current research, metabolic studies demonstrate great potential in fields of regenerative medicine, stem cell research, and neuroscience. In our study, we propose to use ^1H NMR to observe ^{13}C -labelled pyruvate metabolism in real-time to detect metabolic changes in mMSCs, wild-type mouse tissues, and Alzheimer's model mouse tissues. Our hypothesis is that the exchange of the ^{13}C label between pyruvate and downstream metabolites (lactate and alanine) can act as a biomarker in physiology and disease. In particular, we expect that the ratio between [1- ^{13}C]lactate and [1- ^{13}C]alanine could be representative of metabolic changes associated with cell differentiation, inflammation, and sexual dimorphism. Additionally, we aim to investigate upstream genomic and proteomic factors associated the observed metabolite signatures. Specific experimental objectives are as follows:

- Culture and differentiate mMSCs into mMSC-derived adipocytes and osteoblasts. (Section 3.1)
- After confirming effective differentiation via staining, enzymatic activity assays will be performed to evaluate LDH and ALT enzyme activities at specific timepoints during differentiation. (Section 3.2)
- At identical timepoints, ^1H NMR, qRT-PCR, and Western Blot

techniques will be applied, effectively generating multi-aspect (metabolic, genomic, and proteomic; respective to each technique) snapshots of mMSC differentiation. (Sections 3.3, 3.5 and 3.6)

- The same experimental approach will then be used to investigate wild-type and Alzheimer's disease model mouse tissues. Tissues will be collected, and their metabolic, genomic, and proteomic profiles will be analyzed via the same techniques. (Section 3.7 and onwards)
- For wild-type tissues, we will examine mouse brain, liver, adipose, and bone tissues. In the context of AD, we will look at liver and cortex tissues.
- Lastly, we will perform metabolomics testing of all gathered ^1H NMR data with the aim to detect any potential biomarkers outside of the pyruvate-associated pathways. (Sections 3.4, 3.8, and 3.12)

Our prediction is that mMSC-derived adipocytes and osteoblasts will present unique $[1-^{13}\text{C}]\text{lactate}/[1-^{13}\text{C}]\text{alanine}$ ratios, corresponding to differences in gene and protein expression. In wild-type tissue samples, we expect to see differences in reaction rates ($[1-^{13}\text{C}]\text{lactate}$ and $[1-^{13}\text{C}]\text{alanine}$ synthesis) and upstream factors (gene and protein expression), allowing distinction between tissues and cell phenotypes based on these factors. Lastly, in AD tissues, we will examine for any metabolic, proteomic, and genomic differences in pyruvate metabolism that arise due to sexual dimorphism and inflammation.

Chapter 2: Methods

2.1 Cell culture

2.1.1 Mesenchymal stem cell differentiation

The complete medium used to maintain undifferentiated mMSC cultures consisted of Dulbecco's Modified Eagle Medium (1g/L D-glucose) supplemented with 10% (v/v) fetal bovine serum, 1% (v/v) minimum essential medium (MEM) non-essential amino acid solution, 1% (v/v) L-glutamine 200mM and 1% (v/v) penicillin/streptomycin 10,000 U/mL (all from Thermo Fisher, UK). Our cells of choice for the experiment were of a murine bone marrow-derived D1 MSC cell line. Cell populations were split in a 1:2 ratio twice before being seeded for the experiment (at 0.2 million cells/cm² density). Cell populations were split using 0.05% Trypsin/Ethylenediaminetetraacetic acid (EDTA) (Thermo Fisher, UK) upon reaching ~75% confluency. For the first experimental replicate, the cells were thawed from -80°C storage at passage 22, while the second replicate used cells from passage 25. Cells were incubated at 37°C in 5% CO₂. To induce MSC differentiation, the complete medium was replaced with osteogenic or adipogenic medium. Osteogenic medium: 50mM ascorbic acid, 1M β-glycerophosphate, and 5mM dexamethasone in complete MSC medium (all from Cayman Chemicals, USA). Adipogenic medium: 10μg/mL insulin, 5mM dexamethasone, 0.1M isobutylmethylxanthine (IBMX) and 10mM rosiglitazone (all from Cayman Chemicals, USA) in complete MSC medium. Differentiation medium was regularly replenished (every 2 days). The same media and supplements were used throughout the study to ensure consistency. Analysis of all cell groups was performed at three timepoints: day 5, day 10, and day 13.

2.1.2 Alizarin Red staining and quantification

Osteogenic differentiation was confirmed using Alizarin Red (Sigma-Aldrich, UK) staining to detect matrix calcium deposits. Before staining, cells were washed with phosphate-buffered saline (PBS) and fixed for 10 minutes using 500µL of ice-cold 4% (v/v) paraformaldehyde (PFA) (Sigma-Aldrich, UK). Following fixation, cells were treated with 500µL of 1% Alizarin Red staining solution (distilled water-based) and incubated for 15 minutes at room temperature. Afterwards, the stained cells were washed with distilled water to remove any excess staining. To quantify the amount of staining, the cells were treated with 500µL of de-staining solution (20% methanol, 10% acetic acid) and a Tecan Infinity 200 PRO microplate reader (TECAN, Switzerland) was used optical density reading (absorbance measurement). Samples were spectrophotometrically analysed in triplicates, 100µL per well in a 96-well plate. Absorbance was measured at 405nm and was expressed in Relative Absorbance Units (a.u.). Images of the stained cells were acquired on a Nikon Eclipse TS100 light microscope (Nikon Instruments Inc., UK). Absorbance values were not normalized to the number of cells from each condition.

2.1.3 Oil Red O staining and quantification

Adipogenic differentiation was confirmed using Oil Red O staining to detect the presence of lipid vacuoles (Kraus *et al.*, 2016). In preparation for staining, cells were rinsed with PBS and fixed for 10 minutes using 500µL of ice-cold 4% (v/v) PFA. Afterwards, the cells were incubated in 500µL of staining solution containing the Oil Red O (Sigma-Aldrich, UK) stain for 15 minutes at room temperature. Then, cells were washed, first with 500µL of 60% isopropanol, and then with distilled water in order to remove excess staining before quantification. In preparation for quantification, cells were de-stained with 500µL of 60% isopropanol for around 3 minutes. Spectrophotometric analysis was performed at 510nm using a Tecan

Infinite 200 PRO microplate reader (TECAN, Switzerland). Samples were analysed in triplicates on a 96-well plate. Absorbance was expressed in Relative Absorbance Units. Images of stained cells were acquired via Nikon Eclipse TS100 light microscope (Nikon Instruments Inc., UK). Absorbance values were not normalized to the number of cells from each condition.

2.1.4 Alanine aminotransferase (ALT) activity assay

Triplicates of mMSCs were seeded in 6-well plates, each well containing 500,000 cells. Within each triplicate, two mMSC populations were induced to differentiate into osteoblasts and adipocytes (see section 2.1.1), while undifferentiated mMSC populations were used as control samples. The enzymatic activity of ALT was measured using a commercial assay kit (MAK052, Sigma-Aldrich, UK), following the protocol provided by the manufacturer. Trypsin treatment was used to harvest the cells (n=3 for each condition) and 1×10^6 cells were used for this assay. Cell samples were homogenized in 200 μ L of ALT assay buffer (Sigma-Aldrich, UK) and centrifuged at 15,000g for 10 minutes at room temperature to remove insoluble cellular debris. 20 μ L of the supernatant of each sample was transferred to a 96-well plate in duplicates. The enzymatic activity of ALT was quantified based on a colorimetric reaction induced by the reagents provided in the assay kit. Absorbance was measured at 570nm on a SpectraMax 190 microplate reader (Molecular Devices, USA). Measurements were taken every 5 minutes for 60 minutes at 37°C. ALT activity is expressed in moles per minute per mL (mU/mL).

2.1.5 Lactate dehydrogenase (LDH) activity assay

Triplicates of mMSC samples were seeded in 6-well plates, each well containing 500,000 cells. Within each triplicate, two mMSC populations were induced to differentiate into osteoblasts and adipocytes, while undifferentiated mMSC populations were used as control samples. The enzymatic activity of LDH was measured using a commercial assay kit,

following the protocol provided by the manufacturer. Trypsin treatment was used to harvest the cells (n=3 for each condition) and 1×10^6 cells were used of the assay. Cell samples were homogenized in 500 μ L of cold LDH assay buffer and centrifuged at 15,000g for 10 minutes at room temperature to remove insoluble cellular debris. 10 μ l of the of the supernatant of each samples was transferred to a 96-well plate in duplicates. The enzymatic activity of LDH was quantified based on a colorimetric reaction induced by the reagents provided by the reagents provided in the assay kit. Absorbance was measured at 450nm using a SpectraMax 190 microplate reader (Molecular Devices, USA). Measurements were taken every 2.5 minutes for 30 minutes at 37°C. LDH activity is expressed in moles per minute per mL (mU/mL).

2.2 Western blotting

2.2.1 Tissue sample collection

All procedures for tissue collection were approved by the Institutional Animal Care and Use Committee of University of Nottingham. All animals used in this study were bred and maintained at the University of Nottingham Biomedical Service Unit. Following a schedule 1 method of humane killing, brain, bone, fat (subcutaneous), and liver tissues were very rapidly (within 2-3 minutes) collected from a 4.5-month-old female wild-type C57BL/6J mice via dissection using tools cleaned with 70% IMS. Immediately following collection, tissue samples were snap frozen in liquid nitrogen. Samples were stored at -80°C for later use.

Samples of Alzheimer's model APP/PS1 mouse tissues (cortex and liver) were kindly provided by Dr Marie-Christine Pardon (Radde *et al.*, 2006). APP/PS1 mouse tissues were collected from 4.5-month-old male and female mice. Before tissue collection, APP/PS1 mice were subjected to lipopolysaccharide (LPS, E.coli serotype Sigma0111:B4, Sigma-Aldrich, UK) or PBS treatment (randomly allocated) (Agostini *et al.*, 2020).

Administration of treatment was through intravenous injection via lateral tail vein (100µg/kg of body weight of LPS or 1µl/g of body weight of PBS). 4 hours following the treatment, mice were culled. Tissues were collected via dissection. Collected mouse livers and cortex samples were snap frozen and stored at -80°C.

The C57BL/6J mice were not control littermates of the APP/PS1 mice. In the wild-type, we compared data between different tissues, while in APP/PS1 mice we looked at differences related to sexual dimorphism and inflammation in AD-affected tissues.

2.2.2 Preparation of lysate from tissues

Sample tissues were lysed in ice-cold radioimmunoprecipitation assay (RIPA) buffer (150mM NaCl, 50mM Tris-HCl, 1% Triton X-100, 0.5% sodium deoxycholate, 0.1% sodium dodecyl sulfate (SDS) (all from Sigma-Aldrich, UK), diluted to required volume with distilled water. Before use, the buffer was supplemented with cOmplete™ mini EDTA-free protease inhibitor tablets (Sigma-Aldrich, UK) at a ratio of 1 tablet per 10mL of buffer. Homogenization was performed using an IKA T10 basic ULTRA-TURRAX homogenizer (IKA® England LTD, UK). Following a 20-minute centrifugation at 12,000 rpm at 4°C in a microcentrifuge, the supernatant was aspirated and aliquoted for future use. Aliquoted lysates were stored at -80°C.

2.2.3 Protein Quantification – Bradford Assay

The Bradford Assay was employed to quantify protein abundance in tissue and cell lysates (Bradford, 1976). A bovine serum albumin (BSA) (Sigma-Aldrich, UK) stock solution of 50mg/ml was created by dissolving 0.5g of BSA powder in 10ml of distilled water. 80µL of the stock solution was added to 920µL of dH₂O to generate a standard with a concentration of 4000µg/mL. Serial dilutions were then performed to produce standards with the following concentrations: 2000µg/mL, 1000µg/mL, 500µg/mL,

250µg/mL, 125µg/mL, 62.5µg/mL, 31.25µg/mL, 15.625µg/mL, and 0µg/mL. The last standard contained only distilled water and was used as a negative control. Experimental samples were diluted 1:20 with distilled water. Both standards and experimental samples were run in triplicate in a 96-well plate, 10µl of per well. 250µl of Bradford Reagent dye (BioRad Laboratories, UK) was added to each well. After 10 minutes of color development on the bench, the plate was read at 595nm using a SPECTROstar Nano absorbance plate reader (BMG Labtech, Ortenberg, Germany). The raw data was then subsequently analysed in Excel (Microsoft, USA).

2.2.4 Sodium dodecyl sulphate–polyacrylamide gel electrophoresis (SDS-PAGE)

In preparation for SDS-PAGE, protein samples were mixed with 4x Laemmli (BioRad Laboratories, UK) working solution in the ratio of 1:3 (Laemmli to protein sample). The 4x Laemmli working solution consisted of 900µl of 4x Laemmli supplemented with 100µl β-mercaptoethanol (Sigma Aldrich, UK). Laemmli-stained protein samples were boiled at 95°C for 7 minutes before loading into the gel wells. The amount of protein loaded per well was 50µg. Gel electrophoresis was performed using the Mini-Protean Tetra Cell 1-D vertical kit (BioRad, UK). Proteins were separated based on their size using hand-cast gels. The resolving gel (10%) recipe: 6.3mL dH₂O, 5.3mL 30% acrylamide, 4mL 1.5M Tris pH8.8, 160µl 10% SDS, 160µl 10% ammonium persulfate, and 16µl N,N,N',N'-tetramethylethane-1,2-diamine (TEMED). Isopropanol was used to level the cell surface. Stacking gel (4%) recipe: 6mL dH₂O, 1.3mL 30% acrylamide, 2.5mL 0.5M Tris pH 6.8, 100µL 10% SDS, 100µL 10% APS, and 10µL TEMED (all from Sigma-Aldrich, UK). The larger pore size and a lower pH of the stacking gel ensured simultaneous entry of all protein samples into the resolving gel, where size-based separation of proteins

occurred. 4µl of Precision Plus Protein™ Dual Color Standard ladder (BioRad, UK) was used to identify protein weights. Gels were run at a constant 110 volts for 2 hours, until the migrating bands reached the end of the resolving gel.

2.2.5 Gel transfer

Immediately following the completion of SDS-PAGE, the resolved proteins were transferred onto a nitrocellulose membrane (0.45µm pore size) (BioRad, UK) using a wet transfer technique overnight. The gel was placed in a “transfer sandwich” (filter paper-gel-nitrocellulose membrane-filter paper), cushioned by sponge pads and held together by a support grid. The supported gel sandwich was placed vertically in a tank containing transfer buffer (25mM Tris-HCl, 192mM glycine, 20% methanol (v/v), pH adjusted to 8.3) and electrodes. Proteins were transferred overnight by running a constant 10V, 40mA current. Following the transfer, nitrocellulose membranes were blocked in 5% BSA (w/v) Tris-Buffered Saline (TBS) (Sigma Aldrich, UK) for 1 hour at room temperature or overnight at 4°C, aided by gentle rocking in both cases.

2.2.6 Immunoblotting

Following the blocking procedure (section 2.2.5), membranes were incubated in 5mL of primary antibody diluted in 5% BSA [w/v] TBS for 3 hours at room temperature. All incubation and wash steps were performed with gentle rocking. The loading control used for all samples was glyceraldehyde 3-phosphate dehydrogenase (GAPDH). After incubation with primary antibodies (Table 2), the membranes were washed 3 times in TBS-Tween 0.1% (v/v) for 5 minutes per wash. Membranes were then incubated with secondary antibodies (Table 2) diluted with 5% BSA (w/v) TBS for an hour at room temperature while protected from light with aluminum foil. Before imaging, the membrane was washed another 3 times using TBS-Tween. Fluorescent signals from

secondary antibodies were acquired via Odyssey FC Imaging System (LI-COR, UK) using dual-color detection at 700nm (red fluorescent range) and 800nm (green fluorescent range). The acquired images were analysed using Image Studio software (LI-COR, UK). The antibodies used in this study can be found in the tables below.

Table 2: List of primary antibodies. The list shows all the primary antibodies that were used to detect enzymes of interest in cells and tissues. All antibodies were diluted in 5% BSA (w/v) TBS.

Target	Host	Predicted molecular weight (kDa)	Dilution	Manufacturer
Lactate dehydrogenase A	Rabbit	35 kDa	1:5000	Abcam, UK
Alanine aminotransferase	Mouse	48 kDa	1:1000	Santa Cruz Biotechnology, UK
Pyruvate dehydrogenase α subunit	Rabbit	43kDa	1:1000	Cell Signaling Technology Inc., UK
Pyruvate dehydrogenase α subunit [p Ser 293]	Rabbit	43kDa	1:1000	Novus Biologicals, UK
Glyceraldehyde 3-phosphate dehydrogenase	Rabbit	37 kDa	1:1000	Cell Signaling Technology Inc., UK

Table 3: List of secondary antibodies. The list shows all the secondary antibodies that were used to detect enzymes of interest in cells and tissues. All antibodies were diluted in 5% BSA (w/v) TBS.

Target	Host	Dilution	Manufacturer
Anti-rabbit (700)	Donkey	1:5000	LI-COR, UK
Anti-rabbit (800)	Donkey	1:15000	LI-COR, UK
Anti-mouse (700)	Goat	1:5000	LI-COR, UK

2.2.7 Processing of immunoblot data

Fluorescent signal intensity of individual protein bands was identified using Image Studio software (LI-COR, UK). Target proteins band were recorded at 700nm, while the loading control was recorded at 800nm. Following normalization to the control, data was visualized in graphs using GraphPad Prism 8. One-way ANOVA tests were performed to compare signal means between sample groups. Tukey's multiple comparison was used as a post-hoc test to determine statistical significance

2.3 Quantitative reverse transcription polymerase chain reaction (qRT-PCR)

2.3.1 Sample preparation for RNA purification

The workspace was decontaminated with RNaseZap (Sigma Aldrich, UK) to prevent RNAase contamination of the workspace. For total RNA purification from wild-type (liver, brain, bone, adipose) and APP/PS1 (liver, cerebral cortex) tissues, ~50mg of each tissue was measured. Tissue samples were weighed on a scale while frozen using liquid nitrogen. If necessary, tissue was processed using a mortar and pestle. Liquid nitrogen levels were maintained in the mortar to prevent defrosting of the tissue. Tissue samples were then kept in RNAlater (Thermo Fisher, UK) and were allowed to thaw on ice.

In preparation for total RNA extraction from cells (controls mMSCs, mMSC-derived adipocytes and mMSC-derived osteoblasts) cells were treated with TRIzol (Invitrogen, UK) in 6-well plates (3 wells per cell group) and were incubated at room temperature for 10 minutes to allow thorough lysis. Afterwards, cell lysates were collected, pooled, and used for further RNA extraction (section 2.3.2).

2.3.2 Total RNA Purification

Total tissue RNA was purified using the RNeasy Mini Kit (Qiagen, UK). The

protocol was followed as described by the manufacturer. RNA concentration and purity were evaluated using the NanoDrop™ 2000 SpectroPhotometer (Thermo Fisher, UK). The absorbance of RNA was measured at 260nm, while wavelengths of 230nm and 280 were indicative of salt and protein contaminants, respectively. A260/A280 and A260/230 ratios were measured to determine adequate RNA purity and quantity, with both ratios being between 1.8 – 2.0 indicating acceptable levels. If necessary, the samples were diluted with nuclease-free water (Thermo Fisher, UK) to adjust the final RNA concentration levels. Optimal concentration for further experimentation was 500-1000 ng/μl. The entire procedure was carried out in the fume hood.

2.3.3 cDNA synthesis

cDNA was synthesized from the purified RNA. 2ng of RNA per sample group was used for the cDNA synthesis. The kit used was SuperScript™ III Reverse Transcriptase (Thermo Fisher, UK). 11.375μl volume samples were made up, containing 2ng of RNA and nuclease-free water. The reaction volume was topped up to 20μl by the following additions: 1.625μl Master Mix 1 (Random primers, 10mM dNTP mix), and Master Mix 2 (5X buffer, 0.1M DTT, RNase out RNase inhibitor, Superscript III reverse transcriptase) (all from Qiagen, UK). The recipes of master mixes can be found in the appendix. The final 20μl mix was inserted into the thermocycler, where the reaction was performed. In the thermocycler, a three step program was run: 25°C for 5 minutes, 50°C for 60 minutes, and 70°C for 15 minutes, in that order. Samples were kept on ice after the reaction was complete. Long term storage of cDNA was at -20°C.

2.3.4 Relative quantification

qRT-PCR was carried out to detect real-time amplification of genes of interest relative to reference gene (Gapdh), using SYBR™ Green Master Mix - PowerUp™ (Applied Biosystems, UK). Relative quantification of gene

expression was carried out for mMSC and AD tissue samples. All primers were used at 10 μ M concentration and aliquoted using the protocol provided by the manufacturer. Master mixes were made up for each target gene (Table 4). The experiment was run in 96-well PCR plate (ThermoFisher, UK), with duplicates for every individual gene of interest. 2 μ l of cDNA (section 2.3.3) was used per every well. The reaction was performed in a StepOne™ Real-Time PCR System (Thermo Fisher, UK). See appendix for thermocycling program.

Table 4: qRT-PCR master mix recipe.

Reagent	Volume (μ L)
Forward Primer (10mM working solution) (see	1
Reverse Primer (10mM working solution)	1
Ultra-Pure Nuclease Free Water	6
PowerUp™SYBR™ Green Master Mix	10
cDNA	2
Total volume per reaction	20

Forward and reverse primers for target genes were designed using Roche Universal ProbeLibrary Assay Design Center (Sigma-Aldrich, UK). Primer sequences for Ldha, Gpt1, Pdha1, and Gapdh are listed in the appendix. After completion of the qPCR programme, C_t of target genes were generated by integrated StepOne™ Real-Time PCR System software. Data was then transferred to Excel (Microsoft), where it was analysed using the ΔC_t method. Means of both the target gene and housekeeper gene (Gapdh) C_t values for each condition were calculated.

$$\text{Fold expression} = 2^{-\Delta C_t}$$

Where $\Delta C_t = C_t$ gene of interest – C_t internal control

Fold expression values were then normalised to a control value and

exported to and visualised in GraphPad Prism. One-way ANOVA tests alongside Tukey's multiple comparison post hoc test were used to compare means and determine statistical significance.

2.3.5 Absolute quantification

Due to varying expression of reference Gapdh gene across wild-type tissues, absolute quantification of gene expression was performed instead. cDNA generated from wild-type tissues was serially diluted in a 1:1 ratio with distilled water to generate standards (100ng/ μ l, 50ng/ μ l, 25ng/ μ l, 12.5ng/ μ l, 6.25ng/ μ l, 3.125ng/ μ l). These standards were plated in duplicates (2 μ l each). The same master mix and thermal program were used as in relative quantification. The data from the standards was used to generate standard curves for each target gene (ALT, PDH, LDH) in each tissue (brain, liver, adipose, bone). Standard curves consisted of standard Ct values plotted against log concentration of each standard. The Ct values of target genes acquired from wild-type tissues were then compared to the curve, allowing extrapolation of target replicon concentration.

2.4 Nuclear magnetic resonance (NMR) spectroscopy

2.4.1 Sample preparation for NMR

^1H NMR was used to measure ^{13}C -label incorporation in alanine and lactate in real time. On the day of the experiment, five solutions were made up: (i) 6mM glutamate, (ii) 3mM pyridoxal phosphate, (iii) 6mM NAD⁺, (iv) 1.2mM alanine, and (v) 6.4mM lactate. All the solutions were made up using an NMR buffer (40mM HEPES, 10mM nicotinamide, 0.1mM pyridoxal phosphate, 2mM DTT, and 0.2M KCl, pH corrected to 7.1 with KOH). The NMR buffer was specifically formulated to mimic intracellular conditions. Additionally, the buffer helped enhance pyruvate isotopic exchange by adjusting for metabolite concentration differences arising from the addition of ^{13}C -labelled pyruvate.

In preparation of the experiment, tissue samples (wild-type and Alzheimer's) were homogenized with ice-cold NMR buffer supplemented with cOmplete™ Mini EDTA-free protease inhibitor tablets (1 tablet per 10mL buffer, prepared separately) (Sigma Aldrich, UK). A ratio of 2ml of buffer per 1g of tissue was used to generate the homogenates. The only exception were the APP/PS1 cortex samples, for which the ratio was 10ml per 1g of tissue (due to small tissue amount). For mMSCs samples, they were washed with PBS and harvested via trypsinization. Following centrifugation at 1100rpm for 5 minutes, the resulting pellet was homogenized in 500µl of NMR buffer.

After a thorough resuspension with a 40mm gauge needle (SHD Medical, UK), all homogenates (mMSC, wild type and AD tissue) were centrifuged at 4000rpm for 15 minutes at 4°C. The supernatant from the post-centrifugation homogenate was used in the following NMR experiment.

2.4.2 Running the ¹H NMR experiment

The following reagents were mixed in a 5mm NMR tube (Sigma-Aldrich, UK):

Table 5: Sample composition for ¹H NMR experiment

Reagent	Amount
Pyridoxal phosphate, 3mM	20µL
NAD ⁺ , 6mM	40µL
Glutamate, 6mM	20µL
D ₂ O	35µL
Lactate, 6.4mM	30µL
Alanine, 1.2mM	20µL
TSP, 1mM	7µL
Tissue/cell extract	250µL
NMR buffer	185µL

The tube was then inserted into a Bruker 800MHz NMR spectrometer (Bruker, Germany), where data was acquired at 18.8T by applying a 1D Nuclear Overhauser Effect Spectroscopy (NOESY) pulse sequence to observe all ^1H - ^{13}C and ^1H - ^{12}C couplings. Example spectra can be found in the appendix. The pulse sequence included water suppression (pre-saturation), a 0.12s mixing time, a 12.5 second recycling delay, all the while averaging over 8 transients. Following an initial calibration run, the sample was briefly removed to allow addition of 10 μL of [$1\text{-}^{13}\text{C}$]pyruvate, after which the sample was reinserted into the magnet and the experiment was continued. Transfer of the ^{13}C label from pyruvate onto lactate and alanine was measured in real time by performing repeated data acquisition of the same sample every 2 minutes and 50 seconds. This was performed for at least two hours, or until a steady state plateau was identifiable in the metabolites of interest. ^{13}C methyl satellite signals were distinguished from ^{12}C methyl signals based on the ^{13}C coupling pattern (see Appendix). Sample temperature was maintained at 37°C at all times. Chemical shifts were referenced to 1mM of (3-(trimethylsilyl)-2,2',3,3'-tetradeuteropropionic acid (TSP; 0.0ppm). ^1H NMR data was analysed using MestReNova software (Mestrelab Research, Spain). Peaks of interest were integrated, and the area of the spectra were used to calculate changes in concentration in [$1\text{-}^{13}\text{C}$]pyruvate, [$1\text{-}^{13}\text{C}$]alanine, and [$1\text{-}^{13}\text{C}$]lactate at each timepoint. One-phase association functions were fit to the data points to calculate rates of [$1\text{-}^{13}\text{C}$]alanine and [$1\text{-}^{13}\text{C}$]lactate generation. The equation for the one-phase association curve fit:

$$Y=Y_0 + (\text{Plateau}-Y_0)*(1-\exp(-K*x))$$

Where:

Y_0 is the Y value when X is zero, expressed in the same units as Y,

Plateau is the Y value at infinite time, expressed in the same units as Y,

K is the rate constant, expressed in reciprocal of the X axis time units,

Tau is the is the time constant, expressed in the same units as the X axis.

It is computed as the reciprocal of K.

Concentration and rate constants were normalized for differences in proton number (9H^+ in TSP versus 3H^+ in both lactate and alanine). $[1\text{-}^{13}\text{C}]\text{lactate}/[1\text{-}^{13}\text{C}]\text{alanine}$ ratios were calculated. One-way and two-way ANOVA tests followed by Tukey's multiple comparison post hoc test were utilised to compare means and determine statistical significance, respectively.

2.4.3 Principal component analysis of ^1H NMR spectra

Principal component analysis was performed on the initial spectra (without $[1\text{-}^{13}\text{C}]$ pyruvate) in each dataset. The goal of this PCA was to identify any other metabolites outside of pyruvate-associated pathways that could potentially act as untargeted biomarkers for physiological and pathological conditions. Data pre-treatment and analysis was carried out using SIMCA-P software (Sartorius, Germany). Spectra used in PCA were binned (bucketed) into 0.04ppm-wide bins from 0.2ppm to 10ppm using the sum method in MestReNova. Noise levels were averaged from regions 0.24-0.84ppm and 9.48-10ppm and were subtracted from every individual bin. Negative bin values were set to 0. Each spectrum was then normalized by the total sum of all the cells within the spectrum. Data were mean-centered and auto-scaled to remove data offsets and equalize importance of all metabolites, respectively. Some data were excluded from PCA, including water, alanine, lactate, and pyruvate signals. This was to minimize the effect of metabolite additions through buffers on the final PCA model. Score plots generated by PCA allowed observation of similarities and differences between samples, while loading plots provided insight on metabolic factors affecting the scores. PCA results were

evaluated based on parameters R^2X (amount of data explained by PCA) metric and Q^2 (predictive power of the PCA model)

2.5 Statistical analysis

Results from all experiments were expressed as mean (n=3) \pm SEM. All statistical analysis and data visualization (except for PCA) was performed using GraphPad Prism 8 (GraphPad Software, USA). One-way and two-way ANOVA followed by post hoc Tukey's multiple comparisons tests were used to determine statistical significance between different groups. A p value of <0.05 was used a marker of significance.

Chapter 3: Results

3.1 Adipogenic and osteogenic differentiation of mouse mesenchymal stem cells (mMSCs) *in vitro* was successful.

To investigate pyruvate metabolism of mouse mesenchymal stem cells (mMSCs) and their differentiated cells, we developed a chemically induced experiment model of mesenchymal differentiation *in vitro*. Similar models are described in literature (Gimble *et al.*, 2008; Lai *et al.*, 2017). Differentiation was driven by addition of chemical supplements to cell culture media during cell growth (section 2.1.1). Cell culture staining using Alizarin Red and Oil Red O (sections 2.1.2 and 2.1.3) was used to evaluate the progression of mMSC differentiation on days 10 (Figure 6) and 13 (Figure 7) for all conditions. The Oil Red O (ORO) stain was used to observe lipid vacuole production (characteristic of adipocytes), while Alizarin Red (AR) staining identified formation of a calcium-enriched mineralized matrix (characteristic of osteoblasts) in cell cultures. Staining of mMSC populations was quantified using relative absorbance at 570nm (ORO stain) and 405nm (AR stain). While a mineralized matrix was only present in osteogenically-induced mMSCs, varying levels of ORO staining were detected across all experimental groups on both days 10 and 13. The greatest level of ORO absorbance was observed in adipogenically-induced mMSCs, with lower levels seen in both control and osteogenic mMSCs (Figures 6G and 7G). Through image analysis, an absence of lipid vacuoles in mMSCs was identified, suggesting incomplete stain removal during the washing steps of the staining protocol. Conversely, lipid vacuoles were present in mMSC-derived osteoblasts, although at a level significantly lower than observed in adipogenic mMSCs.

3.2 mMSC differentiation into adipocyte and osteoblast lineages is associated with changes in LDH and ALT activities.

At days 10 and 13 of mMSC differentiation, enzymatic assays were

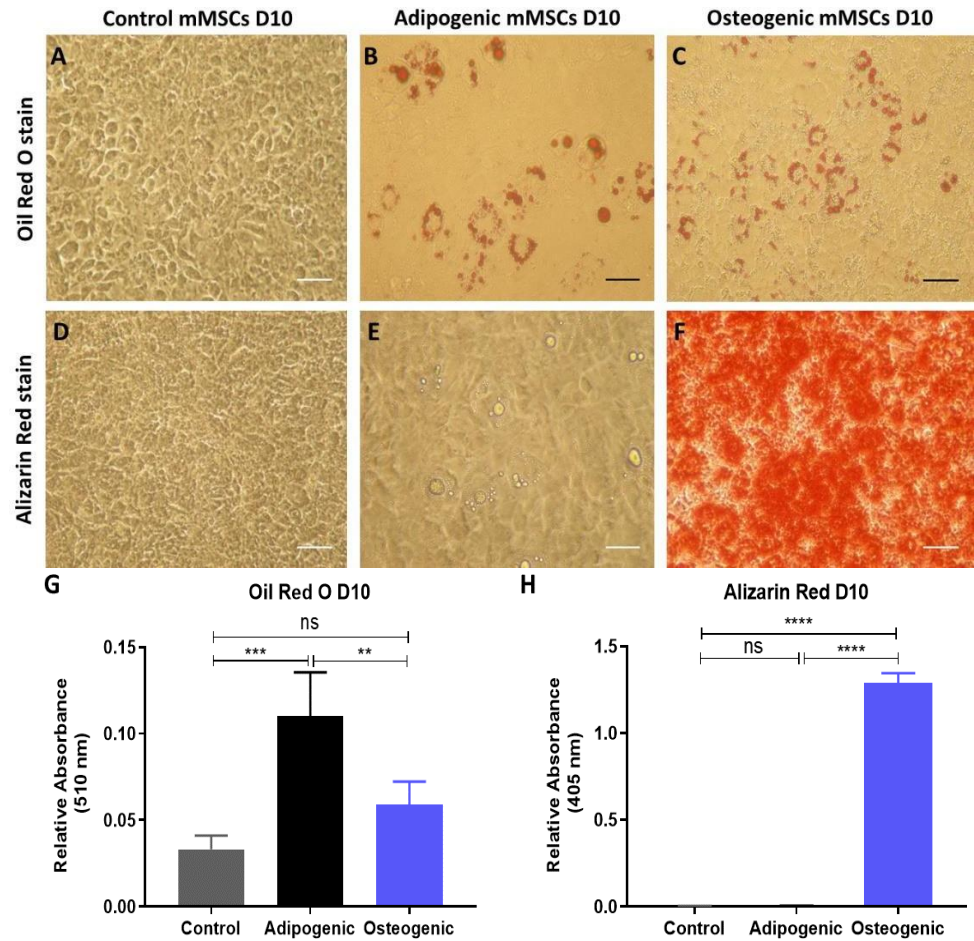


Figure 6: ORO and AR staining of control and differentiated mMSC populations at day 10 of differentiation *in vitro*. Images A-C represent staining of lipid vacuoles by the Oil Red O stain in control mMSCs (A), adipogenic mMSCs (B), and osteogenic mMSCs (C). Images D-F show the staining of calcium deposits by the Alizarin Red stain in control mMSCs (D), adipogenic mMSCs (E), and osteogenic mMSCs (F). Scale bars = 50nm. Bar charts G and H show the quantification of both Oil Red O and Alizarin Red stain absorbances at 510nm (G) and 405 (H), respectively. N=3; One-way ANOVA, error bars \pm SEM; **** $p \leq 0.0001$, *** $p \leq 0.001$, ** $p \leq 0.01$; ns $p \geq 0.05$.

employed to measure ALT and LDH activity levels in control, adipogenic, and osteogenic mMSC populations. In terms of ALT activity, little to no significance was seen in the differences between all experimental groups on day 10 (Figure 8A). Similar results were seen in the LDH assay, where no significance was seen in LDH activity variation on day 10 (Figure 8C).

However, changes in ALT and LDH activities were clearly visible on day 13. The highest ALT activity was observed in the osteogenic mMSC group (4.5mU/mL), followed by adipogenic (2.7mU/mL) and control groups (1.35mU/mL) (Figure 3B). In contrast, the highest LDH activity was detected in mMSC-derived adipocytes (132.5mU/mL), with the osteoblasts (77.78mU/mL) and control mMSCs (39.78mU/mL) showing significantly lower LDH presence (by 54.72 mU/mL and 92.72mU/mL, respectively) (Figure 8D).

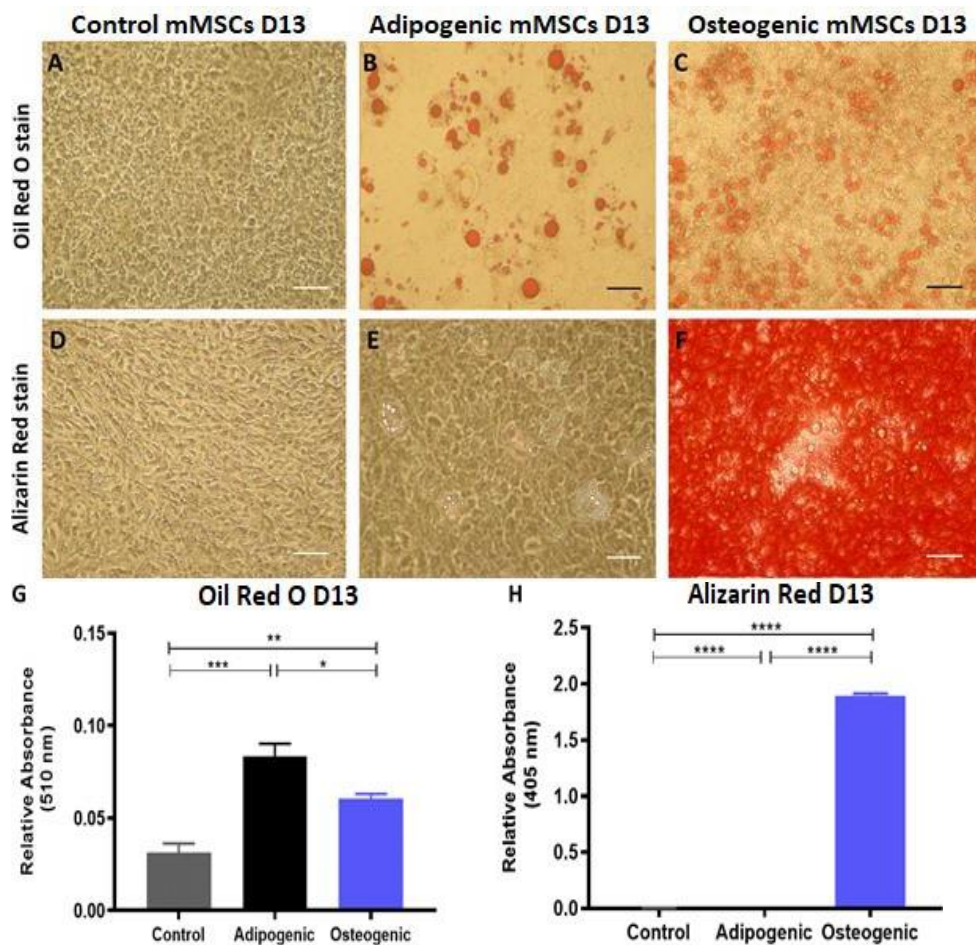


Figure 7: ORO and AR staining of control and differentiated mMSC populations at day 13 of differentiation *in vitro*. Images A-C represent staining of lipid vacuoles by the Oil Red O stain in control mMSCs (A), adipogenic mMSCs (B), and osteogenic mMSCs (C). Images D-F show the staining of calcium deposits by the Alizarin Red stain in control mMSCs (D), adipogenic mMSCs (E), and

osteogenic mMSCs (F). Scale bars = 50nm. Bar charts G and H show the quantification of both Oil Red O and Alizarin Red stain absorbances at 510nm (G) and 405 (H), respectively. N=3; One-way ANOVA, error bars \pm SEM; **** $p \leq 0.0001$, *** $p \leq 0.001$, ** $p \leq 0.01$; * $p \leq 0.05$.

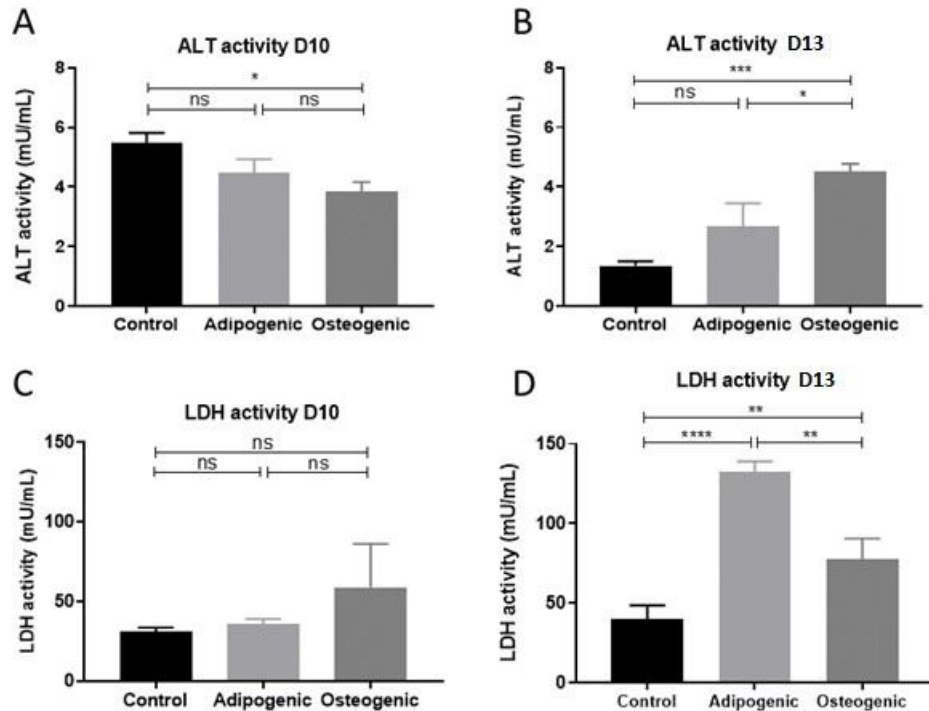
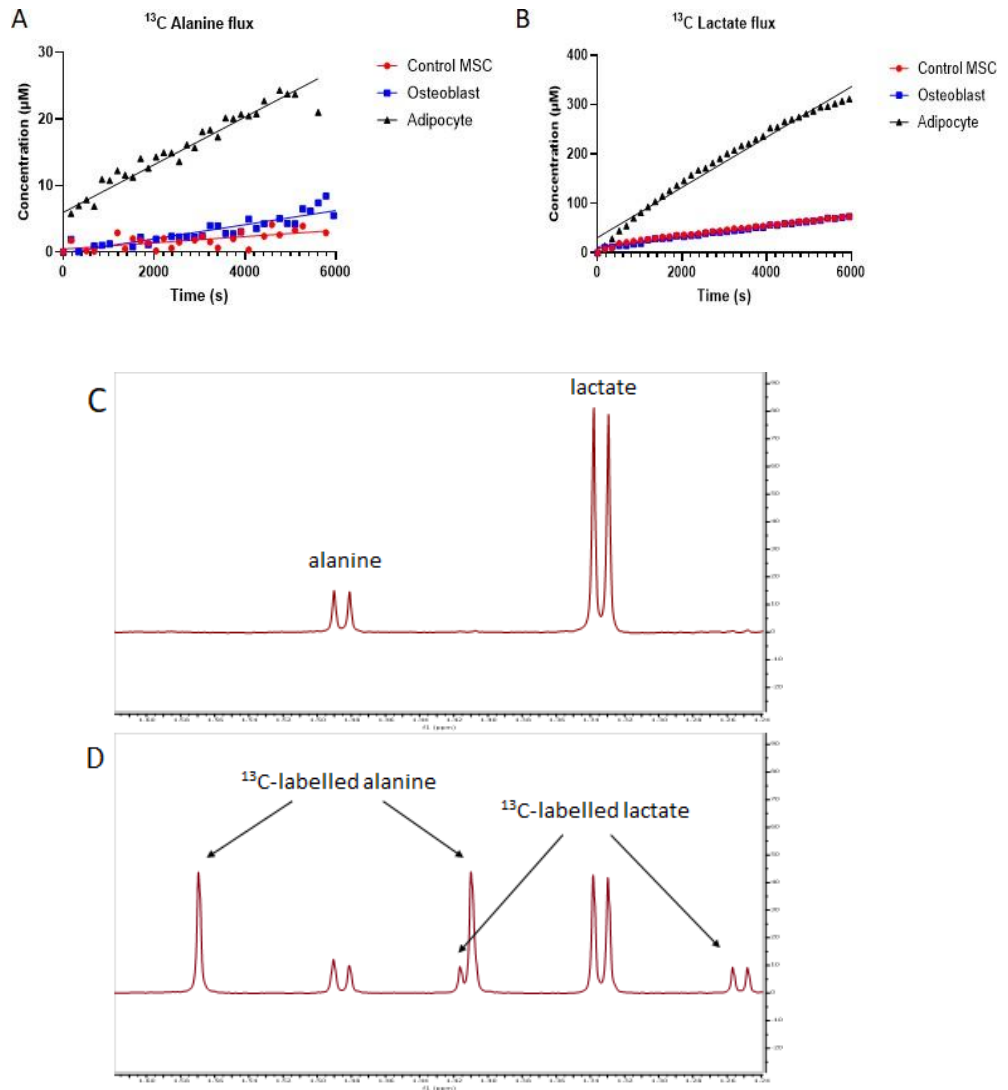


Figure 8: Changes in ALT and LDH activity associated with mMSC differentiation *in vitro*. Bar charts represent the results of ALT and LDH activity assays of all experimental groups (n=3). Graphs A and B represent ALT activity in control, adipogenic, and osteogenic cell groups at days 10 and 15, respectively. Graphs C and D represent LDH activity in the same cell groups at days 10 and 15. N=3; One-way ANOVA, error bars \pm SEM; **** $p \leq 0.0001$; *** $p \leq 0.001$; ** $p \leq 0.01$; * $p \leq 0.05$; ns $p > 0.05$.

3.3 ^1H NMR observation of ^{13}C label incorporation into alanine and lactate can be used as biomarker of mMSC lineage determination during differentiation

Building on the results of the enzymatic assays, ^1H NMR spectroscopy was performed at day 10 on all experimental cell groups to determine the exchange of ^{13}C label from $[1-^{13}\text{C}]$ pyruvate to generate $[1-^{13}\text{C}]$ lactate and $[1-^{13}\text{C}]$ alanine. A linear increase in both $[1-^{13}\text{C}]$ lactate and $[1-^{13}\text{C}]$ alanine

was observed in all three cell groups following addition of ^{13}C labelled pyruvate (Figure 9A and 9B). In adipocytes, the concentration of $[1-^{13}\text{C}]$ alanine and $[1-^{13}\text{C}]$ lactate increased during the experimental time to $21.75 \pm 0.72 \mu\text{M}$ and $359.77 \pm 26.65 \mu\text{M}$, respectively. These numbers were much higher than the ones seen in control MSCs $23.25 \pm 19.343 \mu\text{M}$ for $[1-^{13}\text{C}]$ alanine; $92.79 \pm 17.96 \mu\text{M}$ for $[1-^{13}\text{C}]$ lactate) and osteoblasts ($2.81 \pm 0.84 \mu\text{M}$ for $[1-^{13}\text{C}]$ alanine; 90.69 ± 10.4 for $[1-^{13}\text{C}]$ lactate). Label exchange ratios between $[1-^{13}\text{C}]$ lactate and $[1-^{13}\text{C}]$ alanine were calculated and revealed that adipocytes can be clearly distinguished from control MSCs and osteoblasts using these ratios (Figure 9E).



E

	¹³ C label transfer rate from [1- ¹³ C pyruvate] to alanine, nM/sec	¹³ C label transfer rate from [1- ¹³ C]pyruvate to lactate, nM/sec	1- ¹³ C]lactate/[1- ¹³ C]alanine ratio
Control MSCs	4.05 ± 2.06	13.44 ± 1.63	3.31 ± 0.79
mMSC-derived adipocytes	3.14 ± 0.09	55.24 ± 2.52	17.58 ± 0.31 ***
mMSC-derived osteoblasts	0.57 ± 0.23	12.99 ± 1.18	22.52 ± 5.13

Figure 9: Distinction between mMSC-derived adipocytes and osteoblasts using ¹H NMR and ¹³C-labelled pyruvate. Plots A and B show measurements acquired using ¹H NMR spectroscopy to observe ¹³C label exchange from pyruvate to lactate and alanine at day 10 of differentiation. Representative data are shown, one set from each control MSC (red), adipocyte (black), and osteoblast (blue) experiment. Example NMR spectra in images C (pre-pyruvate addition) and D (post-pyruvate addition, end of time course) show a region of the spectrum where alanine and lactate signals are found (between 1.24ppm and 1.60ppm). The arrows indicate the identities of the peaks. The table (E) shows a summary of ¹³C label exchange rates between specific metabolites; (n=3 for each experimental group). Values in the table are shown as means ± SEM. *** - significant against all other groups, p<0.001.

3.4 Distinction of metabolic profiles in mMSC-derived populations using principal component analysis (PCA)

Multivariate analysis of baseline spectra acquired from all mMSC sample groups revealed that overall metabolic profiles of osteoblasts and adipocytes (excluding the pyruvate-associated pathways) were quite distinct. As seen in the score plot from the PCA analysis (Figure 10A), adipocyte and osteoblast populations are clearly separated by principal component 1. Control mMSC metabolic profiles were similar to osteoblasts but were overall more centrally located. Principal component 2 separated some outliers within cell groups, likely based on inconsistencies in

repeated experiments. Moreover, the loadings plot provided insight on which data buckets within the spectra were the cause for cell profile separation (excluding pyruvate-associated metabolites). Adipocyte metabolic phenotypes seemed to be linked to bins 3, 3.92, and 3.2. Conversely, on the osteoblast side, bins 3.16, 3.84, 3.68, and 3.76 seemed to be the key variables. Metabolites contained within the aforementioned bins could therefore present biomarker potential. In terms of quality metrics, principal components 1 and 2 described 62.7% and 22.8% of observed variance, respectively, as indicated by the R2X[1] and R2X[2] values shown under the plots. A cumulative R2X value (0.855) suggested that this model explained the data provided quite well. A third principal component was deemed unnecessary due to lack of significant effect on the cumulative R2X value. Additionally, the Q2 value (0.634) indicated that this model has good predictive power in terms of explaining any future data, but still lacked robustness ($Q2 < 0.7$).

3.5 mMSCs indicated fluctuations in gene expression during mesenchymal differentiation.

Following analysis of metabolic profiles in mMSCs, adipocytes, and osteoblasts, we performed qRT-PCR analysis to investigate changes in LDH, ALT, and PDH expression at a genomic level. Our goal was to determine whether any alterations in the expression of these genes in adipogenic and osteogenic lineages occur in parallel to the metabolic changes observed by ^1H NMR. We observed unique gene expression patterns between in both adipocytes, and osteoblasts. Heatmaps were generated to showcase gene expression changes at all three different timepoints (Figure 11). Gene expression data were expressed as fold difference. All data were normalized to and compared to the control group. A two-way ANOVA was used to determine significance of the data.

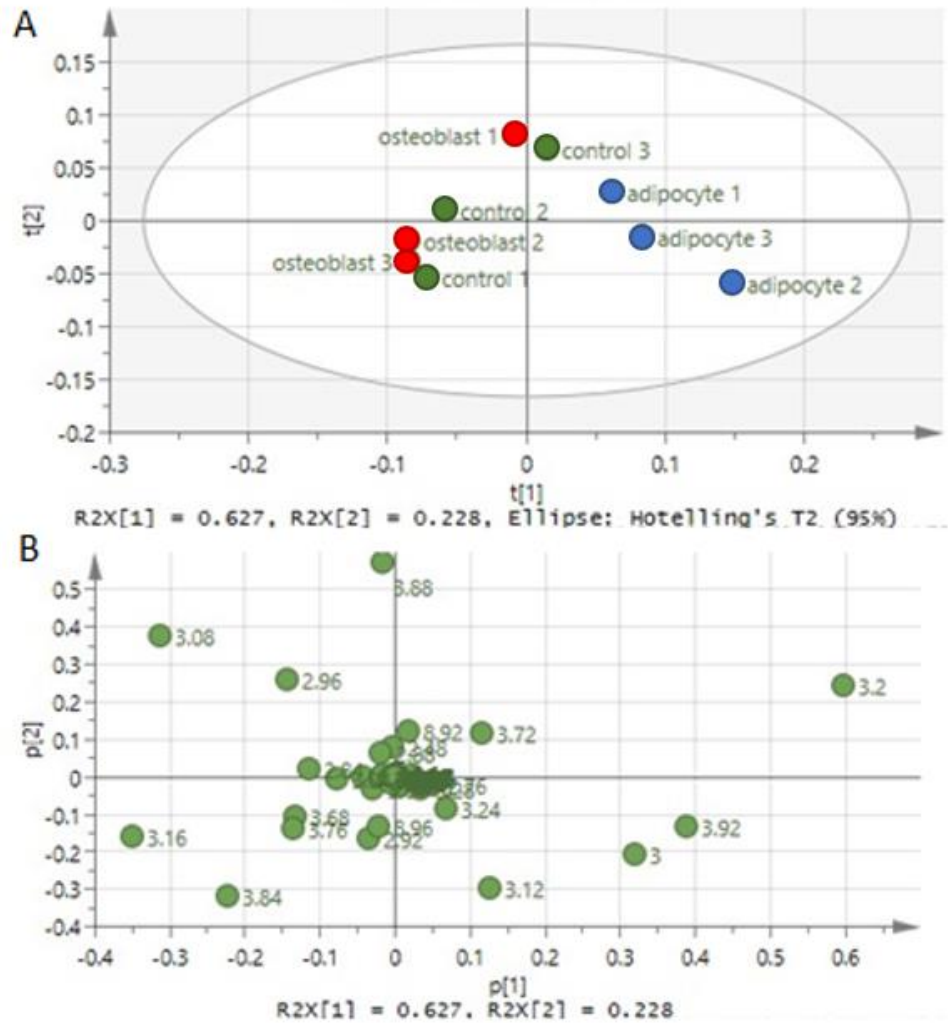
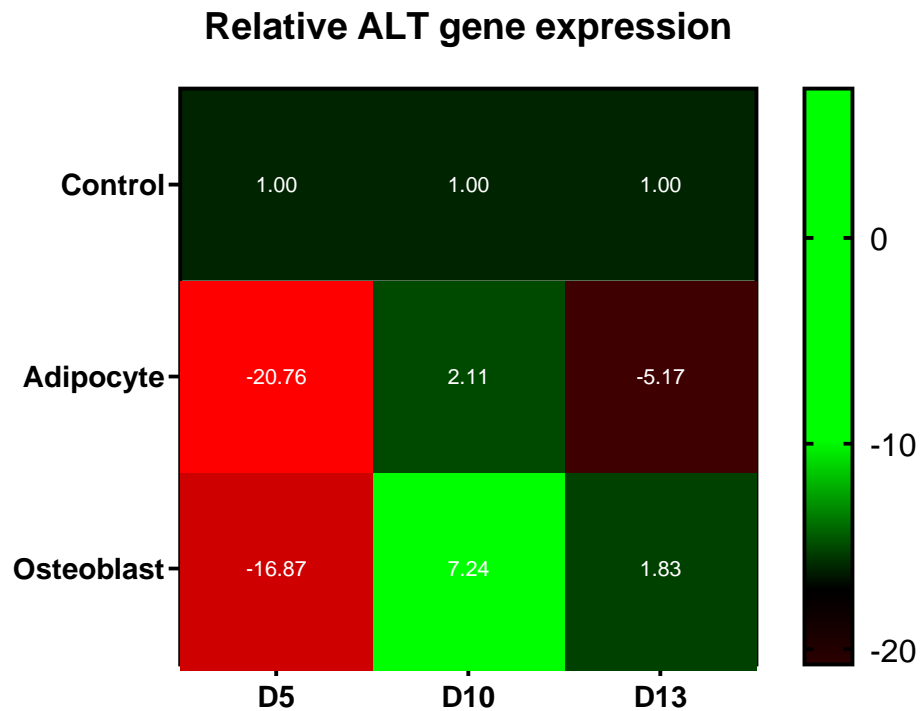


Figure 10: Principal component analysis of mMSC populations. Data were gathered from pre-pyruvate addition spectra and normalized to total sum. A – the scores plot, showing how the observations were distributed on the two principal component axes. Green – control group, blue – adipocytes, red – osteoblasts. B – the loadings plot, showing how the variables were distributed on the two principal component axes. At the bottom of both pictures, the cumulative R2X values provided by each principal component can be seen. t[1]– principal component 1; t[2] – principal component 2. n=3 for each cell group.

As shown in Figure 11, the expression levels of all three target enzymes varied highly over time in adipocytes and osteoblasts. At day 5, both adipocytes and osteoblasts showed a smaller fold change in ALT gene expression vs control MSCs (-20.76, p=0.0055 and -16.87, p=0.0219,

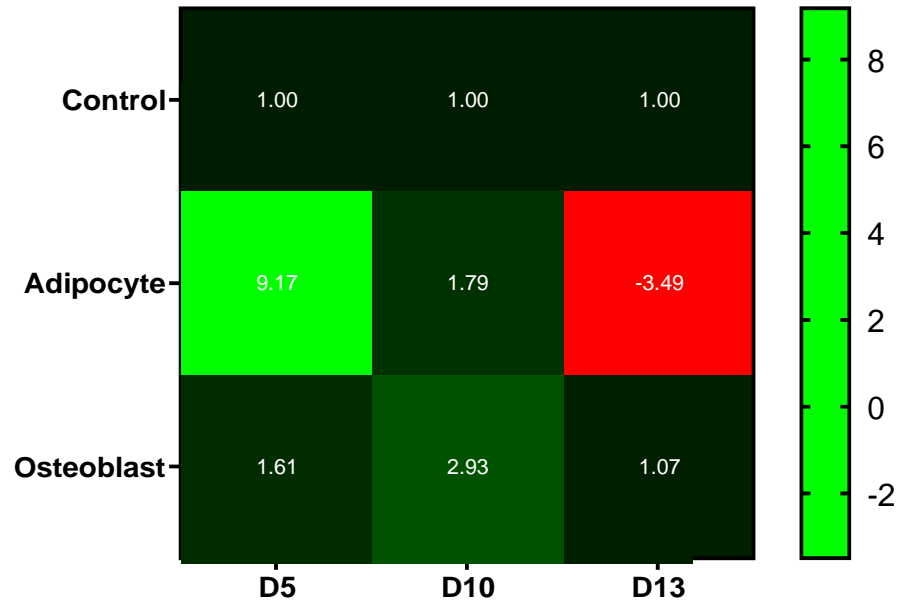
respectively) (Figure 11A). Having reached day 10, ALT gene expression in adipocytes and osteoblast had surpassed that of the control group (-20.76 to 2.11, $p>0.05$ and -16.87 to 7.24, $p>0.05$, respectively (two-way ANOVA)). Finally, at day 13, adipocytes seemed to again show smaller fold changes in ALT gene expression (2.11 to -5.17, $p>0.05$) compared to control MSCs, whilst osteoblasts maintained expression above the control group (7.24 to 1.83, $p>0.05$). In sum, the data suggests an upregulation of ALT expression in osteogenically-induced mMSCs over the course of differentiation. This is likely representative of a shift towards a more biosynthetic metabolism commonly observed in osteoblasts. However, no significant differences between adipocytes and osteoblasts in terms ALT gene expression were seen at any timepoint ($p>0.05$).

A



B

Relative LDH gene expression



C

Relative PDH gene expression

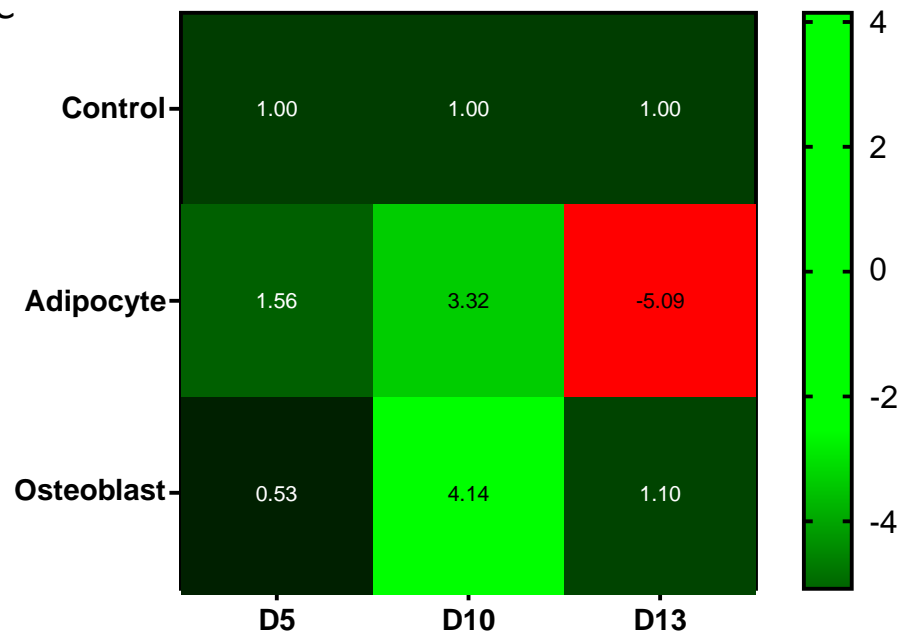


Figure 11: Gene expression heatmaps in cultured mMSCs and mMSCs-derived adipocytes and osteoblasts. Each heatmap represents a specific gene, as indicated by the graph titles. Values in the cells indicate mean expression fold difference values compared to the control group. Heatmaps A, B, and C represent ALT, LDH, and PDH data, respectively. All data were normalized to GAPDH. ALT – alanine aminotransferase; LDH – lactate dehydrogenase; PDH – pyruvate dehydrogenase; D5 – day 5 of differentiation; D10 – day 10 of differentiation, D13 – day 13 of differentiation. N=3.

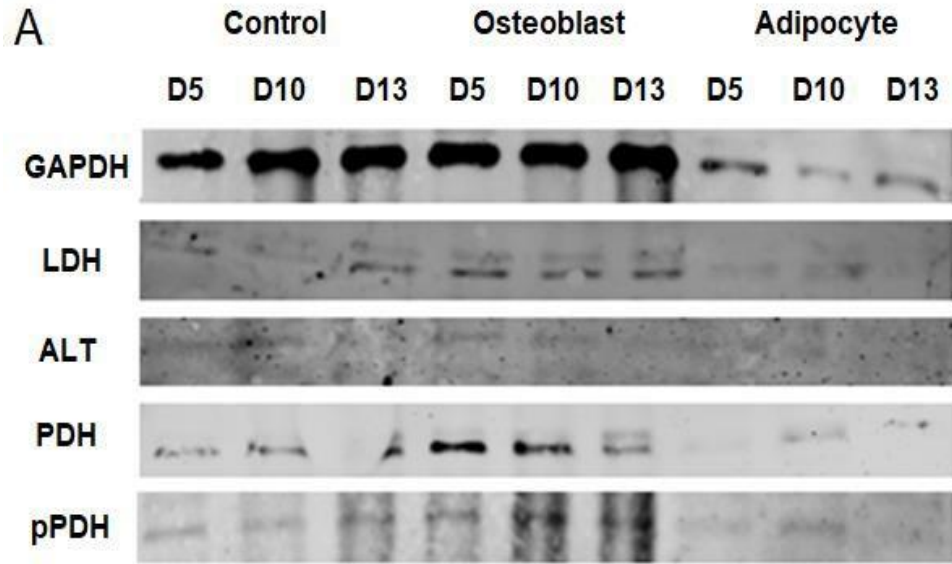
LDH gene expression in adipocytes experienced a steady decline over the differentiation time course (9.17, $p < 0.0001$ to 3.32, $p > 0.05$ to -5.09, $p < 0.0001$ at days 5, 10, 13, respectively) compared to the control group (Figure 11B). Meanwhile, osteoblast expression of the LDH gene followed a similar pattern to the ALT gene - from day 5 to day 10, we saw an LDH gene expression level change from 1.61 ($p > 0.05$ vs control) to 2.93 ($p = 0.0028$ vs control). At day 13, however, there was a decrease in osteoblast LDH gene expression (2.93 to 1.07-fold, $p > 0.05$), very similar to the level of LDH gene expression in the control group. Days 5 and 13 were also timepoints of significant difference between adipocytes and osteoblasts in terms of LDH gene expression ($p < 0.0001$ at both timepoints). It can be inferred that osteoblasts maintain a glycolytic bioenergetic profile similar to undifferentiated mMSCs, while adipocytes shift away from lactate production as differentiation progresses.

Similar patterns to those seen in ALT and LDH genes expression were also seen in PDH expression. From day 5 to day 10, PDH gene expression increased in both adipocyte and osteoblast populations (1.56 to 3.32, $p > 0.05$ in adipocytes, 0.53 to 4.14, $p > 0.05$ in osteoblasts) compared to the control MSCs. However, none of these changes showed statistical significance. At day 13, following decreases in PDH expression in both adipocytes (3.32 to -5.09, $p = 0.0029$) and osteoblasts (4.14 to 1.10, $p > 0.05$),

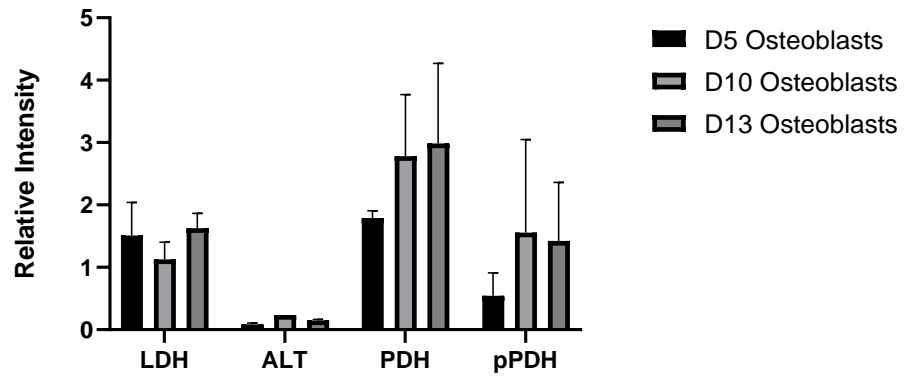
significance could be seen between adipocyte and osteoblast populations ($p=0.0025$). These findings suggest an upregulation of OXPHOS in both adipocytes and osteoblasts at D10. As with LDH, osteoblasts seem to maintain a similarity to the control group, while adipocytes develop a more distinct profile of pyruvate metabolism.

3.6 Levels of proteins involved in pyruvate metabolism indicate minimal differentiation-associated changes.

To complement the metabolic and genomic data acquire from NMR and qPCR, Western blots were employed to determine any changes in pyruvate-associated enzyme expression. Chosen target enzymes were ALT, LDH, PDH, and pPDH. pPDH is a phosphorylated version of PDH with a phosphate residue attached to serine residue 293- a region where PDH is commonly inactivate through pyruvate dehydrogenase kinase activity. As seen in Figure 12A, detection of target enzyme via immunoblotting was successful overall. Some enzymes, such as ALT and pPDH, displayed very low abundance, although still within quantifiable range. ALT enzyme levels seemed to be in accordance with low ALT enzymatic activity (see above). Based on the blots, statistical analysis (two-way ANOVA) was performed to determine whether the visual differences observed – variance in enzyme presence withing differentiated mMSC groups and over time – were substantial. The data used for statistical analysis was based on the relative intensity of the bands seen in the pictured blots. Looking at the data gathered within groups, no substantial changes in the levels of LDH, ALT, PDH and pPDH in both adipocytes and osteoblasts were seen during differentiation. In osteoblasts, LDH and ALT seemed to maintain mostly stable levels (1.509 ± 0.53 at day 5, 1.128 ± 0.27 at day 10, 1.627 ± 0.23 at day 13 for LDH; 0.085 ± 0.02 at day 5, 0.233 ± 0.001 at day 10, 0.147 ± 0.01 at day 13 for ALT). There was a moderate increase in PDH and



Enzyme expression in osteoblasts



Enzyme expression in adipocytes

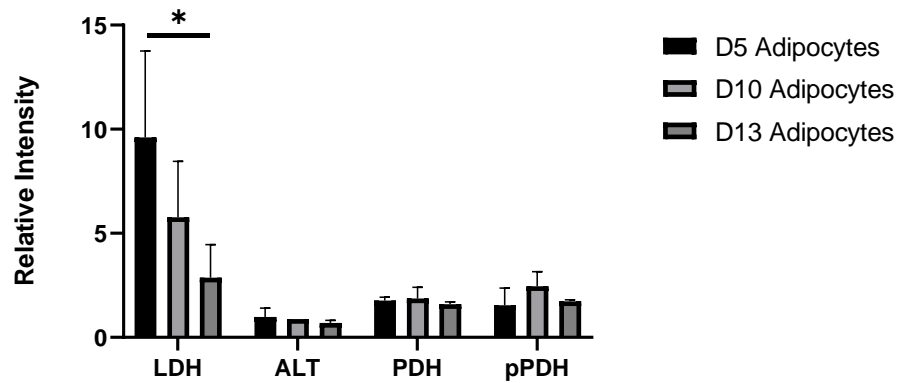


Figure 12: Western blotting results in cultured and differentiated mMSCs. A – representative images of protein blots acquire via LI-COR imaging. Well identities are indicated above, while the enzyme names of corresponding

images are shown on the left. Enzymes sizes in respective bands are shown on the right. This set of data is representative of one experimental repeat. GAPDH signal intensity was measured at 800nm, while LDH, PDH, and ALT were measured at 700nm. B and C – quantified data of enzyme expression in osteoblasts and adipocytes, respectively. Relative intensity of antibody fluorescence was measured via densitometric analysis (expressed in arbitrary units). Values shown are mean (n=3) ± SEM. Both groups were normalized to the control MSC group data at the D5 timepoint. *p<0.05. All unspecified multiple comparisons were non-significant.

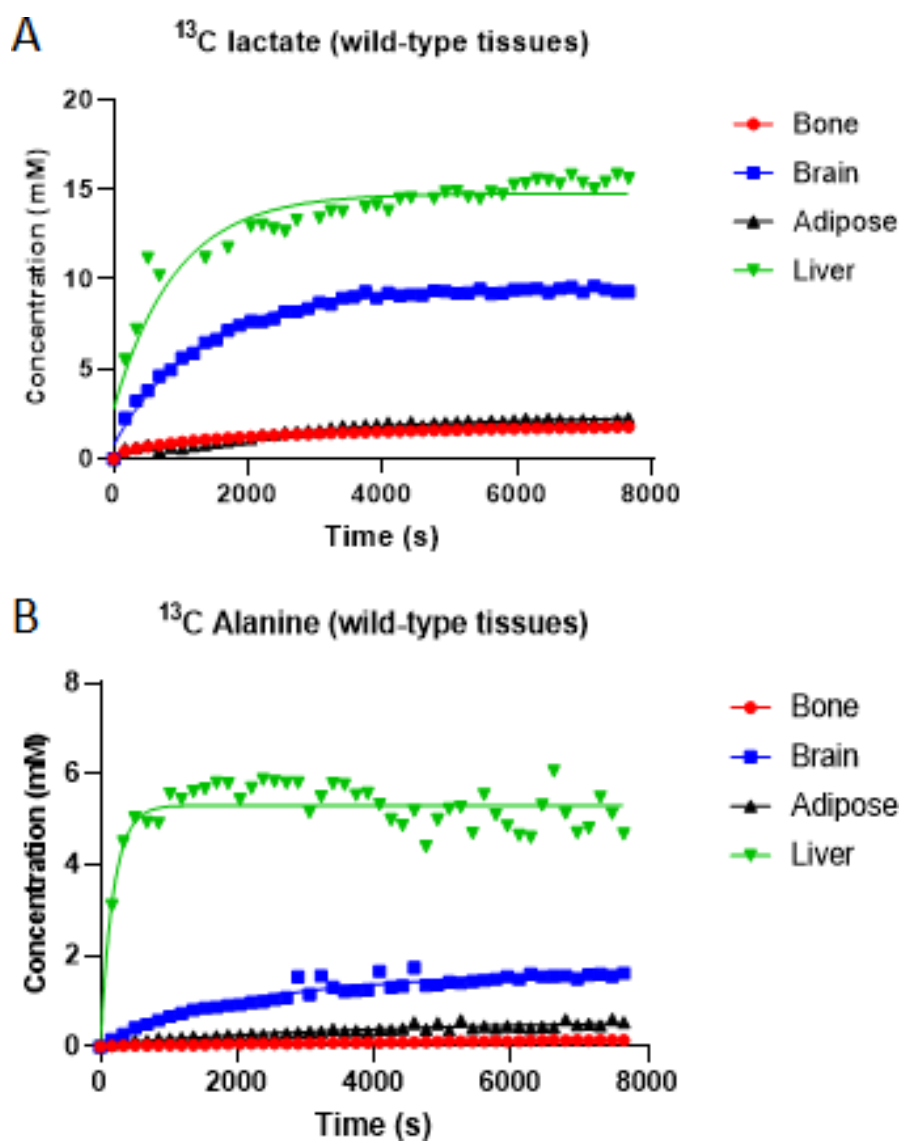
pPDH expression, although it was not statistically significant (1.791±0.11 at day 5 vs 2.987±1.28 at day 13 for PDH; 0.546±0.37 at day 5 vs 1.424±0.93 at day 13 for pPDH). In the context of adipocytes, however, a significant decrease in LDH expression between days 5 and 13 could be seen (9.611±4.14 at day 5 vs 2.870±1.59 at day 13, p<0.05). This decrease seemed to correlate with the pattern observed in qPCR, where a decrease in LDH gene expression could be seen with time. Interestingly, collective genomics and proteomics data of LDH in mMSC-derived adipocytes seemed to contradict the high LDH activity seen in the assay experiment (Figure 8D). Outside of LDH, however no other enzymes seemed to drastically change during the differentiation process in mMSCs.

Quite noticeably, the abundance of GAPDH was considerably lower in adipocytes when compared to osteoblasts and control mMSCs (Figure 12A). The reduced protein yield is likely due to high lipid content in adipocytes. This factor has been known to complicate protein extraction procedures (An and Scherer, 2020).

3.7 ¹³C label incorporation into alanine and lactate occurs much faster in tissue samples

As a follow up to our experiments in mMSCs, we decided to investigate whether the same methodology could be applied to tissue samples. Identical ¹H NMR spectroscopy experiments to those in mMSCs were thus

performed on mouse tissue (liver, adipose, bone, and brain) homogenates (Figure 13). The timescale of ^1H NMR experiments (~ 2 hours) was selected to allow the formation of kinetic steady states in the ^{13}C label exchange reactions. In direct comparison to the data from mMSC samples, the changes in $[1-^{13}\text{C}]$ lactate and $[1-^{13}\text{C}]$ alanine concentration displayed little to no linearity. Moreover, a non-linear regression analysis of the data showed that most curves demonstrate almost perfect curve-fitting ($R^2 > 0.9$). Nevertheless, $[1-^{13}\text{C}]$ alanine data proved to lean more towards linearity in comparison to $[1-^{13}\text{C}]$ lactate, especially in adipose tissue. This means that the exchange of pyruvate to alanine is much slower than pyruvate to lactate.



C

Tissue	¹³ C label transfer rate from [1- ¹³ C] pyruvate to alanine, μM/sec	¹³ C label transfer rate from [1- ¹³ C]pyruvate to lactate, μM/sec	[1- ¹³ C]lactate/[1- ¹³ C]alanine ratio
Brain	0.280 ± 0.093	0.697 ± 0.179	2.49 ± 1.92
Liver	0.457 ± 0.039	0.345 ± 0.197	0.75 ± 5.05
Adipose	0.147 ± 0.043	1.811 ± 0.107	12.32 ± 2.48
Bone	0.179 ± 0.031	0.720 ± 0.154	4.01 ± 4.96

Figure 13: ¹H NMR spectroscopic measurements of ¹³C label incorporation in tissue samples. Representative images A and B show plotted representative kinetics graphs from bone, brain, adipose, and liver tissues. Red – bone, blue – brain, black – adipose, green – liver. One phase association curves are shown in corresponding colours. Image A shows ¹³C-label incorporation into lactate, while image B shows the ¹³C-label incorporation into alanine. Table C shows the calculated label transfer rates and ratios between specific metabolites in tissues. Values are shown as mean ± SEM. N=3 for all groups.

Overall, we observed a larger metabolite concentration in tissue samples compared to mMSC samples, which is likely due to a difference in both enzyme and cell quantity between cell and tissue samples. This difference in metabolite concentration was also apparent when comparing different tissues. Liver tissue demonstrated the highest levels of both [1-¹³C]alanine (6.6±3.6mM) and [1-¹³C]lactate (11.1±3.8mM). This was expected, as the liver is a key organ in the Cori and alanine cycles (Waterhouse and Keilson, 1969; Felig, 1973). As such, high levels of LDH and ALT abundance and activity are expected to be seen in hepatocytes. The brain, on the other hand, was close to the liver in terms of [1-¹³C]lactate (5.9±1.8mM), but showed drastically lower [1-¹³C]alanine levels (1.5±0.6mM). Astrocytes, the most common cells found in the mouse central nervous system, have been known to produce lactate as part of a

coupled metabolic system between astrocytes and neurons (Keller, Erö and Markram, 2018; Dienel, 2019; Ioannou *et al.*, 2019). Therefore, substantial levels of LDH would be expected in brain tissue. Regarding [1-¹³C]alanine levels observed in the brain, studies have shown that alanine is not utilized as an energy source or neurotransmission in the brain. However, alanine plays an important role in ammonia transfer during glutamate/glutamine cycling in brain tissue (Bröer *et al.*, 2007). Therefore, it is likely that ALT generates levels of alanine in the brain only sufficient for the maintenance of local metabolic processes.

Meanwhile, adipose and bone tissues displayed very similar levels of [1-¹³C]lactate (1.6±0.5mM in adipose vs 1.6±0.3mM in the bone). However, [1-¹³C]alanine levels between bone and adipose were not as similar (0.869±0.34mM in the adipose vs 0.1±0.02mM in the bone), with the bone tissue showing surprisingly low levels. Lactate production is an integral aspect of both adipocyte and osteoblast metabolic profiles. Adipocytes prioritize lactate biosynthesis to dispose of excess glucose, while the bone tissue microenvironment is highly hypoxic, making cells rely on glycolytic bioenergetics (Esen and Long, 2014; Krycer *et al.*, 2020). Thus, the observed levels of generated [1-¹³C]lactate coincide with the functionality of the host cells. However, the same cannot be said about the observed [1-¹³C]alanine levels. With particular attention to the bone tissue, a much more substantial increase in [1-¹³C]alanine levels was expected due to the high abundance to highly biosynthetic osteoblasts. A possible explanation for the difference between expectation and the result is that during tissue processing for ¹H NMR experiments, whole bone was homogenized. The homogenate thus likely contained traces of non-osteoblast cells, such as bone marrow cells, skewing the metabolic data.

3.8 Wild-type tissue metabolomics display no clear grouping of tissues

As for mMSCs, multivariate statistical analysis was employed to screen baseline (pre-pyruvate addition) spectra for any biomarkers metabolites linked to pyruvate. Spectra from all wild-type tissues were binned, normalized to total spectra sum, and analyzed. outside of the PCA analysis showed no significant differences between most tissues. However, brain tissues displayed some difference to other tissues, being exclusively

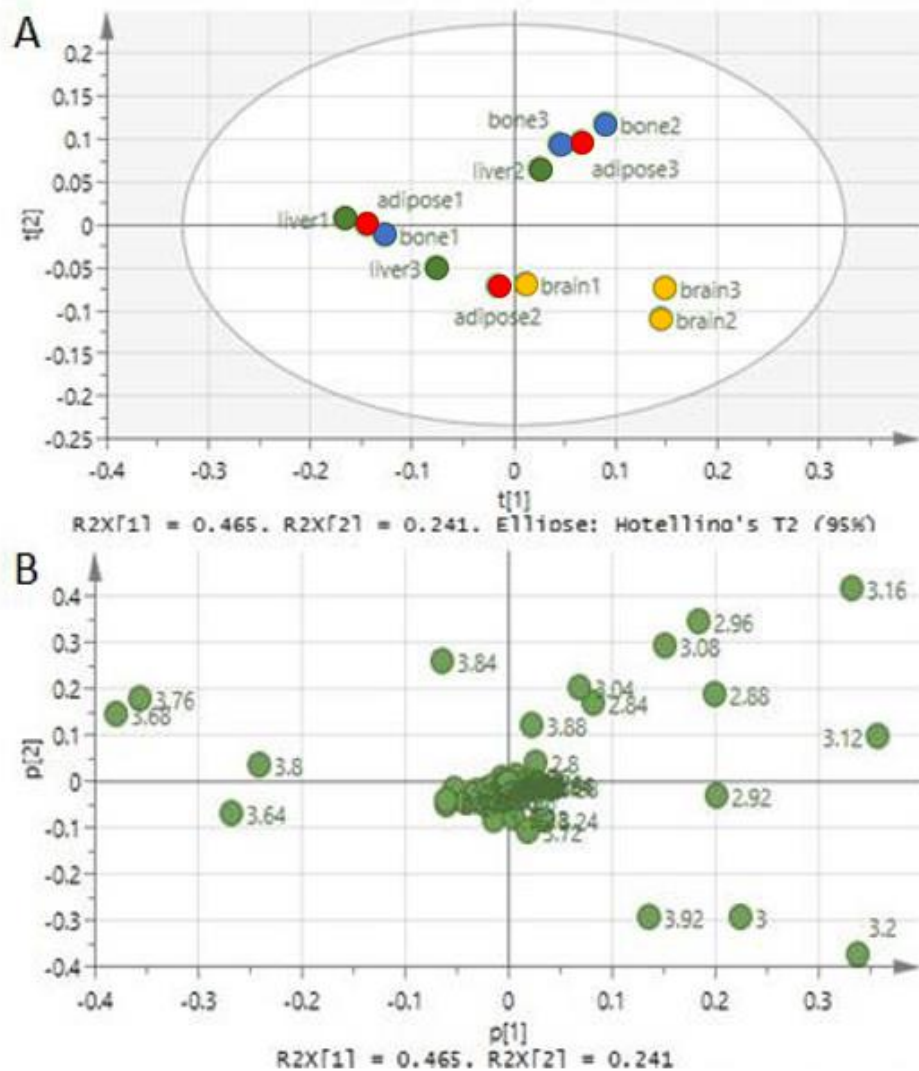


Figure 14: Principal component analysis of wild-type mouse tissues. Data were obtained from the pre-pyruvate addition spectra and normalized to total sum of spectral bins. A – the scores plot, showing how the observations are distributed on the two principal component axes. Green – liver, blue – bone, red – adipose, yellow – brain tissue. B – the loadings plot, showing how the variables are distributed on the two principal component axes. At the bottom of both pictures, the cumulative R2X values provided by each principal component can be seen. t[1] – principal component 1; t[2] – principal component 2. N=3 for each tissue.

allocated to one quarter on the score plot (Figure 14A). The remaining tissues, however, could be found randomly distributed across the plot. Confidence values generated by two principal components were 0.706 for R2X and 0.432 Q2. These numbers suggested that the presented model explains the present data sufficiently well, but may potentially lack predictive power to determine how incoming data would be treated.

The loadings provided some insight on which bins, and therefore metabolites present in those bins, affect the distribution (Figure 14B). Seemingly, brain tissue separation was highly influenced by bins 3, 3.2, and 3.92. Heavy pull to the left hand side was seen from bins 3.68 and 3.76. Some pull up was seen from bins 3.16, 2.96, and 3.08. Lastly, pull to the right was mostly affected by bin 3.12

3.9 Differences in gene expression responsible for pyruvate metabolism in mouse tissues

Absolute quantification of LDH, PDH and ALT gene expression was performed due to differences in GAPDH expression (reference gene) levels between different tissues. A heatmap was generated to show the gene expression distribution in our tested tissues (Figure 15). As the data was generated using absolute quantification, instead of fold expression difference the data is expressed as replicon concentrations ng/ μ L.

Expression of ALT gene in the liver tissue was significantly higher compared to both adipose and bone tissues ($107.53 \pm 10.33 \text{ ng}/\mu\text{L}$ in the liver vs $69.23 \pm 5.69 \text{ ng}/\mu\text{L}$ in the adipose ($p=0.0362$), and $67.29 \pm 0.34 \text{ ng}/\mu\text{L}$ in the bone; $p=0.0293$), and differed little from brain tissue ($107.53 \pm 10.33 \text{ ng}/\mu\text{L}$ in the liver vs $82.31 \pm 2.83 \text{ ng}/\mu\text{L}$, $p>0.05$). In terms of LDH gene expression, adipose tissue data showed substantial differences to liver and bone tissues ($105.52 \pm 5.04 \text{ ng}/\mu\text{L}$ in adipose vs $73.66 \pm 4.79 \text{ ng}/\mu\text{L}$ in the liver ($p=0.0087$) and $81.88 \pm 1.66 \text{ ng}/\mu\text{L}$ ($p=0.0341$)). LDH gene expression in the brain was noticeably smaller than in the adipose ($92.52 \pm 3.45 \text{ ng}/\mu\text{L}$ in the brain vs $105.52 \pm 5.04 \text{ ng}/\mu\text{L}$ in adipose), but the significance threshold was not crossed ($p>0.05$). PDH copy numbers seemed to remain stable across all tissues ($106.32 \pm 11.95 \text{ ng}/\mu\text{L}$ in the brain, $102.15 \pm 5.52 \text{ ng}/\mu\text{L}$ in the liver, $103.66 \pm 8.28 \text{ ng}/\mu\text{L}$ in the adipose, $106.52 \pm 5.97 \text{ ng}/\mu\text{L}$ in the bone, $p>0.05$).

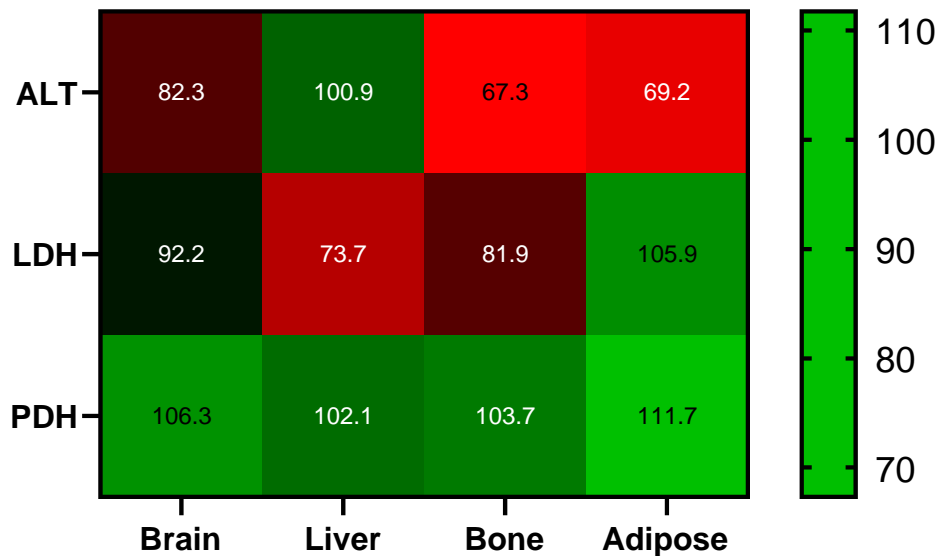


Figure 15: Absolute quantification of gene expression in wild-type mouse tissues. Each cell in the heatmaps shows the concentration of replicons of an individual gene of interest in four wild-type mouse tissues. Graphs show mean data ($n=3$). Data were generated using a standard curve for each gene in every tissue.

Expression of the ALT gene in the liver tissue was significantly higher compared to both adipose and bone tissues ($107.53 \pm 10.33 \text{ ng}/\mu\text{L}$ in the liver vs $69.23 \pm 5.69 \text{ ng}/\mu\text{L}$ in the adipose ($p=0.0362$), and $67.29 \pm 0.34 \text{ ng}/\mu\text{L}$ in the bone ($p=0.0293$)) and differed little from brain tissue ($107.53 \pm 10.33 \text{ ng}/\mu\text{L}$ in the liver vs $82.31 \pm 2.83 \text{ ng}/\mu\text{L}$, $p>0.05$). In terms of LDH, adipose tissue data showed substantial differences to liver and bone tissues ($105.52 \pm 5.04 \text{ ng}/\mu\text{L}$ in adipose vs $73.66 \pm 4.79 \text{ ng}/\mu\text{L}$ in the liver ($p=0.0087$) and $81.88 \pm 1.66 \text{ ng}/\mu\text{L}$ ($p=0.0341$)). LDH gene expression in the brain was noticeably lower than in the adipose ($92.52 \pm 3.45 \text{ ng}/\mu\text{L}$ in the brain vs $105.52 \pm 5.04 \text{ ng}/\mu\text{L}$ in adipose), but the significance threshold was not crossed ($p>0.05$). PDH copy numbers seemed to remain stable across all tissues ($106.32 \pm 11.95 \text{ ng}/\mu\text{L}$ in the brain, $102.15 \pm 5.52 \text{ ng}/\mu\text{L}$ in the liver, $103.66 \pm 8.28 \text{ ng}/\mu\text{L}$ in the adipose, $106.52 \pm 5.97 \text{ ng}/\mu\text{L}$ in the bone, $p>0.05$).

3.10 Differences in enzyme expression responsible for pyruvate metabolism in mouse tissues

To complete our elucidation of pyruvate metabolism in mouse wild-type tissues, we performed Western blotting on tissue homogenates. Images of the blots can be seen in Figure 16A. As previously described, we quantified the signals and plotted them on a bar chart (Figure 16B). Values were expressed at relative intensity (arbitrary value).

Following quantification and normalization of data, we could adequately compare enzyme levels between the tissues. In contradiction to LDH gene expression data in wild-type tissues, the most LDH protein was present in the bone tissue (3.82 in the bone vs 2.56 in the liver; 2.82 in the adipose; 1 in the brain). ALT was the highest in the liver (73.99 in the liver vs 29.74 in the bone; 7.43 in the adipose, 1 in the brain). Again, an inconsistency was present when comparing gene expression with protein expression for ALT. Protein expression of ALT in the brain was the lowest of all tissues, yet the gene expression was higher than both bone

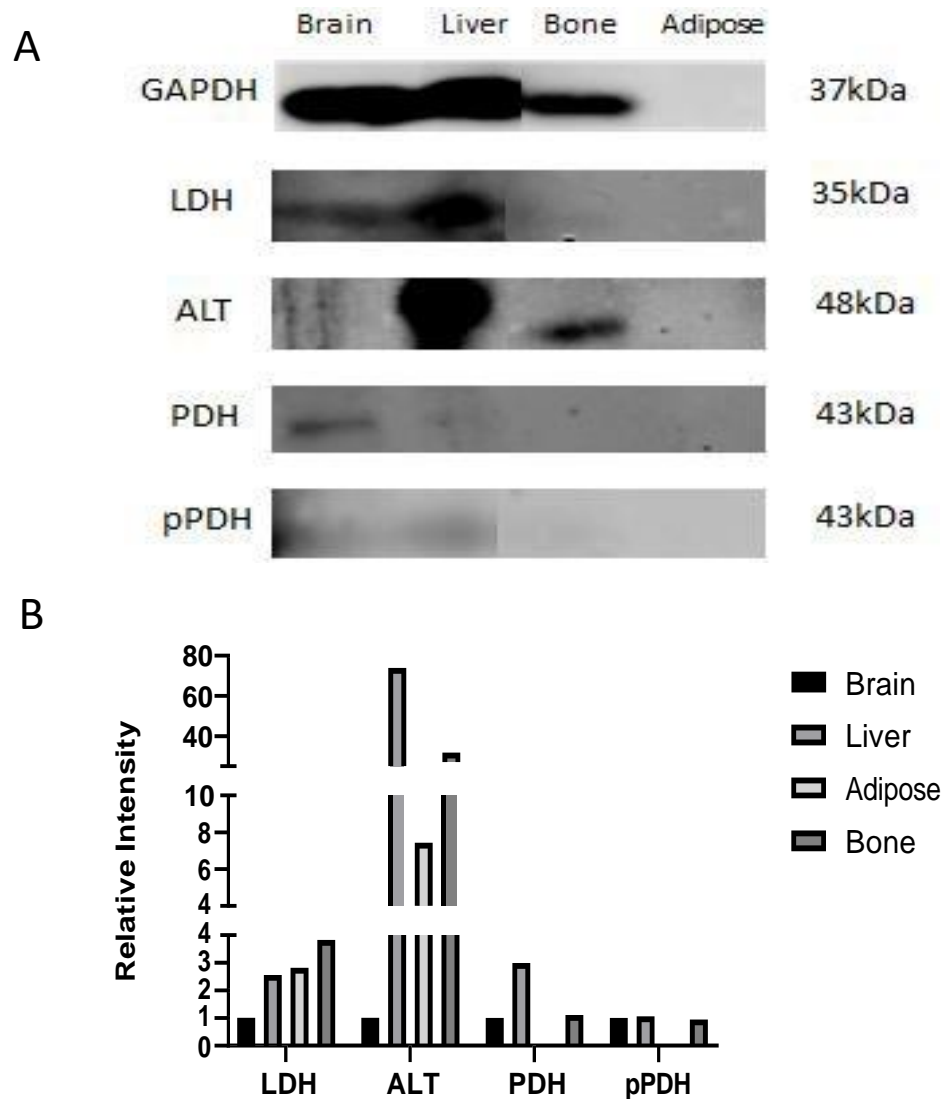


Figure 16: Western blot results of wild-type mouse tissues. A – images of blots. Well identities are indicated above the blots, while the enzyme names of the corresponding images are shown on the left. Enzyme sizes in respective bands are shown on the right. 50 μ g of protein was loaded in every well. This data set was gathered from one experimental repeat. GAPDH signal was measured at 800nm, while all other enzymes were imaged at 700nm. Data was normalized to GAPDH. B – quantified data from blots. Relative intensity of antibody fluorescence was measured via densitometric analysis (expressed in arbitrary units). Values shown are means (n=1). Brain tissues values were used as calibrators to allow easier comparison. Insufficient repeats prevented statistical testing.

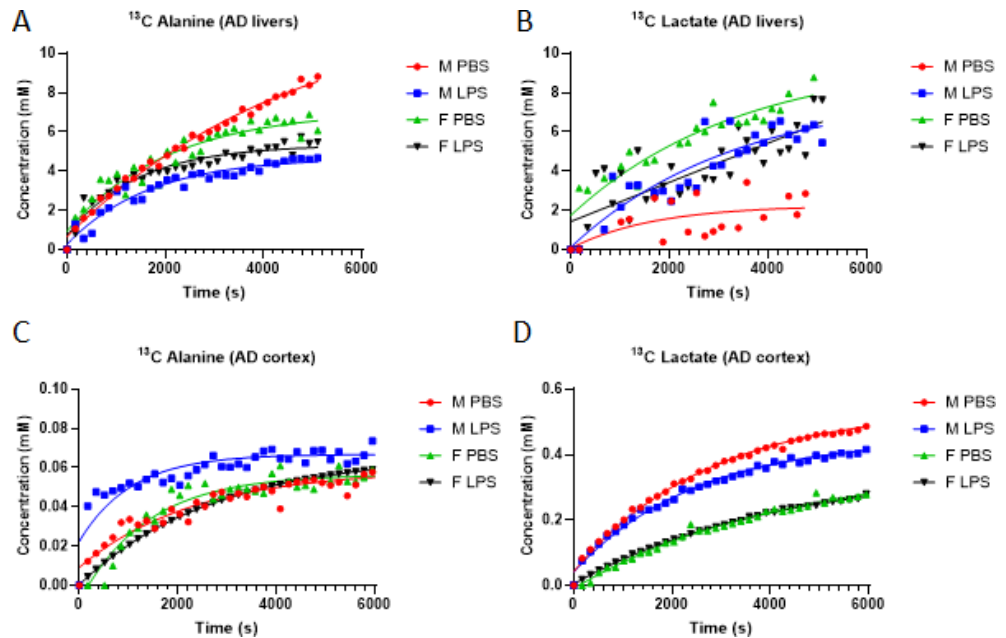
and adipose. While PDH gene expression was very similar across all tissues, the protein was barely detectable, being the most abundant in the liver (2.99 in the liver vs 1.11 in the bone; 1 in the brain, undetected in adipose). pPDH levels were also highest in the liver, although very similar to both bone and brain (1.06 in the liver vs 0.94 in the bone; 1 in the bone, undetected in adipose). The poor signals in adipose tissue could be due to high lipid content.

3.11 ^1H NMR data collected from Alzheimer's Disease mouse tissue cannot differentiate between sex or states of inflammation

Having successfully collected data from wild-type tissues, we carried out the same approach tissue gathered from APP/PS1 (Alzheimer's model) mice. Wild-type and AD model tissues could not be compared directly due to difference in genotype. We aimed to assess pyruvate metabolism as a potential biomarker in Alzheimer's disease (AD), particularly in relation to sexual dimorphisms and the effects of inflammation. Four groups of APP/PS1 mouse tissue were used. These four groups represented two sexes (male(M) and female(F)) and two different treatments that the mice were subjected to (PBS treatment (non-inflamed) and LPS treatment (inflamed)). Two types of tissue were analyzed: liver and cerebral cortex. Although the disease process of AD primarily affects brain tissue, some evidence suggests that the liver is involved with $\text{A}\beta$ clearance, and is also among the organs affected by amyloid pathology progression (Sutcliffe *et al.*, 2011; Zheng *et al.*, 2019). Thus, in the context of AD, liver tissue was examined alongside brain tissue.

^{13}C label transfer from pyruvate to lactate and alanine showed similarity in terms of kinetics compared to wild-type tissues. The kinetics data were fitted using one phase association equation and not a linear fit as for mMSC data (Figure 17). A two-way ANOVA followed by a post hoc Tukey's

multiple comparison was used to compare the ^{13}C label transfer rates in all four experimental groups within AD mouse tissues. In the liver, statistical analysis showed no significant difference in $[1-^{13}\text{C}]\text{lactate}$ generation rate based on sex or inflammation ($0.31\pm 0.28\mu\text{M}/\text{sec}$ in M PBS; $0.25\pm 0.084\mu\text{M}/\text{sec}$ in M LPS; $0.14\pm 0.004\mu\text{M}/\text{sec}$ in F PBS; $0.13\pm 0.012\mu\text{M}/\text{sec}$). For $[1-^{13}\text{C}]\text{alanine}$, however, there was a significant change in the reaction rate associated with inflammation, ($0.26\pm 0.05\mu\text{M}/\text{sec}$ in M PBS, $0.26\pm 0.007\mu\text{M}/\text{sec}$ in F PBS vs $0.13\pm 0.02\mu\text{M}/\text{sec}$ in M LPS $0.22\pm 0.018\mu\text{M}/\text{sec}$ in F LPS, $p=0.0111$). Data are summarized in a table (Figure 17E). Additionally, no substantial difference was found between $[1-^{13}\text{C}]\text{lactate}/[1-^{13}\text{C}]\text{alanine}$ ratios in all four liver groups ($p>0.05$). Overall, our results suggest that both ^{13}C -labelled lactate and alanine are produced at very similar rates in these livers, and that neither sex nor inflammation impact these numbers.



E

	¹³ C label transfer rate from [1- ¹³ C]pyruvate] to alanine, μM/sec	¹³ C label transfer rate from [1- ¹³ C]pyruvate to lactate, μM/sec	[1- ¹³ C]lactate/[1- ¹³ C]alanine ratio
M PBS	0.26 ± 0.05	0.31 ± 0.28	1.21 ± 5.61
M LPS	0.13 ± 0.02 *	0.26 ± 0.08	1.97 ± 4.29
F PBS	0.26 ± 0.007	0.15 ± 0.004	0.55 ± 0.58
F LPS	0.22 ± 0.018 *	0.13 ± 0.012	0.56 ± 0.69

F

	¹³ C label transfer rate from [1- ¹³ C]pyruvate] to alanine, μM/sec	¹³ C label transfer rate from [1- ¹³ C]pyruvate to lactate, μM/sec	[1- ¹³ C]lactate/[1- ¹³ C]alanine ratio
M PBS	0.45 ± 0.02	0.28 ± 0.07	0.62 ± 3.16
M LPS	0.61 ± 0.33	0.32 ± 0.08	0.52 ± 0.24
F PBS	0.75 ± 0.14	0.17 ± 0.03	0.23 ± 0.19
F LPS	0.39 ± 0.018	0.31 ± 0.07	0.79 ± 3.7

Figure 17: Production of ¹³C-labelled lactate and alanine in APP/PS1 mouse tissue. Images A and B show representative graphs of ¹³C-label incorporation into alanine and lactate in APP/PS1 livers, respectively. Images C and D represent ¹³C-label incorporation into alanine and lactate in APP/PS1 cortex tissue. Sex and treatment groups are color coded: red – M PBS, blue – M LPS, green – F PBS, black – F LPS. N=3 in all groups. Tables E (liver) and F (cortex) show reaction rates in each group. * - significant change versus the other treatment group. Values are shown as means (n=3) ± SEM.

3.12 Metabolomics of Alzheimer's tissues reveals differences between different sexes and treatments.

While kinetics data of pyruvate-associated enzymes indicated little capacity for tissue group separation, multivariate analysis of metabolic phenotypes revealed that differences between different groups indeed exist. Score plots from livers (Figure 18A) presented a neat organization of all observations into 3 groups: M PBS, F PBS, and the LPS treated group. Overlap was also present, where some LPS treated tissues were found next to the F PBS tissues, regardless of sex. Based on the loadings plot (Figure 18B), we identified that this model was most affected by metabolites in bins 3, 3.92, 3.2, 3.88, 2.96, and 3.12, 3.16.

Looking at the cortex data (Figure 19), three observation clusters are visible, same as for liver tissues. However, no clear pattern can be identified, based on either sex or treatment. Despite this, the data seemed to be well defined based on the quality metrics (R2X=0.945, Q2=0.77). Nevertheless, data from variables suggest mostly the same culprit bins as in the liver – 3, 3.92, 3.2, 2.96, 3.16. This implies that while the signals from these metabolites varied in the cortex samples, it had no correlation with the treatment group, unlike the liver. However, more statistical power would be required to confirm these findings.

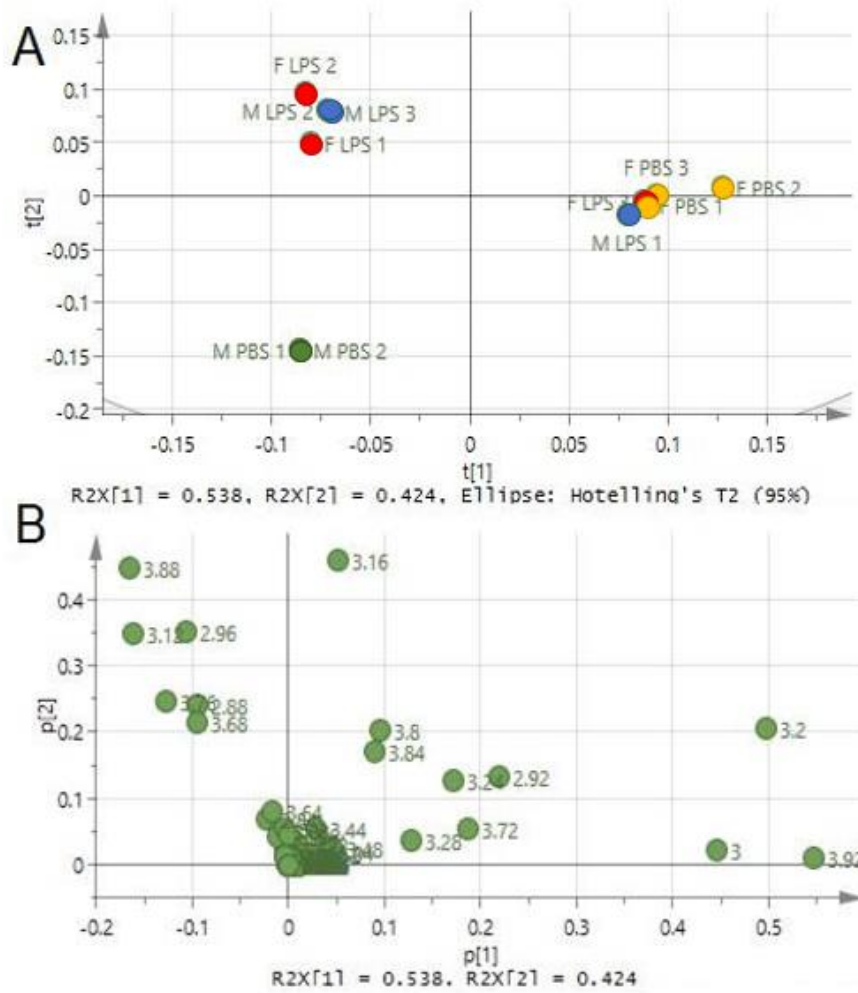


Figure 18: Principal component analysis of APP/PS1 livers. Data was gathered from pre-pyruvate addition spectra and normalized to total sum of bins. A – the scores plot, showing how the observations are distributed on the two principal component axes. Green – M PBS, blue – M LPS, yellow – F PBS, red – F LPS. B – the loadings plot, showing how the variables are distributed on the two principal component axes. At the bottom of both pictures, the cumulative R2X values provided by each principal component can be seen. t[1] – principal component 1; t[2] – principal component 2. N=3 for all

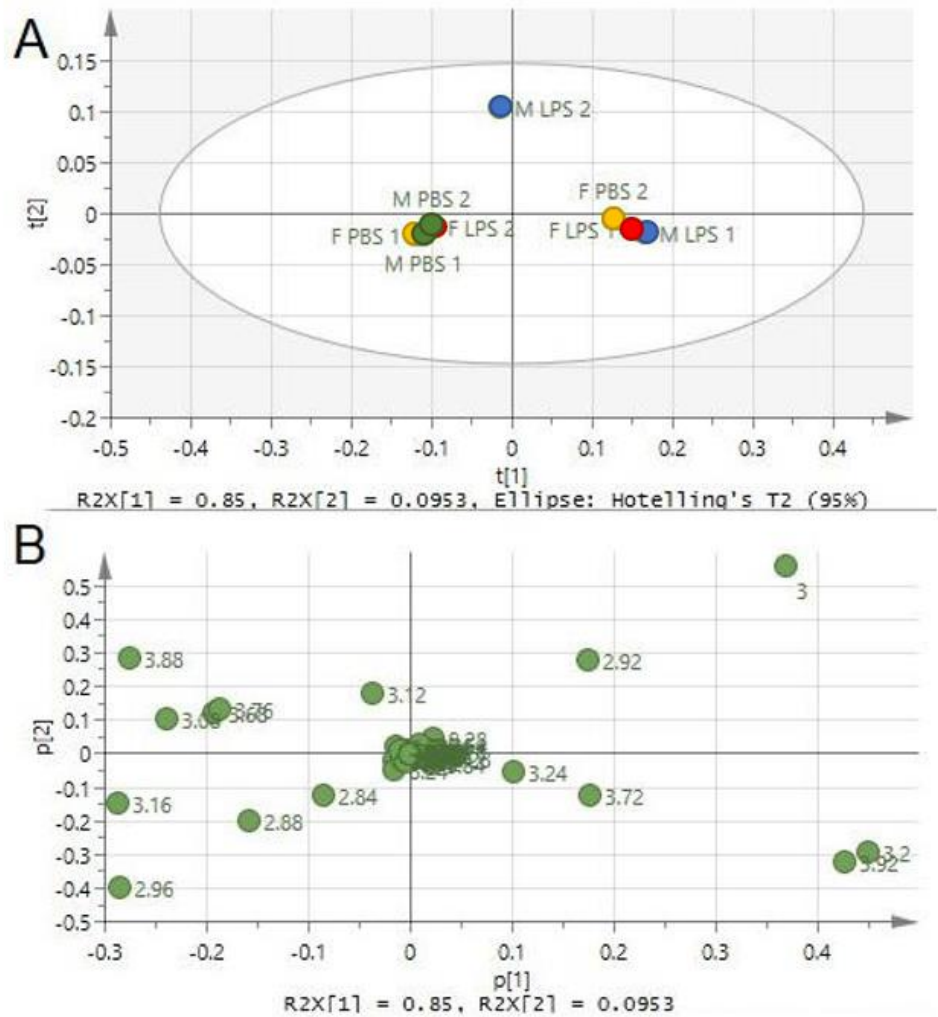


Figure 19: Principal component analysis of APP/PS1 cortex. Data were obtained from pre-pyruvate addition spectra and normalized to total spectra sum. A – the scores plot, showing how the observations are distributed on the two principal component axes. Green – M PBS, blue – M LPS, yellow – F PBS, red – F LPS. B – the loadings plot, showing how the variables are distributed on the two principal component axes. At the bottom of both pictures, the cumulative R2X values provided by each principal component can be seen. t[1] – principal component 1; t[2] – principal component 2. N=2 for all groups.

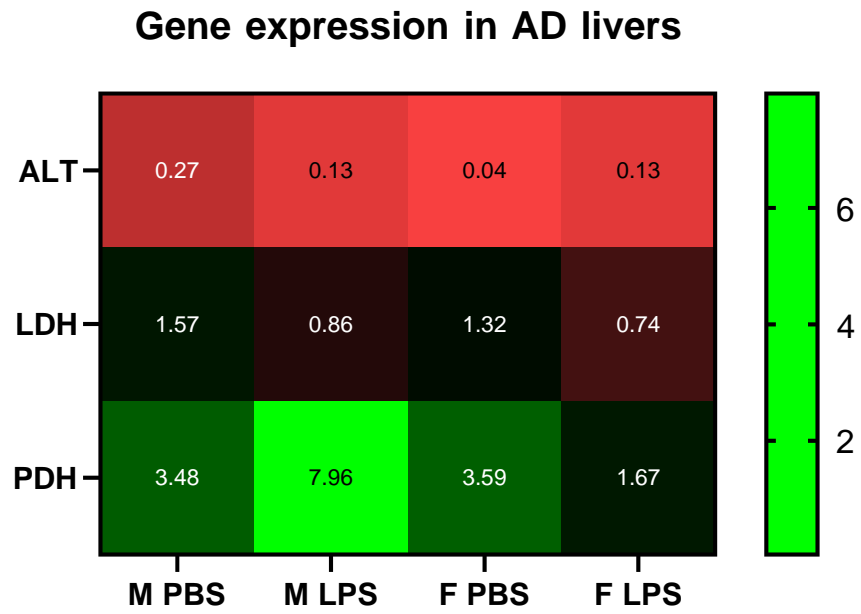
3.13 Gene expression of pyruvate-associated enzymes display changes based on sex and treatment

Having acquired data of metabolite kinetics in AD tissues, we also investigated whether sex or treatment affect gene expression of ALT, LDH, and PDH genes. Data were normalized to reference gene (GAPDH). As a follow up, we used wild-type expression levels as calibrator samples, allow easier comparison in terms or relative gene expression. All data were presented as heatmaps (Figure 16).

In AD mouse livers (Figure 16A), a substantial downregulation in ALT gene expression was apparent when comparing our four experimental groups with the wild-type. This change remained consistent across all sex and treatment groups (0.27 ± 0.05 in M PBS, 0.13 ± 0.01 in M LPS, 0.04 ± 0.01 in F PBS, 0.13 ± 0.01 in F LPS; $p < 0.0001$). No substantial difference in ALT gene expression was found between all four groups of AD mouse livers. A more complex picture was seen in the context of LDH. In response to PBS treatment, LDH seemed to be expressed at a higher level compared to both wild-type and LPS-treated livers (1.57 ± 0.04 in M PBS, $p < 0.01$; 1.32 ± 0.005 in F PBS, $p < 0.01$). LPS-treated livers seemed to express LDH at a level comparable to the wild-type, with the F LPS group indicating some level of LDH gene downregulation (0.74 ± 0.007 , $p = 0.0074$). Finally, PDH data showed substantial variance, to the point where the error prevented identification of any relevant changes, be it sex or treatment related (3.48 ± 2.87 in M PBS, 7.96 ± 2.12 in M LPS, 3.59 ± 1.00 in F PBS, 1.67 ± 0.64 in F LPS; $p > 0.05$). Although, current data indicates a potential increase in PDH expression in the AD phenotype.

Unlike liver samples, AD cortex samples (Figure 16B) showed no clear disposition to changes in the gene expression of ALT. A trend is discernable, such as an increase in ALT expression in LPS-treated tissue

A



B

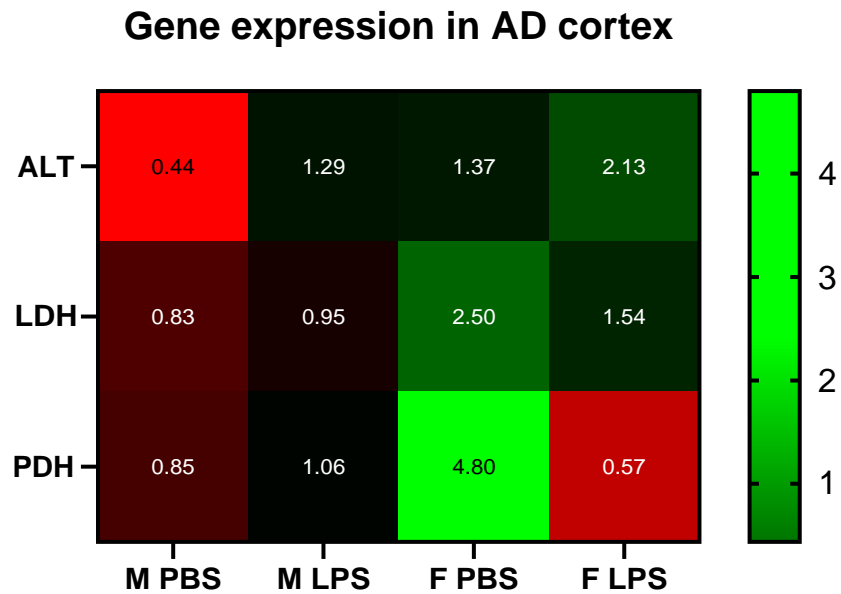


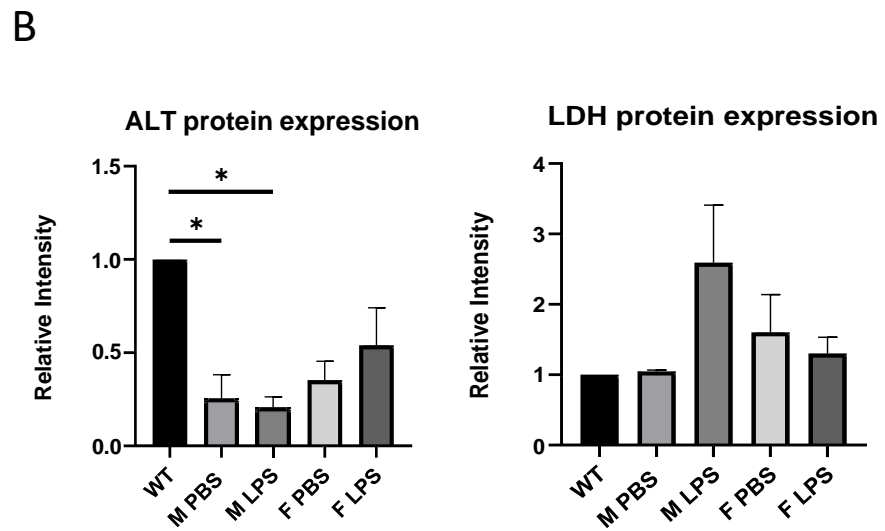
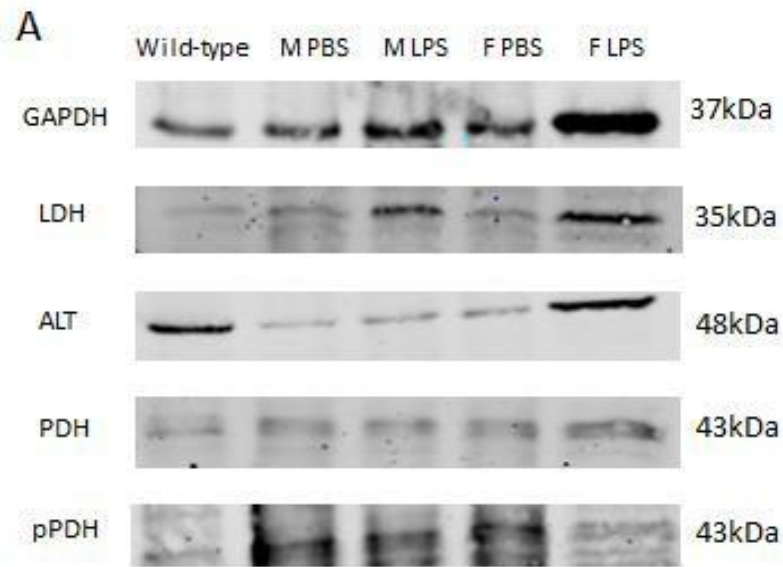
Figure 20: Relative gene expression levels of ALT, LDH, and PDH in Alzheimer's model mouse. All data is adjusted to GAPDH expression and normalized to the wild type to allow easy comparison. Values in cells show fold expression level vs wild-type. Graphs show mean (n=3).

(1.29 ± 0.68 in M LPS vs 0.44 ± 0.08 in M PBS; 2.13 ± 0.11 in F LPS vs 1.37 ± 0.38 in F PBS; $p > 0.05$), but poor data robustness prevented identification of any significant effects. Conversely, data showed a clear and substantial increase in LDH presence in the F PBS group (2.50 ± 0.24 in F PBS vs 0.83 ± 0.03 in M PBS, 0.95 ± 0.06 in M LPS, 1.54 ± 0.69 in F LPS; $p > 0.01$), while all other groups maintained very similar levels amongst themselves. PDH gene expression also showed upregulation in the F PBS treated group (4.80 ± 0.27 in F PBS vs 0.85 ± 0.52 in M PBS, 1.06 ± 0.03 in M LPS, 0.57 ± 0.24 in F LPS; $p < 0.01$)

3.14 Western blot analysis reveals differences in protein levels associated with sex and inflammation

Lastly, we measured enzyme levels in all 4 experimental groups with the aim to identify changes in protein expression associated with AD. All protein expression levels were normalized to the GAPDH loading control and calibrated using a wild-type sample. In AD mouse livers, western blot analysis revealed some sex-specific difference in ALT protein expression, but no changes in response to the treatment. In both male treatment groups, ALT suffered a significant reduction in quantity (0.25 ± 0.13 in M PBS and 0.21 ± 0.06 in M LPS, $p < 0.05$) compared to wild-type tissues. Although lacking significance, the data suggested a trend towards reduce expression of ALT enzyme in female AD mice (0.35 ± 0.10 in F PBS, 0.54 ± 0.20 in F LPS). This finding seemed to agree with qPCR data, where ALT production on a genomic level was significantly reduced in all groups compared to wild-

type tissues. For LDH, PDH, and pPDH, however, there was no significant differences between sex and/or treatment groups as shown by a two-way ANOVA analysis and post hoc Tukey's comparison test ($p > 0.05$). Moreover, any other significant qPCR data found in these same liver groups failed to match protein data.



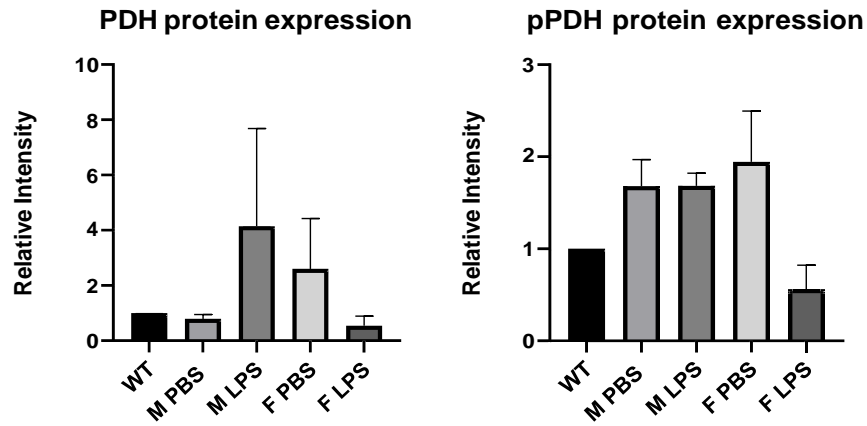


Figure 21: Analysis of Western blots in AD phenotype livers. A – images of blots made in livers. Well identities are indicated above the blots, while the enzyme names of the corresponding images are shown on the left. Enzyme sizes in respective bands are shown on the right. B – quantified blots. Relative intensity of antibody fluorescence was measured via densitometric analysis (expressed in arbitrary units). This set of images was gathered from one experimental repeat. GAPDH signal was measured at 800nm, while all other enzymes were imaged at 700nm. Graphs show mean ($n=3$) \pm SEM. All data was normalized to the wild-type to allow easy comparison. * $p<0.05$. All unspecified relationships were not significant.

A similar pattern was observed in cortex samples of APP/PS1 mice (Figure 22). ALT protein levels seemed to be reduced in all groups compared to the wild type (0.23 ± 0.14 in M PBS, 0.45 ± 0.37 in M LPS, 0.22 ± 0.019 in F PBS, 0.36 ± 0.26 in F LPS, $p>0.05$), although variance of this data was higher, LDH seemed to be present at levels very similar to those of the wild-type, completely unrepresentative of the qPCR data. PDH seemed to be present in much larger quantities, especially in males (3.85 ± 1.12 in M PBS and 5.05 ± 0.5 in M LPS versus 1.58 ± 0.7 in F PBS and 2.8 ± 0.84 in F LPS, $p>0.05$). pPDH was also quite abundant (4.51 ± 0.95 in M PBS, 1.55 ± 0.10 in M LPS, 2.47 ± 0.35 in F PBS, 1.92 ± 1.28), indicating strong inhibition of PDH in AD cortex. However, more statistical power is necessary to elucidate this relationship.

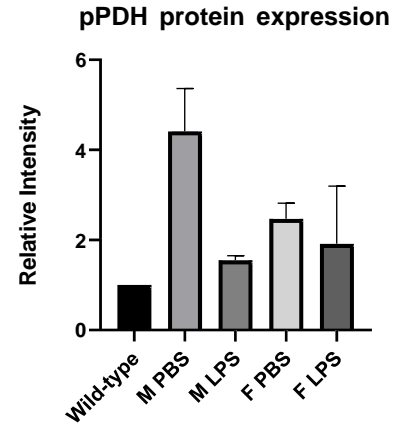
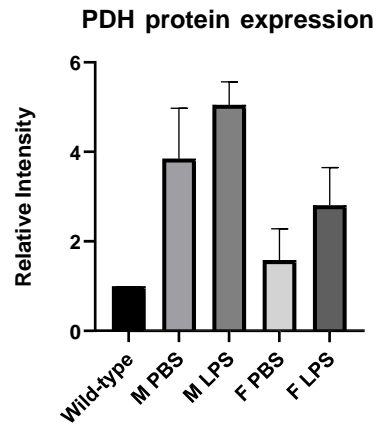
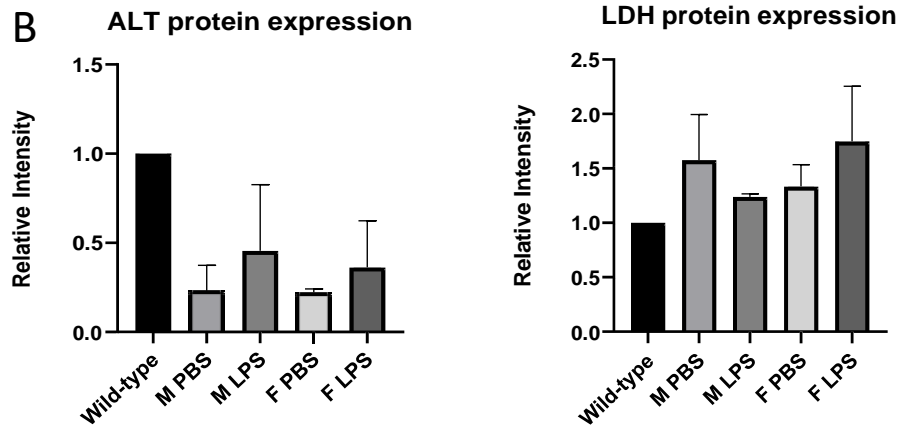
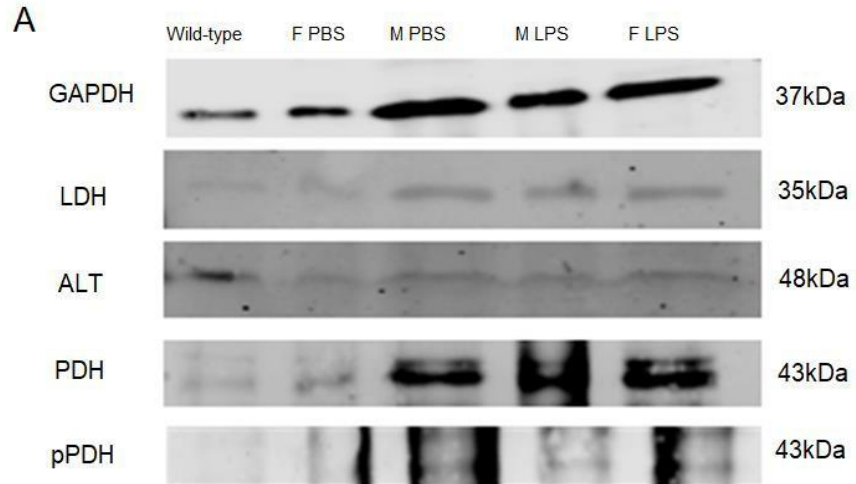


Figure 22: Analysis of Western blots in Alzheimer's phenotype cortex. A – images of blots made in cortex. Well identities are indicated above the blots, while the enzyme names of the corresponding images are shown on the left. Enzyme sizes in respective bands are shown on the right. B – quantified blots. Relative intensity of antibody fluorescence was measured via densitometric analysis (expressed in arbitrary units). This set of images was gathered from one experimental repeat. GAPDH signal was measured at 800nm, while all other enzymes were imaged at 700nm. Graphs show mean (n=3) ± SEM. All data was normalized to the wild-type to allow easy comparison. *p<0.05. All unspecified relationships were not significant.

Chapter 4: Discussion

To determine whether pyruvate conversion to lactate and alanine could be used as potential biomarkers of tissue phenotypes, cell differentiation, and disease, we investigated metabolic changes associated with pyruvate metabolism using ^1H NMR spectroscopy. We showed that the conversions of ^{13}C pyruvate to lactate and alanine were indicative of LDH, and ALT enzymes activities in real time and could be used to determine catabolic and anabolic changes in cells and tissues. Additionally, we investigated potential correlation between metabolic fluxes measured by ^1H NMR and genomic and proteomics analysis of LDH, ALT and also PDH for mitochondrial metabolism. This approach aimed to ascertain any impact or connection between upstream genomic and proteomic factors and the observed downstream metabolic phenotypes. With varying degrees of success, we performed the aforementioned analysis using a mouse model of mesenchymal differentiation, Alzheimer's Disease, and wild-type mouse tissues, and findings for each model were rather distinct and will be discussed sequentially below.

4.1 mMSCs demonstrate lineage plasticity

During mMSC differentiation, we found some overlap between both osteogenic and adipogenic lineages in terms of differentiation pathways. Following the chemical induction of mMSC differentiation through addition of media supplements, formation of lipid vacuoles was observed in the osteogenically-induced group. An immediate point of interest were the media supplements associated with the differentiation procedure. One particular component, dexamethasone, was identified to be present in media aimed to invoke both adipogenic and osteogenic differentiation. At the molecular level, dexamethasone has been shown to interact with pro-osteogenic transcription factors RUNX2 and Osterix, as well as bone matrix

genes (Rickard *et al.*, 1994; Hamidouche *et al.*, 2008). Conversely, adipogenesis is upregulated through the interaction of dexamethasone with C/EBP δ via glucocorticoid receptor binding (Gregoire, Smas and Sul, 1998). Furthermore, research suggests that mature somatic cells derived from human bones can undergo lineage reprogramming and assume an adipocyte phenotype upon exposure to a combination of dexamethasone and IBMX (Nuttall *et al.*, 1998). This suggests that a certain level of phenotypic plasticity exists between adipogenic and osteogenic lineages. In our study, lineage plasticity in mMSCs presents a limitation, as it results in adipocytes arising in osteogenically-induced mMSC populations, thus leading to a mixed population of cells that does not accurately represent metabolic, proteomic, and genomic features of pure osteoblast cultures.

4.3 Differences in enzyme activity levels reflect post-differentiation phenotypes

Enzymatic assays measured in differentiating mMSCs indicated drastic changes in the activity levels of ALT and LDH enzymes for both osteogenic and adipogenic lineages. In particular, ALT activity was the highest in osteoblasts while LDH was the most prominent in adipocytes at the end of the differentiation process. It can therefore be assumed that the activity levels of these enzymes are closely correlated to the function of their host cells.

Osteoblasts are highly biosynthetic cells involved in growth and maintenance of the skeleton, producing large quantities of extracellular matrix proteins (Long, 2012). Additionally, the synthesis of type I collagen, a major component of bone ECM, is closely linked to the expression of osteocalcin, a gene involved in osteoblast differentiation (MacDonell, Hamrick and Isales, 2016). Therefore, ALT could potentially participate in driving a feedforward mechanism that not only drives pyruvate towards amino acid synthesis, but also promotes osteoblast formation. Meanwhile,

proliferating preadipocytes stop growth, usually through contact inhibition, thus reducing their dependence on protein biosynthesis and ALT anabolic activity (Rosen *et al.*, 2017). The remaining use for ALT in adipocytes could therefore be to divert alanine to lipid biosynthesis by converting it to pyruvate and subsequently to acetyl-CoA, the core building block of lipids. Finally, it is difficult to pinpoint why ALT activity decreased in control mMSCs between days 10 and 15. One factor could be that overly confluent cell population at day 15 would inhibit proliferation by cell contact and therefore would reduce biosynthetic demand.

In contrast, LDH activity seemed to increase in adipocytes between days 10 and 15 of mesenchymal differentiation. Recent research has shown that lactate is a substantial output product of adipocytes and is produced independently of glucose metabolism (Krycer *et al.*, 2020). This could explain why LDH activity is elevated in adipocytes. Furthermore, LDH expression in adipocytes is epigenetically controlled through histone acetylation, where acetyl CoA acts as an acetyl group donor (Wellen *et al.*, 2009). As mentioned previously, acetyl-CoA is a core building block in lipid biosynthesis. These findings highlight a direct connection between cellular metabolism and epigenetics. The role of lactate produced by adipocytes remains elusive, but it is currently theorized that it potentially has a key role in mammalian glucose homeostasis, either as signal molecule or substrate (Landau and Wahren, 1988; Ahmed *et al.*, 2010). In the context of osteoblasts, LDH activity also seemed to increase between days 10 and 15 of mesenchymal differentiation, although the values remained within the error margins. Studies suggest that osteoblasts are highly glycolytic cells, similarly to cancer cells (Lunt and Vander Heiden, 2011; Esen and Long, 2014). Considering the high metabolic productivity of osteoblasts, they require a steady supply of ATP and carbon skeletons to maintain *de novo* protein synthesis (Lee *et al.*, 2017). Glycolysis

fulfills this demand by allowing a more rapid (although less efficient) generation of energy alongside provision of building materials.

4.4 Real-time observation of ^{13}C -label exchange offers a promising approach to mMSC phenotyping

^1H NMR spectroscopy was used in conjunction with ^{13}C -labelled pyruvate to measure pyruvate conversion to lactate and alanine, indicative of LDH and ALT activities *in vivo*. In this experiment, we established that ^{13}C lactate/ ^{13}C alanine signal ratios from ^{13}C pyruvate labelling in rapidly extracted cell-free homogenates of control MSCs and lineage-committed cells correlate with mesenchymal differentiation. Based on this evidence, we hypothesize that the fate of ^{13}C tracers could be used as early and sensitive biomarkers of mesenchymal differentiation using intact cells, and also *in vivo* in transplants. Although more work is required to clarify the consistency of $[1-^{13}\text{C}]\text{lactate}/[1-^{13}\text{C}]\text{alanine}$ ratio differences at other stages of differentiation, the relationship between these two metabolites currently shows great potential as a biomarker. Coupled with dynamic nuclear polarization (DNP or hyperpolarization) of ^{13}C -labelled tracers that enhances the sensitivity to detection of ^{13}C tracers $>10^4$ -fold (Ardenkjær-Larsen *et al.*, 2003) there is a great potential for NMR spectroscopy non-destructively observe and measure metabolic fluxes in real-time in stem cell-derived populations cultured in bioreactors. In addition, this method could potentially prove useful in screening for drug toxicity in mMSCs. *In vitro* evaluation of drug toxicity in mMSCs offers an alternative model for testing substances that are otherwise difficult to test in humans due to ethical considerations (Denning *et al.*, 2016). Moreover, mMSC differentiation capacity offers a more versatile and physiologically relevant model when compared to immortalized cell lines (Chang *et al.*, 2011). By employing ^1H NMR-based quality control, mMSC cultures could be

expanded with greatly reduced batch-to-batch variation, ensuring successful differentiation.

4.5 Creatine level fluctuations seem to be associated with mMSC differentiation

In terms of metabolomic analysis, we noticed a clear separation between adipocyte and osteoblast lineages. Control mMSC profiles seemed very similar to osteoblasts in terms of metabolite profile compared to adipocytes. The high similarity between osteoblasts and undifferentiated mMSCs has already been defined on an epigenetic level, therefore metabolic similarity seems unsurprising (Rauch *et al.*, 2019). We also identified several metabolites that were shown by multivariate analysis to be a source of distinction between adipocytes and osteoblasts. For example, creatine (Cr) and phosphocreatine (pCr) seemed to distinguish adipocytes from the other cell phenotypes. Literature on the physiological role of creatine in adipose tissue is rather limited, but currently suggests that creatine stimulates mitochondrial bioenergetics, suppresses diet-induced thermogenesis, and combats obesity (Kazak *et al.*, 2018).

4.6 Gene and protein expression data allows insight into cell biology changes during differentiation

Genomics and proteomics data obtained during mesenchymal differentiation showed some insights on how upstream factors impact the observed metabolite behaviors. Interestingly, we noted a drop in LDHA gene and protein expression in adipocytes nearing the end of differentiation. Considering the previously established significance of lactate production in adipocytes, this seemed rather counterintuitive. One possible explanation could be the overaccumulation of lactate in an *in vitro* setting. Whereas *in vivo* adipocyte-generated lactate is secreted into the bloodstream, in cell culture conditions lactate accumulates, leading to feedback-induced downregulation of LDH synthesis. A concrete

mechanism behind this is a subject of speculation, but it could be related to reversible inactivation of HIF-1 α hydroxylation and upregulated LDH isoform B synthesis (Nadal-Ginard, 1978; Lu *et al.*, 2005). Regardless of gene expression levels, ALT seemed to remain stable in both adipocytes and osteoblasts. It could therefore be assumed that the detected increase in ALT activity in osteoblasts can be associated with allosteric regulation or post-translational modification of the enzyme. Indeed, it has been shown that metabolites involved in bone maintenance pathways, such as L-cysteine or B-vitamins, exert varying levels of regulation on ALT (Adcock, Buckberry and Teesdale-Spittle, 1995). Moreover, ALT isoenzyme expression can also influence ALT activity (Jadaho *et al.*, 2004). Similarly, both osteogenic and adipogenic lineages showed relatively stable protein levels of PDH, seemingly completely independent of any fluctuations in PDH expression on a genomic level. However, the inactive pPDH was more prevalent in the osteoblasts. This seems to coincide with the preference for glycolytic energy generation in osteoblasts, as rapid production of ATP could activate pyruvate dehydrogenase kinases, which would then proceed to downregulate OXPHOS (Sugden and Holness, 2003).

4.7 Kinetics data clearly separated cell and tissue sample groups

In this MRes, we also investigated whether our metabolic phenotyping approach could be applied to wild-type tissue samples. In the context of ¹³C-labelled metabolite kinetics, we immediately noticed a change from mMSCs samples, which was we the presence of concentration plateaus (i.e metabolite steady states). In this case, all the variables within a system, such as the substrates and products of an enzymatic reaction, maintain a chemical equilibrium and the net reaction output is zero (Srinivasan, 2020). Assuming a stable biological environment, metabolites within tissues usually exist at steady states. Under such circumstances, obtaining data regarding metabolic fluxes is impossible. However, following addition of

^{13}C -labelled substrates, the parameters of a steady state reaction, namely the reactants, are perturbed, invoking a measurable metabolic flux through the reaction until a new steady state is achieved. Data acquired during this transition between two steady states describes the full extent of the metabolic changes associated with the particular sample. This framework has already been applied in clinical settings to study various tissues, such as heart and liver (Darpolor *et al.*, 2014; Cunningham *et al.*, 2016). Coming back to our study, the $[1-^{13}\text{C}]\text{lactate}/[1-^{13}\text{C}]\text{alanine}$ exchange ratios acquired in tissues represented a “finalized” reaction, unlike the ratios observed in the mMSC experiments, where steady states were not achieved during the same timeframe. This difference between cell and tissue samples likely originates from differences in quantity of samples used - cells were measured in number, while the tissues were weighed. The resulting higher biomass of tissue samples means higher catalytic enzyme and metabolite abundances, allowing enzymatic reactions to more easily reach steady states within a short time period. Future work, particularly regarding cell samples, should take these findings into account and ensure that metabolic flux data is representative of steady states.

4.8 Although initially successful, metabolic phenotyping of tissues presents further challenges

Such as with mMSCs, the $[1-^{13}\text{C}]\text{lactate}/[1-^{13}\text{C}]\text{alanine}$ ratios acquired from wild-type tissues seemed to be unique to each tissue. Except for liver, all tissues seemed presented higher flux of the ^{13}C label into lactate compared to alanine. This outcome is logical considering a significant portion of cells residing adipose, brain, and bone tissues either favor lactate production, or are predominantly glycolytic (Bouzier-Sore *et al.*, 2006; Lee *et al.*, 2017; Krycer *et al.*, 2020). The higher production of $[1-^{13}\text{C}]\text{alanine}$ over $[1-^{13}\text{C}]\text{lactate}$ observed is likely due to the high ALT expression in the liver, to

the point where ALT expression in the bloodstream is used a clinical marker for hepatic damage (Giannini, Testa and Savarino, 2005). All in all, the metabolic flux data acquired from these tissues were in range with parameters described by scientific literature and validated our primary hypotheses. However, we encountered issues while attempting to distinguish tissue metabolic profiles using metabolomics and PCA analysis. We have currently identified three reasons for why this could be the case. First, tissue sample preparation for ^1H NMR experiments revolved around daily preparation of buffer solutions as well as manual weighing of tissue. Operator error could thus be a source of inconsistent measurements, skewing the PCA model. Furthermore, the NMR buffer employed may be incompatible with metabolomics, as the background signals generated by the buffer components could mask key signals from biomarker metabolites. While the buffer solution was adequate for fluxomics, another sample preparation technique, such as methanol extraction, should be used for global metabolomic profiling (Gines *et al.*, 2018). Lastly, the regional complexity of tissues was largely ignored. Studies have shown that different regions within a tissue can have drastically different metabolisms (Tchernof *et al.*, 2006; Kleinridders *et al.*, 2018). As such, homogenizing an entire brain or bone yields a complex metabolic snapshot that may be heavily influenced by abnormalities within a single region. Taken together, all these factors pose as hurdles in terms of metabolomics, although our real-time fluxomics approach seems unaffected.

4.9 ^1H NMR data allows elucidation of the inflammatory mechanism in APP/PS1 mice

In the context of AD mouse tissues, we investigated the metabolic sexual dimorphism under systemic inflammation observed in APP/PS1 mice. A previous study had concluded that, following treatment with lipopolysaccharide (LPS), a downregulation of pyruvate metabolism could

be observed in hippocampi of male mice (Agostini *et al.*, 2020). We aimed to determine whether this phenomenon is observed in other tissues (liver and cerebral cortex), and to quantify the extent of inflammation effects. Livers from all four groups displayed no significant variance in [1-¹³C]lactate/[1-¹³C]alanine ratios. Furthermore, all ratios seemed to be close to the value of 1, indicating similar production levels of lactate and alanine, slightly higher than the ratio seen in the wild-type mice. It should be noted, however, that the wild-type mice were not subjected to the same control procedures (injection, behavioural testing) as AD mice. Interestingly, the overall concentration of lactate was consistently higher in LPS-treated male mice compared to their PBS-treated counterparts. Although, in contrast with hippocampi's data, our findings could be related to the work of Agostini and colleagues. For instance, key findings by other studies suggest that LPS upregulates glycolysis among other pathways, and that the APP/PS1 model mice present reduced neuronal lactate presence due to downregulated lactate transport between glia and neurons (Zhang *et al.*, 2018). We could therefore interpret a mechanism where the production of lactate in glia is excessively upregulated by LPS, but, due to impaired transport to neurons, brain lactate is released in the bloodstream, transported to the liver where it is metabolized. Interestingly, this phenomenon was unique to male mice. An explanation could be the sexual dimorphism in the context of pro-inflammatory cytokines. Adult female mice have been shown to produce more mild inflammatory response and are thus less susceptible to endotoxin (including LPS) exposure (Kuo, 2016).

Metabolomics analysis of AD mouse tissues suggested that the LPS treatment substantially alters the metabolome of AD mouse livers. Most of the LPS-treated liver data showed metabolic similarity regardless of sex. The remainder – PBS-treated male and female livers – were separated by

our PCA model. The latter phenomenon could be representative of sex asymmetry in terms of metabolic homeostasis observed across multiple species (Mauvais-Jarvis, 2015). Nonetheless, some LPS-treated livers indicated high metabolic similarity to female PBS-treated livers. A possible explanation is naturally occurring variability seen in living organism metabolisms (Pettersen, Marshall and White, 2018). Coupled with low number of animals used in this study, we cannot draw conclusions as to why this asymmetry was observed. Through PCA, we were able to identify creatine metabolism as a source of sexual dimorphism in APP/PS1 livers. Aberrant creatine metabolism has an established role in Alzheimer's Disease pathology, particularly in brain tissue, where it accumulates and forms deposits (Bürklen *et al.*, 2006). Future work could therefore investigate this connection between Alzheimer's and creatine metabolism, and how it affects the liver.

4.10 AD mouse livers metabolic profiles depend on sex and treatment

Across all AD mouse livers (both sexes and treatments), ALT gene and protein expression was strongly downregulated compared to the wild-type mice. These findings are concomitant with another study that looked at associations between liver enzymes and AD diagnosis in human patients (Nho *et al.*, 2019). In this study, researchers found that ALT levels were decreased and that the aspartate aminotransferase (AST) ratio with ALT was increased in patients with AD. The exact benefits of ALT gene downregulation to AD pathology remain elusive. Some potential candidates include altered glutamate metabolism and perturbed bioenergetics through gluconeogenesis downregulation (Isik and Bozoglu, 2010). Unlike ALT, genomics and proteomics data of LDH were quite different. LDH gene expression seemed to be downregulated exclusively in LPS-treated livers. As LPS is associated with glycolysis upregulation, reduction in LDH gene expression seems counterintuitive. Nonetheless,

literature suggests that the underlying mechanism could be associated not with regulation of the LDH gene, but rather with tissue injury cause by LPS supplementation (Ajuwon, Oguntibeju and Marnewick, 2014; Hamesch *et al.*, 2015). Following LPS administration, increased serum ALT and LDH levels can be detected in mice models, indicating acute liver injury. This theory, however, is contradicted by the elevated LDH protein expression in liver of LPS-treated male as seen in our proteomics data. Lastly, high presence of phosphorylated PDH in agreement with the PDH gene and protein expression across all groups represented a common AD-associated perturbation (Patel *et al.*, 2012b). Overall, the combination of metabolomics, genomics, and proteomics techniques provided deep insight on the effects of sex and inflammation on AD-affected liver tissue.

4.11 Amino acid metabolism seemingly plays a key role in AD cortex tissue

^1H NMR data acquired in AD-afflicted cortex showed that $[1-^{13}\text{C}]\text{lactate}/[1-^{13}\text{C}]\text{alanine}$ ratios in both sex and treatment groups were <1 , indicating the prioritization of alanine production. As previously discussed, lactate exchange between astrocytes and neurons is impaired in AD (Zhang *et al.*, 2018). Additionally, neurons do not possess sufficient levels of enzymes involved in β -oxidation to rely on fatty acids for energy generation (Panov *et al.*, 2014). The viable substrates left for ATP generation in AD neurons are therefore ketone bodies and amino acids (Cunnane *et al.*, 2012; Puchalska and Crawford, 2019). Our data could therefore be indicative of the latter - an upregulation of amino acid catabolism in order to satisfy the energetic demand in the AD neurons (Griffin and Bradshaw, 2017). Glutamate and glutamine are often identified as the most abundant amino acids in the brain. These two amino acids participate in a cycle termed the glutamate- glutamine cycle, where glutamate used in neuronal signaling is converted to glutamine in astrocytes, exported and taken up by neurons, and converted back to glutamate (Walton and

Dodd, 2007). While the primary function of this cycle is the replenishment of glutamatergic neurotransmitters in the neurons, AD-affected neurons can also direct glutamate towards energy production. The high production of [1-¹³C]alanine could therefore correspond to an increased flux of amino acids towards glutamate production. Astrocytes may support this pathway by upregulating glutamine output. However, as we did not measure glutamate concentration in our study, we cannot therefore be certain if this in fact occurs. Future work should remedy this gap in order to fully characterize the connection between [1-¹³C]alanine flux and AD brain metabolism.

In concordance with observed reduced [1-¹³C]lactate/[1-¹³C]alanine ratios, ALT gene expression in AD cortex seemed upregulated across most groups, with the exception of male PBS-treated cortices. The reason behind this observation is not clear, as sexual dimorphisms regarding amino acid metabolism in AD have not been well studied. However, these results should be taken with caution, as our studied wild-type was female, and not a littermate to the AD mice. Curiously, ALT protein expression data indicated a reduction in ALT across all groups. A similar mismatch between genomic and proteomic data is gathered from AD cortex tissue could also be observed in the context of LDH and PDH. While LDH gene expression seemed similar in all groups, it was drastically upregulated in the female PBS-treated cortex. In terms of protein expression, however, LDH levels were consistently higher in all AD cortices in comparison to wild-type tissue. These observations are suggestive of glycolysis upregulation in response to increased ATP demand in AD brain tissue, and are consistent with the stimulatory effect of LPS on glycolytic pathways. Lastly, gene expression of PDH seemed the highest in female PBS-treated cortex tissue, yet the highest levels of PDH protein were seen in both male cortex groups.

The extent of PDH phosphorylation seemed high in all groups, except for LPS-treated males.

4.12 Real-time study is imperative when correlating metabolomics, proteomics, and genomics

The discrepancy between genomic and proteomic data obtained from AD cortex tissue highlights an importance of the real-time aspect of metabolic studies. *In vivo*, both gene expression and protein expression are highly regulated processes that can be stimulated or suppressed by a plethora of stimuli. In response to physiological or pathological processes that invoke metabolic reprogramming in cells, the mechanism follows the central dogma order: genes are expressed, proteins are synthesized, and metabolites are produced (Veenstra, 2012). However, by the time metabolic signatures are observed by a technique such as ^1H NMR, feedback inhibition or other regulatory signals could have already downregulated gene or protein expression associated with a particular pathway. The temporal “snapshot” of the genome or the proteome acquired at any single time point can therefore be unrepresentative of the metabolic state of the target cell or tissue. Such could be the case with our qPCR and Western blot experiments. While the described scenario is applicable to other tissues, it seemed to be the most prevalent in the cortex, where little correlation could be seen between genomic, metabolomic, and proteomic data.

4.13 Tissue complexity limits reliability of acquired data

And yet, another explanation to the aforementioned issue may lie in our sample preparation method. For ^1H NMR sample preparation, we used pieces surgically removed from the cortex, rather than the whole cortex. This raises a potential problem related to cortex cell population ratios and their gene expression patterns. In the whole cortex, glial cells and neurons exist at a ratio of ~ 1.5 (glia to neurons) (Christopher S. von Bartheld, 2017).

Nevertheless, the cortex is composed of multiple anatomically defined areas and layers throughout which the glia-to-neuron ratios vary. As previously discussed, glia and neurons have unique metabolic patterns. Further complications arise when considering the differential gene and protein expression patterns across the multiple regions of the cortex, particularly in relation with AD severity (Herculano-Houzel, Watson and Paxinos, 2013; Xu *et al.*, 2019). As we did not consider this aspect when sampling the cortex tissue, it is likely that the cortex samples used in our experiments lacked consistency in terms of anatomical composition. This would have then resulted in differences both in protein and gene expression unrelated to either sex or treatment across all groups, which is what was observed.

4.14 Further development of NMR methodology is required

PCA of AD cortex samples failed to replicate the metabolic profile grouping pattern previously seen in AD liver tissue. In fact, no clear grouping was seen based on either sex or treatment. While creatine metabolism was again implicated as key player characterizing certain samples, other unidentified metabolites seemed to affect the model with the same impact. Curiously, there is large overlap between these newfound pivotal metabolites in the cortex, and those that only slightly affected the PCA model in AD livers. This likely represents the natural difference between the metabolic profiles of these two tissues due to their function, metabolism, and cell composition. Nonetheless, due to our inability to identify these molecules, it is uncertain what role they play and whether they have promise as targets in future NMR-based metabolic studies of AD. In our obtained NMR spectra, the signals of unidentified metabolites were mostly found in areas of high signal peak overlap, severely impeding identification attempts. It is thus imperative that our NMR methodology is improved to allow better peak separation. An NMR spectroscopy

technique termed heteronuclear single quantum coherence (HSQC) shows promise, as it would introduce a second dimension to the NMR spectra. The two dimensions correspond to different target nuclei, such as ^1H and ^{13}C , allowing observation of correlations between carbons and their attached protons. Many studies have successfully used ^1H - ^{13}C HSQC in real-time metabolic studies, even managing to monitor acetyl-CoA formation (Mahrous and Farag, 2015; Xu *et al.*, 2018). Therefore, introducing ^1H - ^{13}C HSQC into our study model could help elucidate metabolic profiles of AD tissues by separating signals, allowing circumvention of peak overlap.

4.15 Conclusion

Our study suffered from several limitations and flaws in design. Some drawbacks and potential improvements were already identified previously. Due to resource and time constraints, some of our data lacked statistical power to draw any concrete conclusions. Further repetition of these experiments would therefore be imperative to clarify relationships between data sets. For the analysis of AD mouse tissues, a significant drawback was the absence of a wild-type control of each sex and treatment. In the presence of such a control, we could have determined whether the sexual dimorphisms and treatment impacts observed in our tissue samples were exclusive to AD or were purely the result difference in sex and/or inflammatory effect. Tissue collection methods may also require a review, particularly in the brain, to prevent overlap of data from phenotypically distinct regions. Finally, the *in vitro* environment of this served as another limitation. The use of buffers and media enriched with specific metabolites might have affected resulted in metabolic signatures that would otherwise not be seen *in vivo*. Nevertheless, investigations of metabolic changes can greatly advance the fields of stem cell and AD research. The globally growing attention shift to studying the role of metabolites in physiology and pathophysiology show promise in unfolding

a unified framework in which metabolites, proteins, and genes cooperate to modify the identities and function of cells, tissues, and organs (Wishart, 2019).

In summary, our study confirmed that the real-time observation of metabolic changes linked with pyruvate metabolism can be used as biomarkers when determining cell and tissue phenotypes. Physiological processes, such as mesenchymal stem cell differentiation into adipocytes or osteoblasts, result in specific metabolic signatures detectable via ^1H NMR. Beside cell samples, we were also able to characterize wild-type mouse tissues based on the $[1-^{13}\text{C}]\text{lactate}/[1-^{13}\text{C}]\text{alanine}$ ratios. In AD model mouse livers and cortical tissues, flux data from ^{13}C -labelled metabolites was not directly definitive of sexual dimorphisms or treatments. However, AD fluxomic data provided insight on already established metabolic perturbations in AD seen in literature. We were also able to examine upstream proteomic and genomic changes associated with observed metabolite signatures. Our findings conclude that while not necessarily directly correlated with changes in metabolite levels, genomics and proteomics data could be indicative of regulatory mechanisms and/or alternative pathways. Finally, via metabolomics and multivariate analysis, we were able to determine some metabolites that also shown biomarker potential.

5. Bibliography:

1. bd Ghafar, S. Z. *et al.* (2020) 'Complementary NMR- and MS-based metabolomics approaches reveal the correlations of phytochemicals and biological activities in *Phyllanthus acidus* leaf extracts', *Food Research International*. Elsevier, 136(February), p. 109312. doi: 10.1016/j.foodres.2020.109312.
2. Acosta, C., Anderson, H. D. and Anderson, C. M. (2017) 'Astrocyte dysfunction in Alzheimer disease', *Journal of Neuroscience Research*, 95(12), pp. 2430–2447. doi: 10.1002/jnr.24075.
3. Adcock, H. J., Buckberry, L. D. and Teesdale-Spittle, P. H. (1995) 'The C-S lysis of L-cysteine conjugates by aspartate and alanine aminotransferase enzymes', *Human & Experimental Toxicology*, 14(5), pp. 422–427. doi: 10.1177/096032719501400506.
4. Agostini, A. *et al.* (2020) 'Sex-specific hippocampal metabolic signatures at the onset of systemic inflammation with lipopolysaccharide in the APP^{swE}/PS1^{dE9} mouse model of Alzheimer's disease', *Brain, Behavior, and Immunity*. Elsevier, 83(April 2019), pp. 87–111. doi: 10.1016/j.bbi.2019.09.019.
5. Ahmed, K. *et al.* (2010) 'An Autocrine Lactate Loop Mediates Insulin-Dependent Inhibition of Lipolysis through GPR81', *Cell Metabolism*, 11(4), pp. 311–319. doi: 10.1016/j.cmet.2010.02.012.
6. Ahn, E. *et al.* (2017) 'Temporal fluxomics reveals oscillations in TCA cycle flux throughout the mammalian cell cycle', *Molecular Systems Biology*, 13(11), p. 953. doi: 10.15252/msb.20177763.
7. Ajuwon, O. R. aza., Oguntibeju, O. O. moniy. and Marnewick, J. L. ucast. (2014) 'Amelioration of lipopolysaccharide-induced liver injury by aqueous rooibos (*Aspalathus linearis*) extract via inhibition of pro-inflammatory cytokines and oxidative stress', *BMC complementary*

- and alternative medicine*, 14, p. 392. doi: 10.1186/1472-6882-14-392.
8. Albers, M. J. *et al.* (2010) 'NIH Public Access', 68(20), pp. 8607–8615. doi: 10.1158/0008-5472.CAN-08-0749.Hyperpolarized.
 9. Alexandri, E. *et al.* (2017) 'High resolution NMR spectroscopy as a structural and analytical tool for unsaturated lipids in solution', *Molecules*, 22(10). doi: 10.3390/molecules22101663.
 10. Ambrosi, T. H. *et al.* (2017) 'Adipocyte Accumulation in the Bone Marrow during Obesity and Aging Impairs Stem Cell-Based Hematopoietic and Bone Regeneration', *Cell Stem Cell*, 20(6), pp. 771-784.e6. doi: 10.1016/j.stem.2017.02.009.
 11. Andrew, M. K. and Tierney, M. C. (2018) 'The puzzle of sex, gender and Alzheimer's disease: Why are women more often affected than men?', *Women's Health*, 14. doi: 10.1177/1745506518817995.
 12. Ardenkjær-Larsen, J. H. *et al.* (2003) 'Increase in signal-to-noise ratio of >10,000 times in liquid-state NMR', *Proceedings of the National Academy of Sciences of the United States of America*, 100(18), pp. 10158–10163. doi: 10.1073/pnas.1733835100.
 13. Attwell, D. and Laughlin, S. B. (2001) 'An energy budget for signaling in the grey matter of the brain', *Journal of Cerebral Blood Flow and Metabolism*, 21(10), pp. 1133–1145. doi: 10.1097/00004647-200110000-00001.
 14. Bélanger, M., Allaman, I. and Magistretti, P. J. (2011) 'Brain energy metabolism: Focus on Astrocyte-neuron metabolic cooperation', *Cell Metabolism*, 14(6), pp. 724–738. doi: 10.1016/j.cmet.2011.08.016.
 15. Bensard, C. L. *et al.* (2020) 'Regulation of Tumor Initiation by the Mitochondrial Pyruvate Carrier', *Cell Metabolism*, 31(2), pp. 284-300.e7. doi: 10.1016/j.cmet.2019.11.002.
 16. Bergmann, W., Rudolph, R. and Spohn, U. (1999) 'A bienzyme modified carbon paste electrode for amperometric detection of

- pyruvate', *Analytica Chimica Acta*, 394(2–3), pp. 233–241. doi: 10.1016/S0003-2670(99)00296-2.
17. Berthiaume, F., Maguire, T. J. and Yarmush, M. L. (2011) 'Tissue Engineering and Regenerative Medicine: History, Progress, and Challenges', *Annual Review of Chemical and Biomolecular Engineering*, 2(1), pp. 403–430. doi: 10.1146/annurev-chembioeng-061010-114257.
 18. Bhirde, A. *et al.* (2011) 'Nanoparticles for cell labeling', *Nanoscale*, 3(1), pp. 142–153. doi: 10.1039/c0nr00493f.
 19. Bjerrum, J. T. *veite.* (2015) *Metabonomics: methods and protocols: preface, Methods in molecular biology (Clifton, N.J.)*.
 20. Boesch, C. and Kreis, R. (2000) 'Observation of intramyocellular lipids by 1H-magnetic resonance spectroscopy', *Annals of the New York Academy of Sciences*, 904, pp. 25–31. doi: 10.1111/j.1749-6632.2000.tb06417.x.
 21. Bouzier-Sore, A. K. *et al.* (2006) 'Competition between glucose and lactate as oxidative energy substrates in both neurons and astrocytes: A comparative NMR study', *European Journal of Neuroscience*, 24(6), pp. 1687–1694. doi: 10.1111/j.1460-9568.2006.05056.x.
 22. Bricker, D. K. *et al.* (2012) 'A Mitochondrial Pyruvate Carrier Required for Pyruvate Uptake in Yeast, Drosophila, and Humans', *Science*, 337(July), pp. 96–100. doi: 10.7551/mitpress/8053.003.0075.
 23. Bröer, S. *et al.* (2007) 'Alanine metabolism, transport, and cycling in the brain', *Journal of Neurochemistry*, 102(6), pp. 1758–1770. doi: 10.1111/j.1471-4159.2007.04654.x.
 24. Brosnan, J. T. (2000) 'Glutamate, at the Interface between Amino Acid and Carbohydrate Metabolism', *The Journal of Nutrition*, 130(4), pp. 988S-990S. doi: 10.1093/jn/130.4.988s.
 25. Bürklen, T. S. *et al.* (2006) 'The creatine kinase/creatine connection to

- alzheimer's disease: CK-inactivation, APP-CK complexes and focal creatine deposits', *Journal of Biomedicine and Biotechnology*, 2006, pp. 1–11. doi: 10.1155/JBB/2006/35936.
26. Casley, C. S. *et al.* (2002) 'b -Amyloid inhibits integrated mitochondrial respiration and key enzyme activities', pp. 91–100.
27. Celton, M. *et al.* (2012) 'A comparative transcriptomic, fluxomic and metabolomic analysis of the response of *Saccharomyces cerevisiae* to increases in NADPH oxidation', *BMC Genomics*, 13(1). doi: 10.1186/1471-2164-13-317.
28. Chan, C. K. F. *et al.* (2018) 'Identification of the Human Skeletal Stem Cell', *Cell*. Elsevier Inc., 175(1), pp. 43-56.e21. doi: 10.1016/j.cell.2018.07.029.
29. Chang, Y. *et al.* (2011) 'In vitro toxicity evaluation of graphene oxide on A549 cells', *Toxicology Letters*. Elsevier Ireland Ltd, 200(3), pp. 201–210. doi: 10.1016/j.toxlet.2010.11.016.
30. Chen, C.-T. *et al.* (2008) 'Coordinated Changes of Mitochondrial Biogenesis and Antioxidant Enzymes During Osteogenic Differentiation of Human Mesenchymal Stem Cells', *Stem Cells*, 26(4), pp. 960–968. doi: 10.1634/stemcells.2007-0509.
31. Chen, H. Y. *et al.* (2020) 'Hyperpolarized ¹³C-pyruvate MRI detects real-time metabolic flux in prostate cancer metastases to bone and liver: a clinical feasibility study', *Prostate Cancer and Prostatic Diseases*. Springer US, 23(2), pp. 269–276. doi: 10.1038/s41391-019-0180-z.
32. Christopher S. von Bartheld, J. B. and S. H.-H. (2017) '乳鼠心肌提取 HHS Public Access', *Physiology & behavior*, 176(12), pp. 139–148. doi: 10.1002/cne.24040.The.
33. Ciszak, E. M. *et al.* (2003) 'Structural basis for flip-flop action of thiamin pyrophosphate-dependent enzymes revealed by human

- pyruvate dehydrogenase', *Journal of Biological Chemistry*. © 2003 ASBMB. Currently published by Elsevier Inc; originally published by American Society for Biochemistry and Molecular Biology., 278(23), pp. 21240–21246. doi: 10.1074/jbc.M300339200.
34. Coppel, J. A. *et al.* (2010) 'Hepatic Veno-Occlusive Disease following Stem Cell Transplantation: Incidence, Clinical Course, and Outcome', *Biology of Blood and Marrow Transplantation*. Elsevier Ltd, 16(2), pp. 157–168. doi: 10.1016/j.bbmt.2009.08.024.
35. Coss, C. C. *et al.* (2012) 'Alanine aminotransferase regulation by androgens in non-hepatic tissues', *Pharmaceutical Research*, 29(4), pp. 1046–1056. doi: 10.1007/s11095-011-0649-5.
36. Crisan, M. *et al.* (2008) 'A Perivascular Origin for Mesenchymal Stem Cells in Multiple Human Organs', *Cell Stem Cell*, 3(3), pp. 301–313. doi: 10.1016/j.stem.2008.07.003.
37. Cunningham, C. H. *et al.* (2016) 'Hyperpolarized ¹³C Metabolic MRI of the Human Heart: Initial Experience', *Circulation Research*, 119(11), pp. 1177–1182. doi: 10.1161/CIRCRESAHA.116.309769.
38. Curthoys, N. P. (1995) 'Regulation of Glutaminase Activity and Glutamine Metabolism', *Annual Review of Nutrition*, 15(1), pp. 133–159. doi: 10.1146/annurev.nutr.15.1.133.
39. Darpolor, M. M. *et al.* (2014) 'The aspartate metabolism pathway is differentiable in human hepatocellular carcinoma: Transcriptomics and ¹³C-isotope based metabolomics', *NMR in Biomedicine*, 27(4), pp. 381–389. doi: 10.1002/nbm.3072.
40. DeBerardinis, R. J. *et al.* (2008) 'The Biology of Cancer: Metabolic Reprogramming Fuels Cell Growth and Proliferation', *Cell Metabolism*, 7(1), pp. 11–20. doi: 10.1016/j.cmet.2007.10.002.
41. Denning, C. *et al.* (2016) 'Cardiomyocytes from human pluripotent stem cells: From laboratory curiosity to industrial biomedical

- platform', *Biochimica et Biophysica Acta - Molecular Cell Research*.
The Authors, 1863(7), pp. 1728–1748. doi:
10.1016/j.bbamcr.2015.10.014.
42. Dienel, G. A. (2019) 'Brain glucose metabolism: Integration of energetics with function', *Physiological Reviews*, 99(1), pp. 949–1045. doi: 10.1152/physrev.00062.2017.
43. Diers, A. R. *et al.* (2016) 'Pyruvate fuels mitochondrial respiration and proliferation of breast cancer cells', *Biochemical Journal*, 444(3), pp. 561–571. doi: 10.1042/BJ20120294.Pyruvate.
44. Dominici, M. *et al.* (2006) 'Minimal criteria for defining multipotent mesenchymal stromal cells. The International Society for Cellular Therapy position statement', *Cytotherapy*. Elsevier, 8(4), pp. 315–317. doi: 10.1080/14653240600855905.
45. Drent, M. *et al.* (1996) 'Usefulness of lactate dehydrogenase and its isoenzymes as indicators of lung damage or inflammation', *European Respiratory Journal*, 9(8), pp. 1736–1742. doi: 10.1183/09031936.96.09081736.
46. Emwas, A. H. *et al.* (2019) 'Nmr spectroscopy for metabolomics research', *Metabolites*, 9(7). doi: 10.3390/metabo9070123.
47. Evans, M. L. *et al.* (2004) 'Alanine infusion during hypoglycaemia partly supports cognitive performance in healthy human subjects', *Diabetic Medicine*, 21(5), pp. 440–446. doi: 10.1111/j.1464.
48. Ewaschuk, J. B. *et al.* (2004) 'High-performance liquid chromatographic assay of lactic, pyruvic and acetic acids and lactic acid stereoisomers in calf feces, rumen fluid and urine', *Journal of Chromatography B: Analytical Technologies in the Biomedical and Life Sciences*, 805(2), pp. 347–351. doi: 10.1016/j.jchromb.2004.03.004.
49. Fantin, V. R., St-Pierre, J. and Leder, P. (2006) 'Attenuation of LDH-A expression uncovers a link between glycolysis, mitochondrial

- physiology, and tumor maintenance', *Cancer Cell*, 9(6), pp. 425–434.
doi: 10.1016/j.ccr.2006.04.023.
50. Feldman-Salit, A. *et al.* (2013) 'Regulation of the activity of lactate dehydrogenases from four lactic acid bacteria', *Journal of Biological Chemistry*, 288(29), pp. 21295–21306. doi: 10.1074/jbc.M113.458265.
51. Felig, P. (1973) 'The glucose-alanine cycle', *Metabolism*, 22(2), pp. 179–207. doi: 10.1016/0026-0495(73)90269-2.
52. Felig, P. (1975) 'Amino Acid Metabolism in Man', *Annual Review of Biochemistry*, 44(1), pp. 933–955. doi: 10.1146/annurev.bi.44.070175.004441.
53. Feng, Y. *et al.* (2018) 'Lactate dehydrogenase A: A key player in carcinogenesis and potential target in cancer therapy', *Cancer Medicine*, 7(12), pp. 6124–6136. doi: 10.1002/cam4.1820.
54. Fernandez, S. *et al.* (2019) 'Adipocyte ACLY Facilitates Dietary Carbohydrate Handling to Maintain Metabolic Homeostasis in Females', *Cell Reports*. ElsevierCompany., 27(9), pp. 2772-2784.e6. doi: 10.1016/j.celrep.2019.04.112.
55. Fiehn, O. (2002) 'Metabolomics - The link between genotypes and phenotypes', *Plant Molecular Biology*, 48(1–2), pp. 155–171. doi: 10.1023/A:1013713905833.
56. Firth, J. D., Ebert, B. L. and Ratcliffe, P. J. (1995) 'Hypoxic regulation of lactate dehydrogenase A: Interaction between hypoxia-inducible factor 1 and cAMP response elements', *Journal of Biological Chemistry*. © 1995 ASBMB. Currently published by Elsevier Inc; originally published by American Society for Biochemistry and Molecular Biology., 270(36), pp. 21021–21027. doi: 10.1074/jbc.270.36.21021.
57. Folmes, C. D. L. (2017) 'Energy Metabolism in the Acquisition and

- Maintenance of Stemness', *Physiology and Behavior*, 176(1), pp. 139–148. doi: 10.1016/j.physbeh.2017.03.040.
58. Foster, C. J. *et al.* (2019) *From Escherichia coli mutant 13C labeling data to a core kinetic model: A kinetic model parameterization pipeline*, *PLoS Computational Biology*. doi: 10.1371/journal.pcbi.1007319.
59. FUKUDA, H., KATSURADA, A. and IRITANI, N. (1992) 'Effects of nutrients and hormones on gene expression of ATP citrate-lyase in rat liver', *European Journal of Biochemistry*, 209(1), pp. 217–222. doi: 10.1111/j.1432-1033.1992.tb17279.x.
60. George, S., Hamblin, M. R. and Abrahamse, H. (2019) 'Differentiation of Mesenchymal Stem Cells to Neuroglia : in the Context of Cell Signalling'. *Stem Cell Reviews and Reports*, pp. 814–826.
61. Giannini, E. G., Testa, R. and Savarino, V. (2005) 'Liver enzyme alteration: A guide for clinicians', *Cmaj*, 172(3), pp. 367–379. doi: 10.1503/cmaj.1040752.
62. Gines, B. R. *et al.* (2018) 'Influence of metabolite extraction methods on 1H-NMR-based metabolomic profiling of enteropathogenic yersinia', *Methods and Protocols*, 1(4), pp. 1–11. doi: 10.3390/mps1040045.
63. Glinghammar, B. *et al.* (2009) 'Detection of the mitochondrial and catalytically active alanine aminotransferase in human tissues and plasma', *International Journal of Molecular Medicine*, 23(4), pp. 621–631. doi: 10.3892/ijmm.
64. Goldberg, E. *et al.* (2010) 'LDHC: The ultimate testis-specific gene', *Journal of Andrology*, 31(1), pp. 86–94. doi: 10.2164/jandrol.109.008367.
65. Granlund, K. L. *et al.* (2020) 'Hyperpolarized MRI of human prostate cancer reveals increased lactate with tumor grade driven by

- monocarboxylate transporter 1', *Cell Metabolism*, 31(1), pp. 105–114. doi: 10.1016/j.cmet.2019.08.024.Hyperpolarized.
66. Gray, L. R., Tompkins, S. C. and Taylor, E. B. (2014) 'Regulation of pyruvate metabolism and human disease', *Cellular and Molecular Life Sciences*, 71(14), pp. 2577–2604. doi: 10.1007/s00018-013-1539-2.
67. Greenhaff, P. L. *et al.* (2004) 'Metabolic inertia in contracting skeletal muscle: A novel approach for pharmacological intervention in peripheral vascular disease', *British Journal of Clinical Pharmacology*, 57(3), pp. 237–243. doi: 10.1046/j.1365-2125.2003.01989.x.
68. Gregoire, F. M., Smas, C. M. and Sul, H. S. (1998) 'Understanding adipocyte differentiation', *Physiological Reviews*, 78(3), pp. 783–809. doi: 10.1152/physrev.1998.78.3.783.
69. Griffin, J. W. D. and Bradshaw, P. C. (2017) 'Amino Acid Catabolism in Alzheimer's Disease Brain: Friend or Foe?', *Oxidative Medicine and Cellular Longevity*. Hindawi Publishing Corporation, 2017. doi: 10.1155/2017/5472792.
70. Gupta, V. and Bamezai, R. N. K. (2010) 'Human pyruvate kinase M2: A multifunctional protein', *Protein Science*, 19(11), pp. 2031–2044. doi: 10.1002/pro.505.
71. Gutte, H. *et al.* (2015) 'The use of dynamic nuclear polarization (13)C-pyruvate MRS in cancer.', *American journal of nuclear medicine and molecular imaging*, 5(5), pp. 548–60. Available at: <http://www.ncbi.nlm.nih.gov/pubmed/26550544><http://www.pubmedcentral.nih.gov/articlerender.fcgi?artid=PMC4620180>.
72. Hamesch, k. *et al.* (2015) 'Lipopolysaccharide-induced inflammatory liver injury in mice', *Laboratory Animals*, 49, pp. 37–46. doi: 10.1177/0023677215570087.
73. Hamidouche, Z. *et al.* (2008) 'FHL2 mediates dexamethasone-induced mesenchymal cell differentiation into osteoblasts by activating

- Wnt/ β -catenin signaling-dependent Runx2 expression', *The FASEB Journal*, 22(11), pp. 3813–3822. doi: 10.1096/fj.08-106302.
74. Hanahan, D. and Weinberg, R. A. (2011) 'Review Hallmarks of Cancer : The Next Generation', *Cell*. Elsevier Inc., 144(5), pp. 646–674. doi: 10.1016/j.cell.2011.02.013.
75. Hassel, B. (2000) 'Carboxylation and anaplerosis in neurons and glia', *Molecular Neurobiology*, 22(1–3), pp. 21–40. doi: 10.1385/mn:22:1-3:021.
76. Herculano-Houzel, S., Watson, C. and Paxinos, G. (2013) 'Distribution of neurons in functional areas of the mouse cerebral cortex reveals quantitatively different cortical zones', *Frontiers in Neuroanatomy*, 7(OCT), pp. 1–14. doi: 10.3389/fnana.2013.00035.
77. Holness, M. J. and Sugden, M. C. (2003) 'Regulation of pyruvate dehydrogenase complex activity by reversible phosphorylation', *Biochemical Society Transactions*, 31(6), pp. 1143–1151. doi: 10.1042/bst0311143.
78. Horan, M. P., Pichaud, N. and Ballard, J. W. O. (2012) 'Review: Quantifying mitochondrial dysfunction in complex diseases of aging', *Journals of Gerontology - Series A Biological Sciences and Medical Sciences*, 67 A(10), pp. 1022–1035. doi: 10.1093/gerona/qlr263.
79. Houthuijzen, J. M. *et al.* (2012) 'The role of mesenchymal stem cells in anti-cancer drug resistance and tumour progression', *British Journal of Cancer*. Nature Publishing Group, 106(12), pp. 1901–1906. doi: 10.1038/bjc.2012.201.
80. Huang, B. *et al.* (1998) 'Isoenzymes of pyruvate dehydrogenase phosphatase. DNA-derived amino acid sequences, expression, and regulation', *Journal of Biological Chemistry*. © 1998 ASBMB. Currently published by Elsevier Inc; originally published by American Society for Biochemistry and Molecular Biology., 273(28), pp. 17680–

17688. doi: 10.1074/jbc.273.28.17680.
81. Hui, S. *et al.* (2017) 'Glucose feeds the TCA cycle via circulating lactate', *Nature*. Nature Publishing Group, 551(7678), pp. 115–118. doi: 10.1038/nature24057.
82. Ioannou, M. S. *et al.* (2019) 'Neuron-Astrocyte Metabolic Coupling Protects against Activity-Induced Fatty Acid Toxicity', *Cell*. Elsevier Inc., 177(6), pp. 1522-1535.e14. doi: 10.1016/j.cell.2019.04.001.
83. Isik, A. T. and Bozoglu, E. (2010) 'Insulin resistance in Alzheimer disease', *Handbook of Type 1 Diabetes Mellitus: Etiology, Diagnosis, and Treatment*, pp. 481–489. doi: 10.1201/b13935-9.
84. Isopi, E. *et al.* (2015) 'Neurobiology of Disease Pyruvate prevents the development of age-dependent cognitive deficits in a mouse model of Alzheimer's disease without reducing amyloid and tau pathology', *Neurobiology of Disease*. Elsevier Inc., 81, pp. 214–224. doi: 10.1016/j.nbd.2014.11.013.
85. Ito, K. and Suda, T. (2014) 'Metabolic requirements for the maintenance of self-renewing stem cells', *Nature Reviews Molecular Cell Biology*, 15(4), pp. 243–256. doi: 10.1038/nrm3772.
86. Jadhav, S. B. *et al.* (2004) 'Murine Alanine Aminotransferase: cDNA Cloning, Functional Expression, and Differential Gene Regulation in Mouse Fatty Liver', *Hepatology*, 39(5), pp. 1297–1302. doi: 10.1002/hep.20182.
87. Jurgielewicz, P. *et al.* (2017) 'New Imaging Probes to Track Cell Fate: Reporter Genes in Stem Cell Research Piotr', *Cellular and Molecular Life Sciences*, 74(24), pp. 4455–4469. doi: 10.1016/j.physbeh.2017.03.040.
88. Kazak, L. *et al.* (2018) 'HHS Public Access', 26(4), pp. 660–671. doi: 10.1016/j.cmet.2017.08.009.Genetic.
89. Kfoury, Y. and Scadden, D. T. (2015) 'Mesenchymal cell contributions

- to the stem cell niche', *Cell Stem Cell*. Elsevier Inc., 16(3), pp. 239–253. doi: 10.1016/j.stem.2015.02.019.
90. Kim, J. W. *et al.* (2006) 'HIF-1-mediated expression of pyruvate dehydrogenase kinase: A metabolic switch required for cellular adaptation to hypoxia', *Cell Metabolism*, 3(3), pp. 177–185. doi: 10.1016/j.cmet.2006.02.002.
91. Kinney, J. W. *et al.* (2018) 'Inflammation as a central mechanism in Alzheimer's disease', *Alzheimer's and Dementia: Translational Research and Clinical Interventions*. Elsevier Inc., 4, pp. 575–590. doi: 10.1016/j.trci.2018.06.014.
92. Klein, S. L. and Flanagan, K. L. (2016) 'Sex differences in immune responses', *Nature Reviews Immunology*. Nature Publishing Group, 16(10), pp. 626–638. doi: 10.1038/nri.2016.90.
93. Kleinridders, A. *et al.* (2018) 'Regional differences in brain glucose metabolism determined by imaging mass spectrometry', *Molecular Metabolism*. Elsevier GmbH, 12(April), pp. 113–121. doi: 10.1016/j.molmet.2018.03.013.
94. Klyuyeva, A. *et al.* (2019) 'Tissue-specific kinase expression and activity regulate flux through the pyruvate dehydrogenase complex', *Journal of Biological Chemistry*, 294(3), pp. 838–851. doi: 10.1074/jbc.RA118.006433.
95. Koyama, A. *et al.* (2013) 'The role of peripheral inflammatory markers in dementia and Alzheimer's disease: A meta-analysis', *Journals of Gerontology - Series A Biological Sciences and Medical Sciences*, 68(4), pp. 433–440. doi: 10.1093/gerona/gls187.
96. Kraus, N. A. *et al.* (2016) 'Quantitative assessment of adipocyte differentiation in cell culture', *Adipocyte*. Taylor & Francis, 5(4), pp. 351–358. doi: 10.1080/21623945.2016.1240137.
97. Krycer, J. R. *et al.* (2020) 'Lactate production is a prioritized feature of

- adipocyte metabolism', *Journal of Biological Chemistry*, 295(1), pp. 83–98. doi: 10.1074/jbc.RA119.011178.
98. Kuo, S. M. (2016) 'Gender difference in bacteria endotoxin-induced inflammatory and anorexic responses', *PLoS ONE*, 11(9), pp. 1–12. doi: 10.1371/journal.pone.0162971.
99. Landau, B. R. and Wahren, J. (1988) 'Quantification of the pathways followed in hepatic glycogen formation from glucose', *The FASEB Journal*, 2(8), pp. 2368–2375. doi: 10.1096/fasebj.2.8.3282961.
100. Laughton, J. D. *et al.* (2000) 'Differential messenger RNA distribution of lactate dehydrogenase LDH-1 and LDH-5 isoforms in the rat brain', *Neuroscience*, 96(3), pp. 619–625. doi: 10.1016/S0306-4522(99)00580-1.
101. Lee, W. C. *et al.* (2017) 'Energy metabolism of the osteoblast: Implications for osteoporosis', *Endocrine Reviews*, 38(3), pp. 255–266. doi: 10.1210/er.2017-00064.
102. Levenberg, S. *et al.* (2002) 'Endothelial cells derived from human embryonic stem cells', *Proceedings of the National Academy of Sciences of the United States of America*, 99(7), pp. 4391–4396. doi: 10.1073/pnas.032074999.
103. Lewis, B. C. *et al.* (1997) 'Identification of putative c-Myc-responsive genes: characterization of rcl, a novel growth-related gene.', *Molecular and Cellular Biology*, 17(9), pp. 4967–4978. doi: 10.1128/mcb.17.9.4967.
104. Li, N. and Hua, J. (2017) 'Interactions between mesenchymal stem cells and the immune system', *Cellular and Molecular Life Sciences*, 74(13), pp. 2345–2360. doi: 10.1007/s00018-017-2473-5.
105. Liu, H., Xia, X. and Li, B. (2015) 'Mesenchymal stem cell aging: Mechanisms and influences on skeletal and non-skeletal tissues', *Experimental Biology and Medicine*, 240(8), pp. 1099–1106. doi:

10.1177/1535370215591828.

106. Liu, L. *et al.* (2008) 'Expression, purification, and initial characterization of human alanine aminotransferase (ALT) isoenzyme 1 and 2 in High-five insect cells', *Protein Expression and Purification*, 60(2), pp. 225–231. doi: 10.1016/j.pep.2008.04.006.
107. Loeffler, J. *et al.* (2018) 'The Metabolic Microenvironment Steers Bone Tissue Regeneration', *Trends in Endocrinology and Metabolism*, 29(2), pp. 99–110. doi: 10.1016/j.tem.2017.11.008.
108. Long, F. (2012) 'Building strong bones: Molecular regulation of the osteoblast lineage', *Nature Reviews Molecular Cell Biology*. Nature Publishing Group, 13(1), pp. 27–38. doi: 10.1038/nrm3254.
109. Lu, H. *et al.* (2005) 'Reversible inactivation of HIF-1 prolyl hydroxylases allows cell metabolism to control basal HIF-1', *Journal of Biological Chemistry*, 280(51), pp. 41928–41939. doi: 10.1074/jbc.M508718200.
110. Lunt, S. Y. and Vander Heiden, M. G. (2011) 'Aerobic Glycolysis: Meeting the Metabolic Requirements of Cell Proliferation', *Annual Review of Cell and Developmental Biology*, 27(1), pp. 441–464. doi: 10.1146/annurev-cellbio-092910-154237.
111. MacDonell, R., Hamrick, M. W. and Isales, C. M. (2016) 'Protein/amino-acid modulation of bone cell function', *BoneKEY Reports*. Nature Publishing Group, 5(AUGUST), pp. 1–7. doi: 10.1038/bonekey.2016.58.
112. Magistretti, P. J. and Allaman, I. (2018) 'Lactate in the brain: From metabolic end-product to signalling molecule', *Nature Reviews Neuroscience*. Nature Publishing Group, 19(4), pp. 235–249. doi: 10.1038/nrn.2018.19.
113. Maher, S. A. *et al.* (2018) 'Serum lactate and mortality in emergency department patients with cancer', *Western Journal of*

- Emergency Medicine*, 19(5), pp. 827–833. doi: 10.5811/westjem.2018.6.37295.
114. Mahrous, E. A. and Farag, M. A. (2015) 'Two dimensional NMR spectroscopic approaches for exploring plant metabolome: A review', *Journal of Advanced Research*. Cairo University, 6(1), pp. 3–15. doi: 10.1016/j.jare.2014.10.003.
115. Mao, A. S. and Mooney, D. J. (2015) 'Regenerative medicine: Current therapies and future directions', *Proceedings of the National Academy of Sciences of the United States of America*, 112(47), pp. 14452–14459. doi: 10.1073/pnas.1508520112.
116. Markert, C. L., Shaklee, J. B. and Whitt, G. S. (1975) 'Evolution of a gene', *Science*, 189(4197), pp. 102–114. doi: 10.1126/science.1138367.
117. Martínez-Reyes, I. and Chandel, N. S. (2020) 'Mitochondrial TCA cycle metabolites control physiology and disease', *Nature Communications*. Springer US, 11(1), pp. 1–11. doi: 10.1038/s41467-019-13668-3.
118. Mauvais-Jarvis, F. (2015) 'Sex differences in metabolic homeostasis, diabetes, and obesity', *Biology of Sex Differences*. *Biology of Sex Differences*, 6(1), pp. 1–9. doi: 10.1186/s13293-015-0033-y.
119. McCall, B. (2012) 'UK announces strategy for regenerative medicine', *The Lancet*. Elsevier Ltd, 379(9822), p. 1183. doi: 10.1016/S0140-6736(12)60493-0.
120. Mechie, N. C. *et al.* (2015) 'Association of serum vitamin B12 levels with stage of liver fibrosis and treatment outcome in patients with chronic hepatitis C virus genotype 1 infection: A retrospective study *Gastroenterology*', *BMC Research Notes*. BioMed Central, 8(1), pp. 1–8. doi: 10.1186/s13104-015-1248-z.

121. Merritt, M. E. *et al.* (2007) 'Hyperpolarized ¹³C allows a direct measure of flux through a single enzyme-catalyzed step by NMR', *Proceedings of the National Academy of Sciences of the United States of America*, 104(50), pp. 19773–19777. doi: 10.1073/pnas.0706235104.
122. Michelson, M. *et al.* (2001) 'Inborn errors of metabolism: A cause of abnormal brain development', *Neurology*. Minneapolis : Lancet Publications, 56(10), pp. 1265–1272. doi: 10.1212/WNL.56.10.1265.
123. Mink, J. W., Blumenshine, R. J. and Adams, D. B. (1981) 'Ratio of central nervous system to body metabolism in vertebrates: Its constancy and functional basis', *American Journal of Physiology - Regulatory Integrative and Comparative Physiology*, 10(2), pp. 203–212. doi: 10.1152/ajpregu.1981.241.3.r203.
124. Minniti G, Cerone R, D. T. E. (1982) 'Analytical biochemistry.', *Analytical biochemistry*. Orlando, FL : Academic Press, 122(1), p. 173.
125. Mookerjee, S. A. *et al.* (2017) 'Quantifying intracellular rates of glycolytic and oxidative ATP production and consumption using extracellular flux measurements', *Journal of Biological Chemistry*, 292(17), pp. 7189–7207. doi: 10.1074/jbc.M116.774471.
126. Morales-Alamo, D. *et al.* (2018) 'Skeletal muscle pyruvate dehydrogenase phosphorylation and lactate accumulation during sprint exercise in normoxia and severe acute hypoxia: Effects of antioxidants', *Frontiers in Physiology*, 9(MAR). doi: 10.3389/fphys.2018.00188.
127. Moya, A. *et al.* (2018) 'Human Mesenchymal Stem Cell Failure to Adapt to Glucose Shortage and Rapidly Use Intracellular Energy Reserves Through Glycolysis Explains Poor Cell Survival After Implantation', *Stem Cells*, 36(3), pp. 363–376. doi: 10.1002/stem.2763.

128. Mushahary, D. *et al.* (2018) 'Isolation, cultivation, and characterization of human mesenchymal stem cells', *Cytometry Part A*, 93(1), pp. 19–31. doi: 10.1002/cyto.a.23242.
129. Nadal-Ginard, B. (1978) 'Regulation of lactate dehydrogenase levels in the mouse.', *Journal of Biological Chemistry*, 253(1), pp. 170–177. doi: 10.1016/S0021-9258(17)38284-4.
130. Nagana Gowda, G. A. and Djukovic, D. (2014) 'Overview of mass spectrometry-based metabolomics: Opportunities and challenges', *Methods in Molecular Biology*, 1198, pp. 3–12. doi: 10.1007/978-1-4939-1258-2_1.
131. Nagana Gowda, G. A., Shanaiah, N. and Raftery, D. (2019) 'Isotope Enhanced Approaches in Metabolomics', *Advances in Experimental Medicine and Biology*, 176(3), pp. 147–164. doi: 10.1007/978-94-007-4954-2.
132. Nath, S. (2016) 'The thermodynamic efficiency of ATP synthesis in oxidative phosphorylation', *Biophysical Chemistry*, 219, pp. 69–74. doi: 10.1016/j.bpc.2016.10.002.
133. Nho, K. *et al.* (2019) 'Association of Altered Liver Enzymes With Alzheimer Disease Diagnosis, Cognition, Neuroimaging Measures, and Cerebrospinal Fluid Biomarkers', *JAMA network open*, 2(7), p. e197978. doi: 10.1001/jamanetworkopen.2019.7978.
134. Nuttall, M. E. *et al.* (1998) 'Human trabecular bone cells are able to express both osteoblastic and adipocytic phenotype: Implications for osteopenic disorders', *Journal of Bone and Mineral Research*, 13(3), pp. 371–382. doi: 10.1359/jbmr.1998.13.3.371.
135. O'Dowd, A. (2013) 'Peers call for UK to harness "enormous" potential of regenerative medicine.', *BMJ (Clinical research ed.)*, 347(July), p. 201314. doi: 10.1136/bmj.f4248.
136. Orkin, S. H. and Zon, L. I. (2008) 'Hematopoiesis: An Evolving

- Paradigm for Stem Cell Biology', *Cell*, 132(4), pp. 631–644. doi: 10.1016/j.cell.2008.01.025.
137. Owen, O. E., Kalhan, S. C. and Hanson, R. W. (2002) 'The key role of anaplerosis and cataplerosis for citric acid cycle function', *Journal of Biological Chemistry*, 277(34), pp. 30409–30412. doi: 10.1074/jbc.R200006200.
138. Palomäki, S. *et al.* (2013) 'HIF-1 α is upregulated in human mesenchymal stem cells', *Stem Cells*, 31(9), pp. 1902–1909. doi: 10.1002/stem.1435.
139. Panov, A. *et al.* (2014) 'Fatty acids in energy metabolism of the central nervous system', *BioMed Research International*. Hindawi Publishing Corporation, 2014. doi: 10.1155/2014/472459.
140. Parnetti, L. *et al.* (1995) 'Increased cerebrospinal fluid pyruvate levels in Alzheimer's disease', *Neuroscience Letters*, 199(3), pp. 231–233.
141. Patel, A. B. and Tiwari, V. (2014) 'Pyruvate Carboxylase and Pentose Phosphate Fluxes are Reduced in A β PP-PS1 Mouse Model of Alzheimer's Disease: A ¹³C NMR Study', *Journal of Alzheimer's Disease*, 41(2), pp. 387–399. doi: 10.3233/JAD-122449.
142. Patel, K. P. *et al.* (2012a) 'The spectrum of pyruvate dehydrogenase complex deficiency: Clinical, biochemical and genetic features in 371 patients', *Molecular Genetics and Metabolism*, 105(1), pp. 34–43. doi: 10.1016/j.ymgme.2011.09.032.
143. Patel, K. P. *et al.* (2012b) 'The spectrum of pyruvate dehydrogenase complex deficiency: Clinical, biochemical and genetic features in 371 patients', *Molecular Genetics and Metabolism*. Elsevier Inc., 105(1), pp. 34–43. doi: 10.1016/j.ymgme.2011.09.032.
144. Pattappa, G. *et al.* (2011) 'The metabolism of human mesenchymal stem cells during proliferation and differentiation',

- Journal of Cellular Physiology*, 226(10), pp. 2562–2570. doi: 10.1002/jcp.22605.
145. Pavlova, N. N. and Thompson, C. B. (2016) 'The Emerging Hallmarks of Cancer Metabolism', *Cell Metabolism*. Elsevier Inc., 23(1), pp. 27–47. doi: 10.1016/j.cmet.2015.12.006.
 146. Pellerin, L. and Magistretti, P. J. (1994) 'Glutamate uptake into astrocytes stimulates aerobic glycolysis: A mechanism coupling neuronal activity to glucose utilization', *Proceedings of the National Academy of Sciences of the United States of America*, 91(22), pp. 10625–10629. doi: 10.1073/pnas.91.22.10625.
 147. Pettersen, A. K., Marshall, D. J. and White, C. R. (2018) 'Understanding variation in metabolic rate', *Journal of Experimental Biology*, 221(1). doi: 10.1242/jeb.166876.
 148. Pietrocola, F. *et al.* (2015) 'Acetyl coenzyme A: A central metabolite and second messenger', *Cell Metabolism*, 21(6), pp. 805–821. doi: 10.1016/j.cmet.2015.05.014.
 149. Pocernicha, C. B. and Butterfield, D. A. (2003) 'Acrolein Inhibits NADH-Linked Mitochondrial Enzyme Activity : Implications for Alzheimer ' s Disease', 5(7), pp. 515–519.
 150. Quistorff, B. and Grunnet, N. (2011) 'The isoenzyme pattern of LDH does not play a physiological role; except perhaps during fast transitions in energy metabolism', *Aging*, 3(5), pp. 457–460. doi: 10.18632/aging.100329.
 151. Rafalski, V. A., Mancini, E. and Brunet, A. (2012) 'Energy metabolism and energy-sensing pathways in mammalian embryonic and adult stem cell fate', *Journal of Cell Science*, 125(23), pp. 5597–5608. doi: 10.1242/jcs.114827.
 152. Rafter, I. *et al.* (2012) 'Isoform-specific alanine aminotransferase measurement can distinguish hepatic from extrahepatic injury in

- humans', *International Journal of Molecular Medicine*, 30(5), pp. 1241–1249. doi: 10.3892/ijmm.2012.1106.
153. Raichur, S. *et al.* (2014) 'Short Article CerS2 Haploinsufficiency Inhibits β -Oxidation and Confers Susceptibility to Diet-Induced Steatohepatitis and Insulin Resistance', pp. 687–695. doi: 10.1016/j.cmet.2014.09.015.
154. Rauch, A. *et al.* (2019) 'network of stem cell transcription factors that act as repressors of adipogenesis', *Nature Genetics*. Springer US, 51(April). doi: 10.1038/s41588-019-0359-1.
155. Richardson, S. M. *et al.* (2016) 'Mesenchymal stem cells in regenerative medicine: Focus on articular cartilage and intervertebral disc regeneration', *Methods*. Elsevier Inc., 99, pp. 69–80. doi: 10.1016/j.ymeth.2015.09.015.
156. Rickard, D. J. *et al.* (1994) 'Induction of rapid osteoblast differentiation in rat bone marrow stromal cell cultures by dexamethasone and BMP-2', *Developmental Biology*, pp. 218–228. doi: 10.1006/dbio.1994.1022.
157. Robertson, D. G., Watkins, P. B. and Reily, M. D. (2011) 'Metabolomics in toxicology: Preclinical and clinical applications', *Toxicological Sciences*, 120(SUPPL.1), pp. 146–170. doi: 10.1093/toxsci/kfq358.
158. Rodríguez-Colman, M. J. *et al.* (2017) 'Interplay between metabolic identities in the intestinal crypt supports stem cell function', *Nature*, 543(7645), pp. 424–427. doi: 10.1038/nature21673.
159. Rosen, E. D. *et al.* (2017) 'Transcriptional regulation of adipogenesis', *Comprehensive Physiology*, 7(2), pp. 635–674. doi: 10.1002/cphy.c160022.
160. Rossi, A. *et al.* (2020) 'Defective Mitochondrial Pyruvate Flux

- Affects Cell Bioenergetics in Alzheimer's Disease-Related Models', *Cell Reports*. Elsevier Company., 30(7), pp. 2332-2348. doi: 10.1016/j.celrep.2020.01.060.
161. Ryall, J. G. *et al.* (2015) 'Metabolic Reprogramming of Stem Cell Epigenetics', *Cell Stem Cell*. Elsevier, 17(6), pp. 651-662. doi: 10.1016/j.stem.2015.11.012.
162. Scanu, M., Mancuso, L. and Cao, G. (2011) 'Evaluation of the use of human Mesenchymal Stem Cells for acute toxicity tests', *Toxicology in Vitro*. Elsevier Ltd, 25(8), pp. 1989-1995. doi: 10.1016/j.tiv.2011.07.006.
163. Schueren, F. *et al.* (2014) 'Peroxisomal lactate dehydrogenase is generated by translational readthrough in mammals', *eLife*, 3, p. e03640. doi: 10.7554/eLife.03640.
164. Schwartz, R. E. *et al.* (2002) 'Multipotent adult progenitor cells from bone marrow differentiate into functional hepatocyte-like cells', *Journal of Clinical Investigation*, 109(10), pp. 1291-1302. doi: 10.1172/JCI200215182.Introduction.
165. Sellers, K. *et al.* (2015) 'Pyruvate carboxylase is critical for non-small-cell lung cancer proliferation', *Journal of Clinical Investigation*, 125(2), pp. 687-698. doi: 10.1172/JCI72873.
166. Serrao, E. M. *et al.* (2016) 'MRI with hyperpolarised [1-¹³C]pyruvate detects advanced pancreatic preneoplasia prior to invasive disease in a mouse model', *Gut*, 65(3), pp. 465-475. doi: 10.1136/gutjnl-2015-310114.
167. Serrao, E. M. *et al.* (2018) 'Analysis of ¹³C and ¹⁴C labeling in pyruvate and lactate in tumor and blood of lymphoma-bearing mice injected with ¹³C- and ¹⁴C-labeled pyruvate', *NMR in Biomedicine*, 31(5), pp. 1-10. doi: 10.1002/nbm.3901.
168. Shah, S. H. and Newgard, C. B. (2015) 'Integrated Metabolomics

- and Genomics: Systems Approaches to Biomarkers and Mechanisms of Cardiovascular Disease', *Circulation: Cardiovascular Genetics*, 8(2), pp. 410–419. doi: 10.1161/CIRCGENETICS.114.000223.
169. Shim, H. *et al.* (1997) 'c-Myc transactivation of LDH-A: Implications for tumor metabolism and growth', *Proceedings of the National Academy of Sciences of the United States of America*, 94(13), pp. 6658–6663. doi: 10.1073/pnas.94.13.6658.
170. Shum, L. C. *et al.* (2016) 'Energy Metabolism in Mesenchymal Stem Cells during Osteogenic Differentiation', *Stem Cells and Development*, 25(2), pp. 114–122. doi: 10.1089/scd.2015.0193.
171. Shyh-Chang, N., Daley, G. Q. and Cantley, L. C. (2013) 'Stem cell metabolism in tissue development and aging', *Development (Cambridge)*, 140(12), pp. 2535–2547. doi: 10.1242/dev.091777.
172. Simsek, T. *et al.* (2010) 'The distinct metabolic profile of hematopoietic stem cells reflects their location in a hypoxic niche', *Cell Stem Cell*. Elsevier Ltd, 7(3), pp. 380–390. doi: 10.1016/j.stem.2010.07.011.
173. Šišková, Z. *et al.* (2014) 'Dendritic structural degeneration is functionally linked to cellular hyperexcitability in a mouse model of alzheimer's disease', *Neuron*, 84(5), pp. 1023–1033. doi: 10.1016/j.neuron.2014.10.024.
174. Song, Z. *et al.* (2019) 'Application of NMR metabolomics to search for human disease biomarkers in blood', *Clinical Chemistry and Laboratory Medicine*, 57(4), pp. 417–441. doi: 10.1515/cclm-2018-0380.
175. Sorbi, S., Bird, E. D. and Blass, J. P. (1983) 'Decreased pyruvate dehydrogenase complex activity in Huntington and Alzheimer brain', *Annals of Neurology*, 13(1), pp. 72–78. doi: 10.1002/ana.410130116.
176. Srinivasan, B. (2020) 'Words of advice: teaching enzyme kinetics',

- FEBS Journal*, pp. 1–16. doi: 10.1111/febs.15537.
177. Stuart, C. A. *et al.* (2011) 'Brain glucose transporter (Glut3) haploinsufficiency does not impair mouse brain glucose uptake', *Brain Research*. Elsevier B.V., 1384, pp. 15–22. doi: 10.1016/j.brainres.2011.02.014.
178. Sugden, M. C. and Holness, M. J. (2003) 'Recent advances in mechanisms regulating glucose oxidation at the level of the pyruvate dehydrogenase complex by PDKs', *American Journal of Physiology - Endocrinology and Metabolism*, 284(5 47-5), pp. 0–7. doi: 10.1152/ajpendo.00526.2002.
179. Świderek, K. and Paneth, P. (2011) 'Differences and similarities in binding of pyruvate and l-lactate in the active site of M4 and H4 isoforms of human lactate dehydrogenase', *Archives of Biochemistry and Biophysics*, 505(1), pp. 33–41. doi: 10.1016/j.abb.2010.10.010.
180. Tabar, V. and Studer, L. (2014) 'Pluripotent stem cells in regenerative medicine: Challenges and recent progress', *Nature Reviews Genetics*. Nature Publishing Group, 15(2), pp. 82–92. doi: 10.1038/nrg3563.
181. Tchernof, A. *et al.* (2006) 'Regional differences in adipose tissue metabolism in women: Minor effect of obesity and body fat distribution', *Diabetes*, 55(5), pp. 1353–1360. doi: 10.2337/db05-1439.
182. Tchetina, E. V (2018) 'and osteoarthritic chondrocytes', *Rheumatology International*. Springer Berlin Heidelberg, 38(11), pp. 1963–1974. doi: 10.1007/s00296-018-4103-4.
183. Tormos, K. V. *et al.* (2011) 'Mitochondrial complex III ROS regulate adipocyte differentiation', *Cell Metabolism*. Elsevier Inc., 14(4), pp. 537–544. doi: 10.1016/j.cmet.2011.08.007.
184. Tran, M. *et al.* (2019) ' First-in-human in vivo non-invasive

- assessment of intra-tumoral metabolic heterogeneity in renal cell carcinoma', *BJR/case reports*, 5(3), p. 20190003. doi: 10.1259/bjrcr.20190003.
185. Uccelli, A., Moretta, L. and Pistoia, V. (2008) 'Mesenchymal stem cells in health and disease', *Nature Reviews Immunology*, 8(9), pp. 726–736. doi: 10.1038/nri2395.
186. Uemura, E. and Greenlee, H. W. (2001) 'Amyloid β -peptide inhibits neuronal glucose uptake by preventing exocytosis', *Experimental Neurology*, 170(2), pp. 270–276. doi: 10.1006/exnr.2001.7719.
187. Utter, M. F. and Keerch, B. D. (1960) 'Formation of Oxaloacetate', *Journal of Biological Chemistry*, 235(5), pp. 17–19.
188. Valko, M. *et al.* (2007) 'Free radicals and antioxidants in normal physiological functions and human disease', *International Journal of Biochemistry and Cell Biology*, 39(1), pp. 44–84. doi: 10.1016/j.biocel.2006.07.001.
189. Valvona, C. J. *et al.* (2016) 'The Regulation and Function of Lactate Dehydrogenase A: Therapeutic Potential in Brain Tumor', *Brain Pathology*, 26(1), pp. 3–17. doi: 10.1111/bpa.12299.
190. Veenstra, T. D. (2012) 'Metabolomics : the nal frontier ?', pp. 2010–2012.
191. Voehler, M. W. *et al.* (2006) 'Performance of cryogenic probes as a function of ionic strength and sample tube geometry', *Journal of Magnetic Resonance*, 183(1), pp. 102–109. doi: 10.1016/j.jmr.2006.08.002.
192. Walton, H. S. and Dodd, P. R. (2007) 'Glutamate-glutamine cycling in Alzheimer's disease', *Neurochemistry International*, 50(7–8), pp. 1052–1066. doi: 10.1016/j.neuint.2006.10.007.
193. Wang, P. P. *et al.* (2004) 'Expression of hepatocyte-like

- phenotypes in bone marrow stromal cells after HGF induction', 320, pp. 712–716. doi: 10.1016/j.bbrc.2004.05.213.
194. Wang, X. *et al.* (2015) 'Systemic pyruvate administration markedly reduces neuronal death and cognitive impairment in a rat model of Alzheimer's disease', *Experimental Neurology*. Elsevier Inc., 271, pp. 145–154. doi: 10.1016/j.expneurol.2015.06.008.
195. Warburg, O. (1931) 'The metabolism of tumours', *J Gen Physio.*, 1(3653), p. 74. doi: 10.1136/bmj.1.3653.74-a.
196. Warburg, O. (1956) 'On the origin of cancer cells', *Science*, 123(3191), pp. 309–314. doi: 10.1126/science.123.3191.309.
197. Wellen, K. E. *et al.* (2009) 'ATP-citrate lyase links cellular metabolism to histone acetylation', *Science*, 324(5930), pp. 1076–1080. doi: 10.1126/science.1164097.
198. Wibom, R., Hagenfeldt, L. and Von Döbeln, U. (2002) 'Measurement of ATP production and respiratory chain enzyme activities in mitochondria isolated from small muscle biopsy samples', *Analytical Biochemistry*, 311(2), pp. 139–151. doi: 10.1016/S0003-2697(02)00424-4.
199. Wikoff, W. R. *et al.* (2009) 'Metabolomics analysis reveals large effects of gut microflora on mammalian blood metabolites', *Proceedings of the National Academy of Sciences of the United States of America*, 106(10), pp. 3698–3703. doi: 10.1073/pnas.0812874106.
200. Winter, G. and Krömer, J. O. (2013) 'Fluxomics - connecting 'omics analysis and phenotypes', *Environmental Microbiology*, 15(7), pp. 1901–1916. doi: 10.1111/1462-2920.12064.
201. Wishart, D. S. (2008) 'Metabolomics: applications to food science and nutrition research', *Trends in Food Science and Technology*, 19(9), pp. 482–493. doi: 10.1016/j.tifs.2008.03.003.
202. Wishart, D. S. (2019) 'Metabolomics for investigating physiological

- and pathophysiological processes', *Physiological Reviews*, 99(4), pp. 1819–1875. doi: 10.1152/physrev.00035.2018.
203. Wu, G. and Morris, S. M. (1998) 'Arginine metabolism: Nitric oxide and beyond', *Biochemical Journal*, 336(1), pp. 1–17. doi: 10.1042/bj3360001.
204. Wu, Y. *et al.* (2017) 'Lactate induces osteoblast differentiation by stabilization of HIF1 α ', *Molecular and Cellular Endocrinology*, 452, pp. 84–92. doi: 10.1016/j.mce.2017.05.017.
205. Wyss-Coray, T. and Rogers, J. (2012) 'Inflammation in Alzheimer disease-A brief review of the basic science and clinical literature', *Cold Spring Harbor Perspectives in Medicine*, 2(1), pp. 1–23. doi: 10.1101/cshperspect.a006346.
206. Xu, J. *et al.* (2019) 'Regional protein expression in human Alzheimer's brain correlates with disease severity', *Communications Biology*. Springer US, 2(1). doi: 10.1038/s42003-018-0254-9.
207. Xu, W. J. *et al.* (2018) 'Observation of acetyl phosphate formation in mammalian mitochondria using real-time in-organelle NMR metabolomics', *Proceedings of the National Academy of Sciences of the United States of America*, 115(16), pp. 4152–4157. doi: 10.1073/pnas.1720908115.
208. Zaitso, K. *et al.* (2016) 'Application of metabolomics to toxicology of drugs of abuse: A mini review of metabolomics approach to acute and chronic toxicity studies', *Drug Metabolism and Pharmacokinetics*. Elsevier Ltd, 31(1), pp. 21–26. doi: 10.1016/j.dmpk.2015.10.002.
209. Zhang, F. *et al.* (2011) 'Gene expression profile change and associated physiological and pathological effects in mouse liver induced by fasting and refeeding', *PLoS ONE*, 6(11), pp. 1–11. doi: 10.1371/journal.pone.0027553.
210. Zhang, R. *et al.* (2018) 'Investigation into cellular glycolysis for the

- mechanism study of energy metabolism disorder triggered by lipopolysaccharide', *Toxins*, 10(11). doi: 10.3390/toxins10110441.
211. Zhao, S. *et al.* (2016) 'ATP-Citrate Lyase Controls a Glucose-to-Acetate Metabolic Switch', *Cell Reports*. Elsevier Company., 17(4), pp. 1037–1052. doi: 10.1016/j.celrep.2016.09.069.
212. Barone, E. *et al.* (2016) 'Impairment of biliverdin reductase-A promotes brain insulin resistance in Alzheimer disease: A new paradigm', *Free Radical Biology and Medicine*, 91, pp. 127–142. doi: 10.1016/j.freeradbiomed.2015.12.012.
213. Bianco, P., Robey, P. G. and Simmons, P. J. (2008) 'Mesenchymal Stem Cells: Revisiting History, Concepts, and Assays', *Cell Stem Cell*, 2(4), pp. 313–319. doi: 10.1016/j.stem.2008.03.002.
214. BRADFORD, M. M. (1976) 'A Rapid and Sensitive Method for the Quantitation of Microgram Quantities of Protein Utilizing the Principle of Protein-Dye Binding', *Analytical Biochemistry*, 72, pp. 248–254. doi: 10.1016/j.cj.2017.04.003.
215. Bröer, S. *et al.* (2007) 'Alanine metabolism, transport, and cycling in the brain', *Journal of Neurochemistry*, 102(6), pp. 1758–1770. doi: 10.1111/j.1471-4159.2007.04654.x.
216. Cukierman-Yaffe, T. *et al.* (2009) 'Relationship between baseline glycemic control and cognitive function in individuals with type 2 diabetes and other cardiovascular risk factors the action to control cardiovascular risk in diabetes-memory in diabetes (ACCORD-MIND) trial', *Diabetes Care*, 32(2), pp. 221–226. doi: 10.2337/dc08-1153.
217. Cunnane, S. *et al.* (2012) *Brain fuel metabolism and AD*. doi: 10.1016/j.nut.2010.07.021.BRAIN.
218. Dienel, G. A. (2019) 'Brain glucose metabolism: Integration of energetics with function', *Physiological Reviews*, 99(1), pp. 949–1045. doi: 10.1152/physrev.00062.2017.
219. Esen, E. and Long, F. (2014) 'Aerobic glycolysis in osteoblasts', *Current Osteoporosis Reports*, 12(4), pp. 433–438. doi: 10.1007/s11914-014-0235-y.
220. Felig, P. (1973) 'The glucose-alanine cycle', *Metabolism*, 22(2), pp. 179–207. doi: 10.1016/0026-0495(73)90269-2.
221. Gimble, J. M. *et al.* (2008) 'In vitro differentiation potential of mesenchymal

- stem cells', *Transfusion Medicine and Hemotherapy*, 35(3), pp. 228–238. doi: 10.1159/000124281.
222. Ioannou, M. S. *et al.* (2019) 'Neuron-Astrocyte Metabolic Coupling Protects against Activity-Induced Fatty Acid Toxicity', *Cell*. Elsevier Inc., 177(6), pp. 1522–1535.e14. doi: 10.1016/j.cell.2019.04.001.
223. Ito, K. and Suda, T. (2014) 'Metabolic requirements for the maintenance of self-renewing stem cells', *Nature Reviews Molecular Cell Biology*, 15(4), pp. 243–256. doi: 10.1038/nrm3772.
224. Janson, J. *et al.* (2004) 'Increased Risk of Type 2 Diabetes in Alzheimer Disease', *Diabetes*, 53(2), pp. 474–481. doi: 10.2337/diabetes.53.2.474.
225. Keller, D., Erö, C. and Markram, H. (2018) 'Cell densities in the mouse brain: A systematic review', *Frontiers in Neuroanatomy*, 12(October). doi: 10.3389/fnana.2018.00083.
226. Lai, P. L. *et al.* (2017) 'Efficient generation of chemically induced mesenchymal stem cells from human dermal fibroblasts', *Scientific Reports*. Nature Publishing Group, 7, pp. 1–13. doi: 10.1038/srep44534.
227. Lee, H. J. *et al.* (2012) 'Human umbilical cord blood-derived mesenchymal stem cells improve neuropathology and cognitive impairment in an Alzheimer's disease mouse model through modulation of neuroinflammation', *Neurobiology of Aging*, 33(3), pp. 588–602. doi: 10.1016/j.neurobiolaging.2010.03.024.
228. Lee, J. B. *et al.* (2003) 'Migration and differentiation of nuclear fluorescence-labeled bone marrow stromal cells after transplantation into cerebral infarct and spinal cord injury in mice', *Neuropathology*, 23(3), pp. 169–180. doi: 10.1046/j.1440-1789.2003.00496.x.
229. Lemeshko, V. V. (2018) 'VDAC electronics: 5. Mechanism and computational model of hexokinase-dependent generation of the outer membrane potential in brain mitochondria', *Biochimica et Biophysica Acta - Biomembranes*. Elsevier B.V, 1860(12), pp. 2599–2607. doi: 10.1016/j.bbamem.2018.10.004.
230. Li, X. *et al.* (2016) 'Human neural stem cell transplantation rescues cognitive defects in APP/PS1 model of Alzheimer's disease by enhancing neuronal connectivity and metabolic activity', *Frontiers in Aging Neuroscience*, 8(NOV), pp. 1–14. doi: 10.3389/fnagi.2016.00282.

231. Liu, X. Y., Yang, L. P. and Zhao, L. (2020) 'Stem cell therapy for alzheimer's disease', *World Journal of Stem Cells*, 12(8), pp. 787–802. doi: 10.4252/WJSC.V12.I8.787.
232. Lunt, S. Y. and Vander Heiden, M. G. (2011) 'Aerobic Glycolysis: Meeting the Metabolic Requirements of Cell Proliferation', *Annual Review of Cell and Developmental Biology*, 27(1), pp. 441–464. doi: 10.1146/annurev-cellbio-092910-154237.
233. Maleki, M. *et al.* (2014) 'Comparison of mesenchymal stem cell markers in multiple human adult stem cells', *International Journal of Stem Cells*, 7(2), pp. 118–126. doi: 10.15283/ijsc.2014.7.2.118.
234. Nakaji-Hirabayashi, T., Kato, K. and Iwata, H. (2013) 'In vivo study on the survival of neural stem cells transplanted into the rat brain with a collagen hydrogel that incorporates laminin-derived polypeptides', *Bioconjugate Chemistry*, 24(11), pp. 1798–1804. doi: 10.1021/bc400005m.
235. Nakano, M. *et al.* (2020) 'Bone marrow-derived mesenchymal stem cells improve cognitive impairment in an Alzheimer's disease model by increasing the expression of microRNA-146a in hippocampus', *Scientific Reports*. Nature Publishing Group UK, 10(1), pp. 1–15. doi: 10.1038/s41598-020-67460-1.
236. Petit-Taboué, M. C. *et al.* (1998) 'Effects of healthy aging on the regional cerebral metabolic rate of glucose assessed with statistical parametric mapping', *NeuroImage*, 7(3), pp. 176–184. doi: 10.1006/nimg.1997.0318.
237. Puchalska, P. and Crawford, P. A. (2019) 'Multi-dimensional roles of ketone bodies', *Physiology & behavior*, 176(3), pp. 139–148. doi: 10.1016/j.cmet.2016.12.022.Multi-dimensional.
238. Radde, R. *et al.* (2006) 'A β 42-driven cerebral amyloidosis in transgenic mice reveals early and robust pathology', *EMBO Reports*, 7(9), pp. 940–946. doi: 10.1038/sj.embor.7400784.
239. Song, C. *et al.* (2019) 'Elevated Exogenous Pyruvate Potentiates Mesodermal Differentiation through Metabolic Modulation and AMPK/mTOR Pathway in Human Embryonic Stem Cells', *Stem Cell Reports*. ElsevierCompany., 13(2), pp. 338–351. doi: 10.1016/j.stemcr.2019.06.003.
240. Stallknecht, B., Vissing, J. and Galbo, H. (1998) 'Lactate production and

- clearance in exercise. Effects of training. A mini-review', *Scandinavian Journal of Medicine and Science in Sports*, 8(3), pp. 127–131. doi: 10.1111/j.1600-0838.1998.tb00181.x.
241. Sutcliffe, J. G. *et al.* (2011) 'Peripheral reduction of β -amyloid is sufficient to reduce brain β -amyloid: Implications for Alzheimer's disease', *Journal of Neuroscience Research*, 89(6), pp. 808–814. doi: 10.1002/jnr.22603.
242. Urrutia, D. N. *et al.* (2019) 'Comparative study of the neural differentiation capacity of mesenchymal stromal cells from different tissue sources: An approach for their use in neural regeneration therapies', *PLoS ONE*, 14(3), pp. 1–17. doi: 10.1371/journal.pone.0213032.
243. Waterhouse, C. and Keilson, J. (1969) 'Cori cycle activity in man.', *The Journal of clinical investigation*, 48(12), pp. 2359–2366. doi: 10.1172/JCI106202.
244. Yuan, X., Logan, T. M. and Ma, T. (2019) 'Metabolism in human mesenchymal stromal cells: A missing link between HMSC biomanufacturing and therapy?', *Frontiers in Immunology*, 10(MAY), pp. 1–11. doi: 10.3389/fimmu.2019.00977.
245. Zhang, M. *et al.* (2018) 'Lactate deficit in an Alzheimer disease mouse model: The relationship with neuronal damage', *Journal of Neuropathology and Experimental Neurology*, 77(12), pp. 1163–1176. doi: 10.1093/jnen/nly102.

6. Appendix

Table A: Components of Master Mix 1 (for cDNA synthesis). Values given are per sample.

Component	Volume (μL)
Total RNA (500ng/ μL)	10
Random primers	0.5
Deoxynucleotide mix (10mM)	1
Nuclease-free water	1.5

Table B: Components of Master Mix 2 (for cDNA synthesis). Values given are per sample

Component	Volume (μL)
5X First Strand Buffer	4
Dithiothreitol (0.1M)	1
RNaseOUT RNase inhibitor	1
Superscript III Reverse transcriptase	1

Table C: list of primers used for qPCR

Gene	Forward primer	Reverse primer
Gpt	5'- CCTTCAAGCAGTTTCAAGCA- 3'	5'- GCTCCGTGAGTTTAGCCTTG- 3'
Ldha	5'- TTAACCCAGAACTGGGCACT- 3'	5'- GTAGGCACTGTCCACCACCT- 3'
Pdha1	5'- GGTGGTGTGGTCCTAGCTGT- 3'	5'- ATTCCTGGTGGCTGCTACAC- 3'
Gapdh	5'- AAGAGGGATGCTGCCCTTAC- 3'	5'- CCATTTTGTCTACGGGACGA- 3'

Table D: Thermocycler programme for qPCR

Step	temperature (°C)	Time (s)
Holding stage	95	20
Cycling stage	95-60	3-30 (40 cycles)
Melt curve stage	95-60-95	15-60-15

Figure A: Example spectra acquire via 1H NMR

